Solution-processed charge extraction interlayers and electrodes for organic solar cells

Im Fachbereich
Elektrotechnik, Informationstechnik, Druck- und Medientechnik
der Bergischen Universität Wuppertal

zur Erlangung des akademischen Grades eines
Doktor-Ingenieurs genehmigte Dissertation
von

M.Sc. Kirill Zilberberg
aus
Tscheljabinsk, Russische Föderation

Referenten: Prof. Dr. rer. nat. T. Riedl
Prof. Dr. rer. nat. U. Scherf

Tag der mündlichen Prüfung: 11. Juli 2014

Die Dissertation kann wie folgt zitiert werden:
urn:nbn:de:hbz:468-20141008-141101-0
[http://nbn-resolving.de/urn/resolver.pl?urn=urn%3Anbn%3Ade%3Ahbz%3A468-20141008-141101-0]

Contents

Abbreviation list

Symbol	Description	Unit
α	optical absorption coefficient	1/cm
A	device Area	cm^2
CPD	Contact Potential Difference	eV
E	Energy	eV
EA	Electron Affinity	eV
E_F	Fermi-Energy	eV
f	frequency	Hz
FF	Fill Factor	%
h	Planck constant ($6.626 \cdot 10^{-34}$)	J s
IP	Ionization Potential	eV
J	electrical current density	mA/cm^2
J_{mpp}	Maximum Power Point current density	mA/cm^2
J_{ph}	Photo-generated current density	mA/cm^2
J_s	electrical Saturation current density	mA/cm^2
J_{sc}	electrical Short-Circuit current density	mA/cm^2
I	electrical current	mA
I_{mpp}	Maximum Power Point electrical current	mA
IQE	Internal Quantum Efficiency	%
k	Boltzmann constant ($1.38 \cdot 10^{-23}$)	J/K
λ	Wavelength	nm
MW	Molecular Weight	g/mol
n	diode ideality factor	
P	Power density	mW/cm^2
PCE	Power Conversion Efficiency	%
P_{in}	Input Power density	mW/cm^2
P_{out}	maximum device Output Power density	mW/cm^2
q	elementary charge ($1.602 \cdot 10^{-19}$)	C
rH	relative Humidity	%
R_p	Parallel (shunt) Resistance	Ω
R_s	Series Resistance	Ω
R_{sh}	Sheet Resistance	Ω/sq

$S_{semisphere}$	Semisphere-scattered optical transmittance	%
T	operation Temperature	K
T_{av}	Average optical transmittance	%
$T_{specular}$	Specular optical transmittance	%
V	Voltage	V
V_{mpp}	Maximum Power Point voltage	V
V_{oc}	Open-Circuit Voltage	V
WF	Work Function	eV

AcAc	Acetylacetone
AFM	Atomic Force Microscopy
AgNWs	Silver Nano-Wires
ALD	Atomic Layer Deposition
AZO	Aluminum-doped Zink Oxide (Al:ZnO)
BHJ	Bulk Heterojunction
CB	Conduction Band
CPE	Conjugated Polyelectrolyte
D/A	Donor/Acceptor
DFT	Density Functional Theory
DLS	Dynamic Light Scattering
EBIP	Electron Beam Induced Potential contrast
$eMoO_3$	Thermally evaporated molybdenum(VI)oxide
eV_2O_5	Thermally evaporated vanadium(V)oxide
HOMO	Highest Occupied Molecular Orbital
HOPG	Highly Ordered Pyrolytic Graphite
IPA	Isopropanol
IPES	Inverse Photoelectron Spectroscopy
ITO	Indium Tin Oxide
JV	Current-density / Voltage characteristic
KP	Kelvin Probe
LUMO	Lowest Unoccupied Molecular Orbital
MIM	Metal-Insulator-Metal (model)
MPP	Maximum Power Point
NMR	Nuclear Magnetic Resonance
NPs	Nano-Particles
ODT	1,8-Octanedithiol

Abbreviation list

OE	Organic Electronics
OLED	Organic Light Emitting Device
OPV	Organic Photovoltaics
OSC	Organic Solar Cell
P3BrHT	Poly(3-[6-bromohexyl]thiophene)
P3HT	Poly(3-hexylthiophene-2,5-diyl)
P3ImHT	N-methylimidazoliniumalkyl-substituted P3BrHT
$PC_{60}BM$	Phenyl-C61-butyric acid methyl ester
$PC_{70}BM$	Phenyl-C71-butyric acid methyl ester
PEDOT:PSS	Polyethylene dioxythiophene:polystyrenesulfonate
PCDTBT	Poly[N-9'-heptadecanyl-2,7-carbazole-alt-5,5-(4',7'-di-2-thienyl-2',1',3'-benzothiadiazole)]
PCPDTBT	Poly[2,6-(4,4-bis-(2-ethylhexyl)-4H-cyclopenta [2,1-b;3,4-b']dithiophene)-alt-4,7(2,1,3-benzothiadiazole)]
PL	Photoluminescence
PTFE	Polytetrafluoroethylene
PV	Power density / Voltage characteristics
RF	Radio Frequency
R2R	Roll-to-Roll
rms	Root Mean Square (of surface roughness)
RT	Room Temperature
SE	Secondary Electrons
SEM	Scanning Electron Microscopy
$sMoO_x$	Sol-gel processed molybdenum oxide
SAM	Self-Assembled Monolayers
SPP	Surface Plasmon Polariton
$sSnO_x$	Sol-gel processed tin oxide
$sTiO_x$	Sol-gel processed titanium oxide
sVO_x	Sol-gel processed vanadium oxide
TCO	Transparent Conductive Oxide
TMA	Trimethylaluminum
TMO	Transition Metal Oxide
UPS	Ultraviolet Photoelectron Spectroscopy
VB	Valence Band
XRD	X-Ray Diffraction
XPS	X-Ray Photoelectron Spectroscopy

1. Introduction

With increasing global population, rising economics of 3rd world countries and the hunt for higher life standards, the demand on energy is continuously increasing. The energetic hunger is satisfied almost exclusively by so far easily accessible fossil fuels. Aside from their limited earth-abundance, a considerable and partially irreversible pollution of the biosphere is inevitably associated with their gain and consumption.

Recognizing the problem, world leading economics on governmental and private business level invest significant material and human resources into research on green and regenerative energy sources. Among those, solar energy conversion is a very promising field. Though it is by far not able to cover the whole energy demand, it can still considerably contribute to the diversified network of energy “production”. Especially for remote regions aside from power transmission lines, an island photovoltaic system is often the only possible robust power source.

Traditionally, solar cells are based on inorganic semiconductors, most prominently silicon. Very recently, the field of organic photovoltaics (OPV) has attracted significant attention. Here, organic semiconductor materials, predominantly based on the element carbon are used. Much effort in modelling and synthesis of novel efficient and stable materials allowed to break the 10% efficiency barrier for polymer:fullerene organic solar cells (OSCs).[1-3]

Due to high absorption coefficients of organic materials, thin film devices exhibiting pronounced mechanical flexibility and light-weight can be realized.[4-10] This even allows for covering objects, which are curved in three dimensions, in static, mobile and design applications. The unique spectral absorption properties of organic materials allow for semi-transparent solar cells that may open entirely new markets of e.g. window-embedded see-through [11-14] power-generating devices.

However, photo-active organic materials typically exhibit low charge carrier mobilities, which results in rather moderate performance compared to conventional inorganic PV. The competitiveness of OSCs relies, therefore, on cheapness, quick energetic payback and simultaneously large-area high-throughput production, which in turn requires roll-to-roll (R2R) liquid processing of device layers in order to avoid time- and energy-intensive vacuum processing steps.[15, 16]

R2R processing of OPV on flexible foil substrates, typically plastics, brings technological restrictions regarding the processing temperatures. Even though the polymer:fullerene light-absorbing blends fulfill the R2R requirements, as they can be processed at moderate temperatures (<120°C) from solution, this is not enough for a market-ready device. Due to the physics of OSCs, low-temperature liquid-processed interlayers are required to facilitate the charge extraction of the photo-generated charges. Last but not least, high quality low-temperature liquid-processed electrodes are required for large-area applications.

This work addresses the technological issues stated above and proposes suitable concepts for liquid-processing of functional building blocks in organic solar devices. After a brief introduction into the OSCs physics (**Chapter 2**), it is for the first time demonstrated that vanadium oxide and molybdenum oxide thin films with a high work-function can be processed by a sol-gel technique at temperatures as low as room-temperature. They are used as hole-extraction interlayers in OSCs with equivalent characteristics, as of those based on vacuum-processed metal oxides (**Chapter 3**). Notably, a substantially enhanced long-term stability is evidenced compared to devices based on established solution-processed anode interlayers. In the same context, it is demonstrated that for inverted OSCs these high work-function metal oxides can even be wet-processed on top of the sensitive organic photo-active layers.

In **Chapter 4**, a direct modification of the indium-tin oxide (ITO) cathode in inverted OSCs by deposition of ultra-thin conjugated polyelectrolyte films and avoiding the use of additional low work-function metal oxide layer is presented.

The realization of, at the moment, one of the best performing stable and indium-free solution-processed composite transparent electrodes (**Chapter 5**) based on silver nano-wires and moderately conductive metal oxides at low temperatures, down to room-temperature, is considered.

Ultimately, based on this groundwork, the realization of efficient all-solution-processed semitransparent OSCs comprising room-temperature solution-processed metal oxide interlayers and composite transparent electrodes is demonstrated.

In **Chapter 6**, a conclusion to the main part of this thesis is given. In the **Appendix A**, an excursus on the optimization of so called low-bandgap OSCs is introduced.

2. Basics of organic solar cells

2.1. Materials and charge transport

For polymer:fullerene OSCs the conjugated polymers with alternating single and double bonds are used. In order to establish an energetically favorable spatial orbital orientation, sp2-hybridization of the backbone carbon orbitals takes place. The spatial overlap of z-oriented π-orbitals of carbon leads to delocalization of the electrons in these orbitals over several repeat units of the conjugated polymer. The energetic splitting of overlapping π_z-orbitals results in narrow charge transport "bands" consisting of bonding (lower-energy, occupied) and antibonding (higher-energy, unoccupied) orbitals separated by a bandgap. Therefore, the conjugated molecule resembles a one-dimensional (intrinsic) semiconductor with the bandgap defined as the energetic difference between the highest occupied molecular orbital (HOMO) and the lowest unoccupied molecular orbital (LUMO).

Conjugated molecules exhibit high optical absorption coefficients (on the order of 10^5 cm^{-1}) due to the pronounced overlap of electronic wave functions of ground and excited state.[17] In addition, the absorption spectrum is broadened by vibronic molecular levels.[18] The bandgap of conjugated polymers can be tuned to some extent by varying the conjugation length. The absorption spectrum of the polymer becomes red-shifted for more pronounced π-electron delocalization.[19]

Due to a great degree of disorder and rather small overlap of electron wave functions of adjacent molecules, the mostly amorphous films of organic semiconductors typically exhibit modest charge carrier mobilities of 10^{-6} to 10^{-3} cm^2/Vs strongly linked on the film morphology.[20-22] The charge transport in electric field occurs via phonon-assisted intermolecular hopping between the localized states.[23] The efficiency of this process is typically limited by a rather moderate thermally activated hopping probability.

2.2. Polymer:fullerene solar cell device physics

Unlike in the inorganic semiconductors, the absorption of light by organic molecules does not immediately yield separated charge carriers, but results in a generation of coulombically bound electron-hole pairs, so called Frenkel excitons. The strong coulomb attraction within these excitons is governed by a relatively low dielectric constant of van-der-Waals bound ensemble of molecules and typically accounts for binding energies of several tenth of an eV.[24-26] Importantly, the exciton is electrically neutral and does not oblige to movement in electric field. Instead, a spatially limited (typically several tens nm) [27-32] Brownian diffusion of exciton via complex intermolecular energy transfer can take place before recombination.

For exciton dissociation, a further material with a LUMO level positioned below that of the polymer must be typically positioned in the vicinity of the polymer (**Figure 2.2.1**) to offer energetically more favorable states for an electron. The fullerene is one of the classes of the materials used in OPV, which exhibit the deeper LUMO compared to many absorber polymers, providing the energetic off-set on the order of the exciton binding energy. Thereupon, the polymer is usually signified as an electron donor (D) and the fullerene moiety as an acceptor (A). The D-to-A electron transfer was witnessed to be ultrafast (~50 fs) and, thus, very effective in comparison to competitive (non-)radiative exciton decay processes (~ns, µs).[33-36] After exciton dissociation, the propagation of electrons and holes to the outer electrodes occurs via $LUMO_A$ and $HOMO_D$ states respectively (**Figure 2.2.1**).[37-39]

For an efficient light harvesting, 70-200 nm (dependent on material extinction coefficients) of absorbing organic layer is required. In such thick layers, the D/A phase boundary must be accessible within an exciton diffusion length. In addition, the transport of separated charges toward the electrodes must occur via continuous percolation pathways in phase of each material in order to avoid the recombination of charge carriers. To

meet these requirements simultaneously, the concept of a so called bulk heterojunction (BHJ) was introduced.[40] Here, the polymer and the fullerene are blended previous to layer deposition. To adjust the sophisticated thermo-dynamically driven self-organizing morphology with crystalline and amorphous domains [41, 42] and for a proper nano-scale phase separation, selective co-solvents [43, 44] with different vapor pressures and/or post-deposition thermal annealing [45] are typically applied.

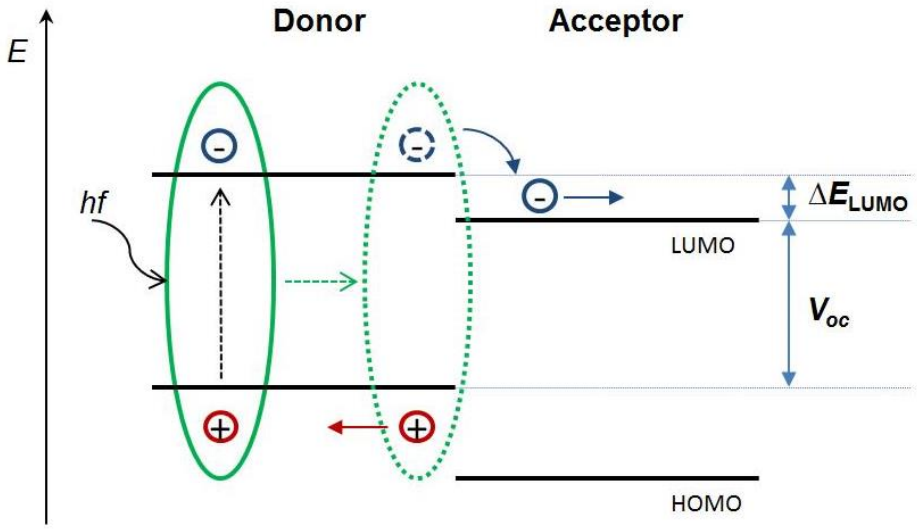

Figure 2.2.1. Energetic scheme of a D/A interface, exciton generation. diffusion and dissociation. Natural limit of open-circuit voltage (V_{oc}) is illustrated.

Ideally, the thickness of the active layer and the bandgap of the polymer predominantly determine the amount of absorbed photons in overlapped spectral region and, thus, the photo-generated current. Meanwhile, the energetic difference between $LUMO_A$ and $HOMO_D$ (**Figure 2.2.1**) determines the maximal achievable open-circuit voltage (V_{oc}) of the OPV device. Strictly speaking, the V_{oc} is defined as a difference between the quasi Fermi-energies of D/A upon splitting due to reasonable amount of free charge carriers in respective orbitals.[46]

2.3. Device characteristics and equivalent circuit

The analysis of OSC performance is essentially associated with a *JV*-curve of the device (**Figure 2.3.1.-a**), which is approximated by a *JV*-curve derived from the Shockley-equation (**Equation 2.3.1**) known from ideal inorganic p-n-junctions.[47] Under illumination, a negative offset due to a photo-generated current density (J_{ph}) is found. Here, J_{ph} is determined by pure photon-to-electron conversion. The series (R_s) and parallel (R_p) resistances account for parasitic effects in a realistic device, according to the equivalent circuit (**Figure 2.3.2.-a**).

R_p reflects the macroscopic effect of leakage currents in the device independent on their origin and is also affected by recombination.[47] R_s may arise from energetic interface barriers, limited lateral electrode conductivity and limited charge carrier mobilities within the BHJ and reduces the device current (**Figure 2.3.2.-b**).[47]

$$J = \frac{1}{1+\frac{R_S}{R_p}} \cdot \left[J_s \cdot \left(e^{\frac{qV - q \cdot JA \cdot R_S}{n \cdot kT}} - 1 \right) - \left(J_{ph} - \frac{V}{R_p \cdot A} \right) \right], \qquad (\mathbf{2.3.1})$$

with J – current density through the diode, R_s – series device resistance, R_p – parallel device resistance, J_s – dark saturation current density, q – elementary charge, V – voltage, A – device area, n – ideality factor, k – Boltzmann constant, T - operation temperature, J_{ph} – photo-generated current density.

$$V_{oc} = n\frac{kT}{q} \cdot ln\left[1 + \frac{J_{ph}}{J_s} \cdot \left(1 - \frac{V_{oc}}{J_{ph} A \cdot R_p} \right) \right] \qquad (\mathbf{2.3.2})$$

$$J_{sc} = -\frac{1}{1+\frac{R_S}{R_p}} \cdot \left[J_{ph} - J_s \cdot \left(e^{q \cdot \frac{|J_{SC}| \cdot A \cdot R_S}{nkT}} - 1 \right) \right] \qquad (\mathbf{2.3.3})$$

For the device performance, it is only the resulting mobility for a given D/A system at given treatment steps and resulting morphology that matters.

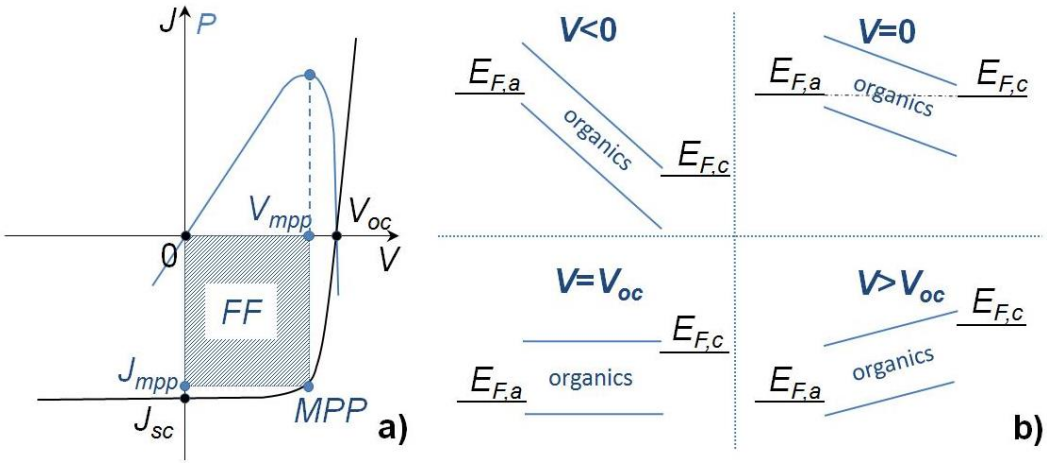

Figure 2.3.1. Schematic *JV*- and *PV*-curve of a solar cell under illumination with marked characteristic points (a); schematic energetic diagram of MIM model for organics sandwiched between two electrodes with different *WF* (anode with $E_{F,a}$ and cathode with $E_{F,c}$) at different applied voltages along the *JV*-curve (b).

From the **Equation 2.3.1**, the characteristic points on the curve, open-circuit voltage (V_{oc}) and short-circuit current density (J_{sc}) can be derived by substitution of J=0 and V=0 respectively (**Equation 2.3.2 and 2.3.3**; **Figure 2.3.1.-a**).[47]

For an ideal device, R_p is infinitely high, which makes the V_{oc} dependent only on the current of photo-generated charges. Also, if R_s in an ideal device is infinitely small, J_{sc} is nearly equal to the J_{ph}. In general, the V_{oc} of OSCs increases logarithmically with the intensity of incident light and finally saturates upon reaching of the maximum Fermi-level splitting possible in the D/A system.[48] Recombination at (non-selective) interfaces and within the photo-active layer due to poor nano-morphology leads to apparent lowering of the shunt resistance and reduces the V_{oc} (**Figure 2.3.2.-b**).[49, 50]

The J_{sc} is limited by the efficiency of a number of individual processes in the device: light absorption, exciton dissociation, charge transport in organics and collection at the electrodes. For a device with an optimized morphology and suppressed bimolecular recombination rate, the J_{sc} depends linearly on the light intensity, until the charge photo-generation

overwhelms the charge extraction and the current becomes space charge limited.[51] Interestingly, the photo-current increases at higher operation temperatures due to thermally enhanced charge carrier hopping transport mobility.[51]

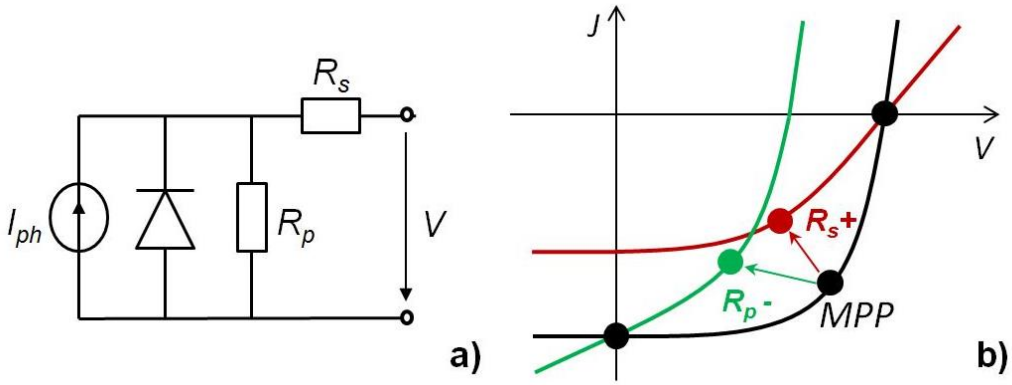

Figure 2.3.2. Equivalent circuit of a solar cell in the fourth quadrant of the *JV*-curve (a); schematic illustration of the *FF* evolution for increasing series resistance (R_s+) and decreasing parallel resistance (R_p-) in the solar cell (b).

In the power generating regime (fourth quadrant), the maximum possible generated power of the device for a given illumination can be derived from the power-voltage (*PV*) curve (**Figure 2.3.1.-a**). The corresponding point of the *JV*-curve is assigned to maximum power point (*MPP*), as shown in **Figure 2.3.1.-a**. With voltage and current density at device *MPP* being V_{mpp} and J_{mpp} respectively, the quality of the device can then be described by the following expression for the device fill factor (*FF*):

$$FF = \frac{J_{mpp} \cdot V_{mpp}}{V_{oc} \cdot J_{sc}} \qquad (\mathbf{2.3.4})$$

In general, *FF* is a combinatory device characteristic, which describes an interplay of the effects introduced by device R_s and R_p, associated with underlying physical processes in the device, as discussed above.[52-55] As demonstrated qualitatively in **Figure 2.3.2.-b**, the device *FF* is reduced

either via increasing R_s (red curve), or decreasing R_p (green curve), as the *MPP* moves closer to the coordinate origin.[56].

Finally, the power conversion efficiency (*PCE*) of the solar cell is calculated from discussed characteristic device values:

$$PCE = \frac{P_{out}}{P_{in}} = \frac{J_{mpp} \cdot V_{mpp}}{P_{in}} = \frac{FF \cdot J_{sc} V_{oc}}{P_{in}}, \qquad (\mathbf{2.3.5})$$

with P_{out} – generated maximum power density, P_{in} – standardized illumination power density of AM1.5G (air-mass global) spectrum of 100 mW/cm^2.

For better understanding of the *JV*-curve and the rectifying behavior of OSC, the metal-insulator-metal (MIM) model (**Figure 2.3.1.-b**) may be applied, as the organic materials are usually intrinsic semiconductors. After a photon absorption and exciton dissociation, free charge carriers must undergo drift through the BHJ, which relies on the built-in potential stemming from the difference of electrode *WF*s.[57] Following this difference, the electrostatic potential changes linearly for a non-doped semiconductor in-between.

For $V<0$ (**Figure 2.3.1.-a** and **b**), the built-in potential difference in the device is enhanced by external field, increasing with an absolute value of *V*, which is favorable for pronounced useful current of holes to the anode and electrons to the cathode. The reverse current through the ideal device under illumination is independent from negative bias and saturated by the finite number of incident photons that generate excitons. For $V=0$, the driving force for J_{ph} is supplied by the built-in potential and the associated built-in field, which is ideally sufficient to provide $J_{sc}(V=0)=J_{ph}(V<0)$. As this built-in field is overcompensated via externally applied positive voltage close to V_{oc}, the J_{ph} becomes more limited and is canceled at the open-circuit condition ($V=V_{oc}$). For positive external voltages $V>V_{oc}$, the injection of holes via anode and electrons via cathode prevails and determines the positive diode injection current in the first quadrant.

According to MIM model, the V_{oc} of the device is restricted by the *WF* difference between anode and cathode [58], which should be at least as large as the energetic offset between $LUMO_A$ and $HOMO_D$ in order to benefit from the entire potential given by polymer:fullerene system. However, additional interface phenomena (Fermi-level pinning, interface dipoles – to be discussed in the **Chapter 2.4**) specific for a particular material and material combination may substantially influence the electronic alignment on contact and, therefore, the V_{oc}.[59-63]

2.4. Charge extraction interfaces

As summarized in the previous chapter, energetic interface extraction barriers due to non-ohmic contacts and leakage currents due to non-selective charge extraction layers induce a massive loss of internally photon-to-electron converted energy. Therefore, a proper energetic alignment between organics of each phase to the corresponding charge extraction (inorganic) layers is required.

Even though the energetics at the organic/inorganic interface can be very complex, the first approximation of general trends relying on equilibrium of chemical potential on contact can provide essential insight into relevant interface formation (**Figure 2.4.1**).

First, the interface of donor and acceptor with ITO substrate is analyzed, as ITO is typically used as a transparent bottom electrode for OPV. Being highly doped, ITO demonstrates quasi-metallic behavior. Its Fermi-energy typically falls in the gap of both D-polymers and A-fullerenes. On contact, charge transfer typically occurs in order to equilibrate the Fermi-levels of ITO and organics.[64] The Fermi-levels of photo-active polymers lie typically deeper than the E_F of ITO (4.7-4.9 eV), which initiates electron transfer from ITO into the polymer. For the fullerenes the opposite charge transfer takes place regarding their Fermi-level above the E_F of ITO.[65] The band bending and the formation of the space charge region as a consequence of the charge transfer occurs (**Figure 2.4.1.-a**).

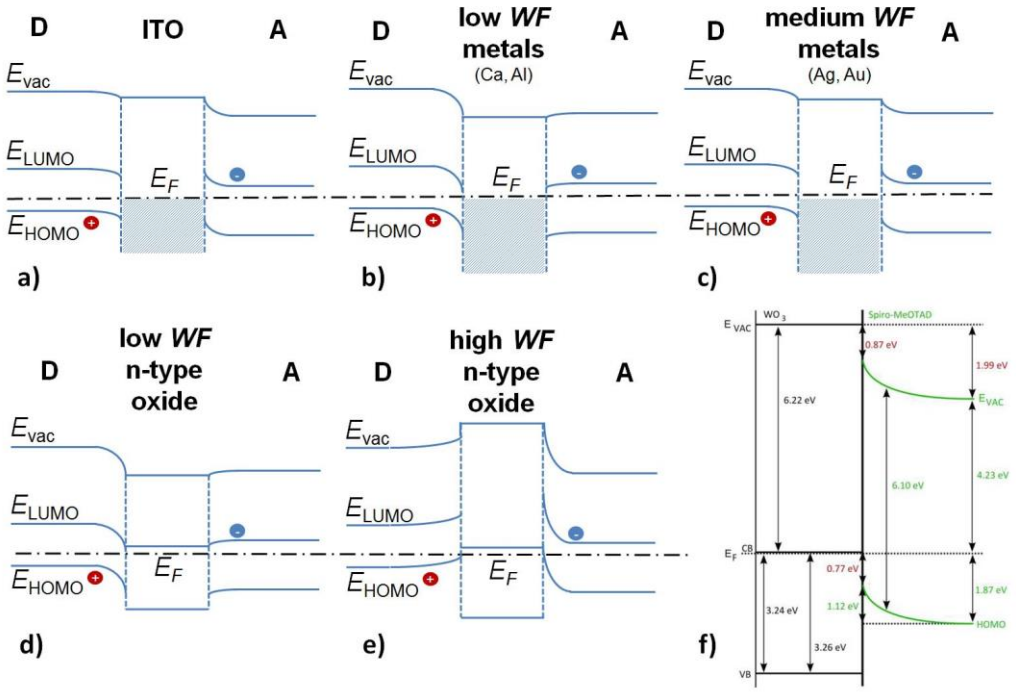

Figure 2.4.1. Simplified vacuum-level-aligned energetic scheme of organic / inorganic interfaces (D/substrate, A/substrate) with substrates: ITO (a), low *WF* metals (b), medium *WF* metals (c), low *WF* metal oxides (d), high *WF* metal oxides (e); an example of the experimentally observed band bending combined with the formation of the interface dipole at the high WF metal oxide/organic interface (f) [66].

The width of the bended region is limited by the screening due to charge carriers and the relatively small dielectric constant of organic materials. In addition, a spatial overlap of conducting orbitals between the van der Waals bound molecules is rather small for a long-range charge transfer. Thus, the band bending is spatially confined to the very first tens of nm [67] from the interface. In the ITO, bend bending can be neglected due to a high carrier density and typically large amount of ITO surface trap states.[64, 68, 69] The resulting electrostatic scheme reflects the Schottky-type contact at both ITO/polymer and ITO/fullerene interfaces.[70, 71] With this, ITO can be neither used efficiently as an anode, nor as cathode, as the holes from $HOMO_D$ and the electrons from $LUMO_A$ experience the charge extraction barriers. In addition, there is no charge carrier type

selectivity and no exciton blocking at the interface between the ITO and typical photo-active layer moieties, as the electrons from $LUMO_D$ and the holes from $HOMO_A$ can easily access the ITO and leak. If interface dipoles are formed at these interfaces additionally to the band bending, they are found to typically further enhance the extraction barriers.[72-74]

Also for metal-organic interfaces (**Figure 2.4.1.-b** and **c**), the charge extraction efficiency cannot be predicted simply by the difference of individual electronic structure relying on vacuum level (E_{vac}) alignment.[75-77] A sophisticated interplay of Pauli "push-back" (repulsion of the electron density that is evanescent into vacuum at the substrate surface back into the substrate bulk due to the interaction with the frontier orbitals of adsorbing molecules), charge transfer and formation of interfacial dipoles takes place determining the final contact energetics.[78-81] However, as an interface dipole (supported by metal electrons) formed upon adsorption of organics on metal typically decreases the metal *WF* and the Fermi-level of metal pins to the LUMO of fullerene, low *WF* metals (Ca, Al) can be used to form an ohmic contact [82-84] with fullerenes for facilitated electron extraction, while simultaneously blocking the holes from the polymer (**Figure 2.4.1.-b**). In analogy to highly doped ITO, the formation of a space charge region is neglected in the metal. As the *WF* of the metal increases (**Figure 2.4.1.-c**), a charge extraction barrier for the electrons from the fullerene arises. Simultaneously, the charge extraction barrier for holes from the donor decreases, but still remains due to insufficient difference of chemical potentials of the polymer and the metal. Therefore, the medium *WF* metals (Ag with 4.6 eV, Au with 4.8-5.0 eV) cannot be used either for electron, or for hole extraction.

To modify the ITO/organics or metal/organics interfaces in order to gain efficient and selective charge extraction, n-type (due to entropy driven oxygen deficiency) [85] metal oxides have found wide-spread application on both anode and cathode side (discussed in detail in **Chapter 3**). Note,

some high *WF* p-type metal oxides, like NiO_x[86] and CuO_x[87], were also shown to favorably modify the anode *WF* in OSCs.

The energetic alignment of the organics at the low *WF* oxide surface results in enhanced electron extraction from the fullerene (oxide *WF* < *EA* of fullerene) with simultaneous blocking of holes from the fullerene and the polymer (**Figure 2.4.1.-d**). This makes the low *WF* metal oxides ideal candidates for the cathode interface.

At the anode side, high *WF* n-type metal oxides are expected to match the $HOMO_D$ and effectively p-dope [66, 88-91] both the polymer and the fullerene, thus, creating the prerequisites for efficient hole extraction from the polymer and rejection of electrons from both $LUMO_D$ and the fullerene (**Figure 2.4.1.-e**). Interestingly, for exceedingly large metal oxide *WF*, the enhanced electron transfer from the polymer to the metal oxide is expected to push the $HOMO_D$ into the resonance with the Fermi-level level of the D and, thus, would ultimately degenerate the organic semiconductor. In reality, the bended $HOMO_D$ pins several tenth of an eV below the Fermi-energy of the oxide.[92, 93] In addition, the formation of an interface dipole is often found (**Figure 2.4.1.-f**) [66] enhancing the built-in field in the device.[59, 94]

2.5. Device architectures

Regarding the device architecture of OSCs, one distinguishes the regular layer sequence with the anode as bottom (substrate) electrode. Opposed to that, in the inverted setup the bottom electrode is the cathode. The regular OSC stack structure is depicted in **Figure 2.5.1.-a**. The transparent substrate (glass, plastic foil etc.) is coated with a transparent conductive oxide (TCO) as a bottom electrode. Typically a mixed phase ITO is used as TCO for it exhibits a high transparency and low sheet resistance. In regular device structure, the TCO is modified by thin films of high *WF* (>5.1 eV) transparent materials (polymers, oxides) or dipole-inducing ultra-thin organic films to form the anode interface and facilitate

hole extraction. Afterwards, the photo-active organic BHJ layer is introduced. At the cathode side, a low WF interlayer combined with a metal to electrode or directly a sufficiently low *WF* metal is used (see **Chapter 2.4**) for efficient electron extraction.

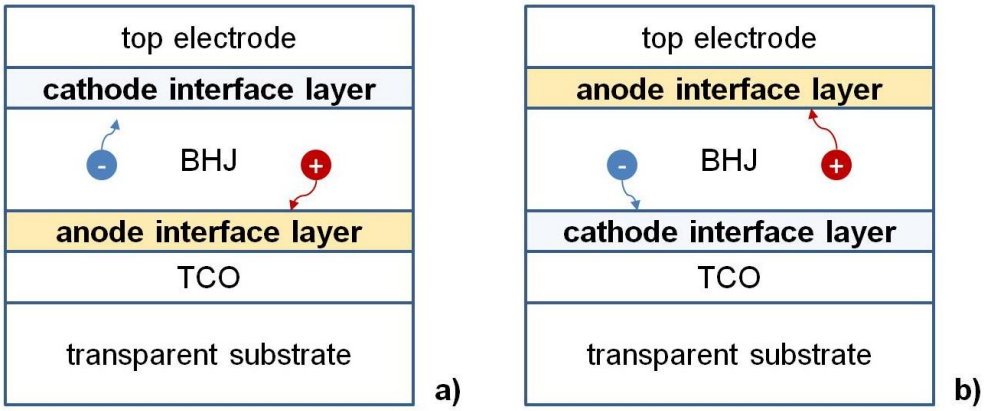

Figure 2.5.1. OSC stack in regular (a) and inverted (b) layout.

For enhanced device lifetime, the inverted stack layout (**Figure 2.5.1.-b**) might be beneficial to some extent.[95] For this "flipped" structure, environmentally stable high *WF* materials are utilized at the top electrode avoiding the oxidation of low *WF* metals (Ca, Al, etc.) typically used in regular devices. In addition, it was demonstrated that polymer:fullerene BHJs often exhibit thermo-dynamically driven vertical concentration gradients of donor and acceptor.[96, 97] If the acceptor fraction is increased towards the substrate, the deposition of the cathode interlayer on the TCO results in more efficient electron extraction.[98, 99]

The concrete stack materials and details of device fabrication within this work are discussed in detail in **Appendix B.1**.

3. Solution-processed high work-function metal oxides

The photo-active organic materials used in OPV are not intentionally doped. Thus, unlike in inorganic p-n-junctions, no space charge region is formed on contact between polymer (D) and fullerene (A). For this reason, the built-in potential difference over the device, which is a driving force for spatial "free" charge separation, must be provided from charge extraction electrodes. In other words, the photo-active film must be sandwiched between two materials with significantly different work functions: high *WF* material on the anode and low *WF* material at the cathode. In addition, to facilitate the extraction of generated charges, these materials must electronically match the $HOMO_D$ and $LUMO_A$ at the anode and the cathode side respectively.

Specifically on the anode side, a high *WF* (5.1 eV) material, polyethylene-dioxythiophene:polystyrenesulfonate (PEDOT:PSS), is typically applied [100-107], for it is relatively cheap and can be comfortably processed from an aqueous dispersion. Unfortunately, PEDOT:PSS is also known for its structural and electrical inhomogeneity [108, 109] and it is capable of deteriorating the device performance on a relatively short time scale due to its acidic nature and aqueous residue in a device after the processing [110-114].

As an alternative to PEDOT:PSS, high work-function (up to 7 eV) transition metal oxides (TMOs), like V_2O_5, MoO_3 and WO_3, have been proven to be promising candidates for hole extraction.[92, 115-119] These materials are typically processed under high vacuum conditions via physical vapor deposition.

These materials have been shown to be n-type semiconductors with unusually high electron affinity (EA) of 6.5 to 6.7 eV and a valence band edge close to 10 eV.[67, 91, 92, 119-121] Thus, the extraction and transport of photo-generated holes via the valence band of the metal oxide is prohibited. Instead, a mechanism was proposed, according to which an equivalent flow of electrons via the CB or gap states (of sufficient density)

of the metal oxide towards the organics and electron injection into the $HOMO_D$ with immediate recombination with a hole takes place (**Figure 3.1**).[93, 119, 122-124]

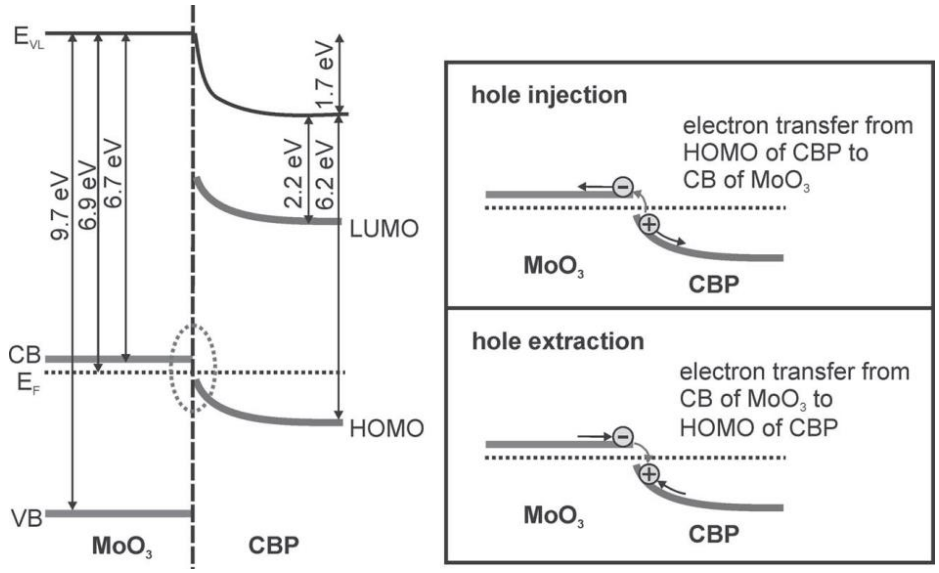

Figure 3.1. Energy level alignment at the MoO_3/4,4'-bis(N-carbazolyl)-1,1'-biphenyl (CBP) interface deduced from the UPS spectra (left) and proposed hole-injection/extraction mechanism (right).[93]

As the minimum of CB is typically several eV below the LUMO of the electron-conducting fullerenes used in the BHJs, no electron blocking properties can be assigned to this class of metal oxides. Nevertheless, parasitic recombination losses at flat band condition are somewhat suppressed due to a space charge region formation at the interface and an upward band bending [67, 117, 125-128] rejecting the electrons. In addition, due to their extraordinary high *WF* these metal oxides are capable to interface to organic materials even with energetically deep HOMO levels.[92, 93, 129, 130]

With growing understanding of the energetics of high *WF* oxides, much effort has been undertaken in recent years to process these materials from solution. This will be the subject of the following sections.

3.1. Evaluation of existing solution-based deposition techniques for high work-function metal oxides

Meeting the technological issues of R2R processing, this work is focused on low-temperature preparation of metal oxide films from solution. The solvent of the dispersion or the precursor solution must be compatible with plastic substrates or the organic photo-active material, if deposited on top of it. Typically, environmentally benign alcoholic solvents are preferred. Further, depending on the chemistry of the metal oxide dispersion or precursor solution and the processing temperature, organic residues might be present in the layers after processing, whose impact on device characteristics is to be evaluated individually.

An intensive study was carried out in recent years on high *WF* metal oxides (MoO_3, V_2O_5, WO_3, NiO_x) spin-casted from nano-particle (NP) dispersions.[131-138] The great advantage of this approach is the possibility to prepare the materials with their required electronic properties even under chemically aggressive conditions and without limitations in process temperatures. The subsequent deposition on the sensitive substrates or organic active layers can be done under inert and low temperature conditions. Despite that, several drawbacks drive this approach less attractive. Relatively large particle size (15-100 nm) results often in incomplete or inhomogeneous surface coverage or high surface roughness of the films and may cause short circuits or recombination losses in devices.[131, 139] The proper functionality of NP-layers is guaranteed only for thicker coatings (30–100 nm), which mostly corresponds to higher series resistance in the device. In order to avoid the agglomeration of NPs in polar solvents, driven by the low surface energy of relatively large particles, for the ink formulation polymeric dispersing agents are often used. They must be subsequently removed e.g. by O_2-plasma or UV-ozone treatment to access the unique electronic structure of the metal oxide. In addition, post-bake at 200-350°C is often needed to “glue” the NPs together. Very recently, it was demonstrated that the

mixing of NPs with the conductive polymeric matrix of PEDOT:PSS can smoothen the film surface by filling the voids [140], but usage of PEDOT:PSS in OE devices should be minimized for reliability issues discussed above.

The hybrid NP/sol-gel approach, were the sol-gel formulation is prepared by H_2O_2- or H_2O-oxidized metal oxide powder, shares essentially the same obstacles, as the pure NP-route.[141-144]

In contrast to that, the sol-gel technique (see also **Appendix B.3** for detailed mechanism) based on highly reactive metal-organic precursors might allow for low-temperature (down to *RT*) processing and uniform metal oxide coatings. Many sol-gel recipes are adopted from previous works focused on catalytic, gas sensing and electrochromic applications.[144-162] The films must have undergone high temperature treatment 250-600°C, as a specific crystallinity or stoichiometry was desired. Nevertheless, the needs of OE are often satisfied already by the corresponding materials in their amorphous phase. With this in mind, several groups successfully lowered the processing temperatures to 100-150°C by utilizing metal-alkoxides and β-diketonates.[163-166]

In this work, even milder wet-chemical processing of high quality vanadium and molybdenum oxide films is presented keeping the focus on the efficiency of OSCs. It should be mentioned that due to processing on ambient air, influence of adsorbates and imperfections of the sol-gel technique, slightly substoichiometrical (to be discussed in the following) metal oxides are formed. Therefore, the modified notation of VO_x and MoO_x (instead V_2O_5 and MoO_3) is to be used for the discussion.

3.2. Sol-gel processing and device application of vanadium (V) oxide

In the following, VO_x films for hole extraction spin-coated from a solution of vanadium(V)oxitriisopropoxide (**Figure 3.2.1**) in anhydrous isopropanol are studied.

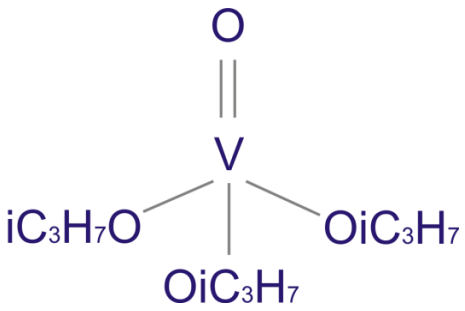

Figure 3.2.1. Molecular structure of vanadium(V)oxitriisopropoxide.

The DLS analysis on a pre-hydrolyzed and partially cross-linked precursor solution reveals clusters with 3 nm in size. As can be seen in **Figure 3.2.2**, a sVO_x-surface with extremely low surface roughness of 0.4 nm rms is obtained, which is attractive especially for large-area thin-film devices. The nano-scopic voids seen on the AFM image are typical for films processed under these conditions and are the result of solvent evaporation.[167, 168] Their eventual influence on the macroscopic electronics is shown to be of minor importance. The XRD analysis of the film doesn't reveal any characteristic diffraction peaks related to (poly) crystal phases. It can be therefore stated that the sVO_x films are predominantly amorphous.[146]

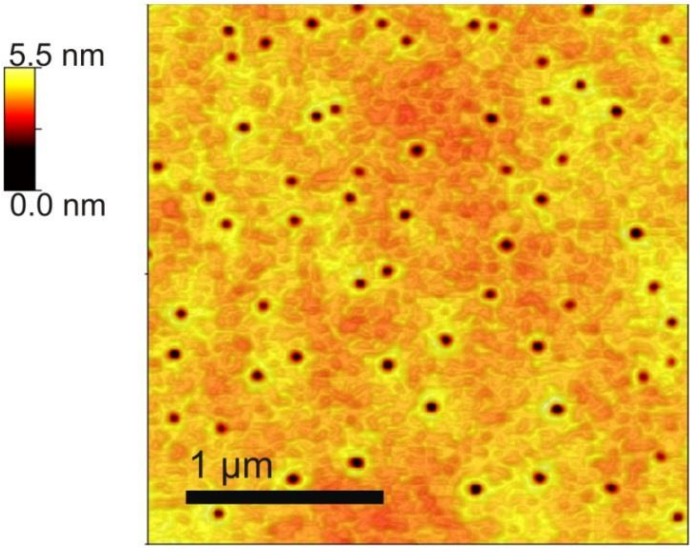

Figure 3.2.2. AFM tapping mode topography image of the sVO_x layer.

No heat or plasma-cleaning is applied to the films after deposition. As the sol-gel layer is formed as a result of chemical reaction between the metal-organic compound and moisture, a small fraction of residual organics originating from alcoholic byproducts and/or non-reacted species may be expected. Probing the elemental composition of the films via XPS (**Figure 3.2.3**) reveals the carbon 1s peak for sVO_x, indicating a portion of carbon of 15 at%, which is in contrast to carbon-free surface of the thermally evaporated counterpart eV_2O_5. The C 1s peak can be found in case of thermally evaporated vanadium oxide layers after an exposure to ambient air (cV_2O_5). This hints to adsorbates as the source of the carbon signal.

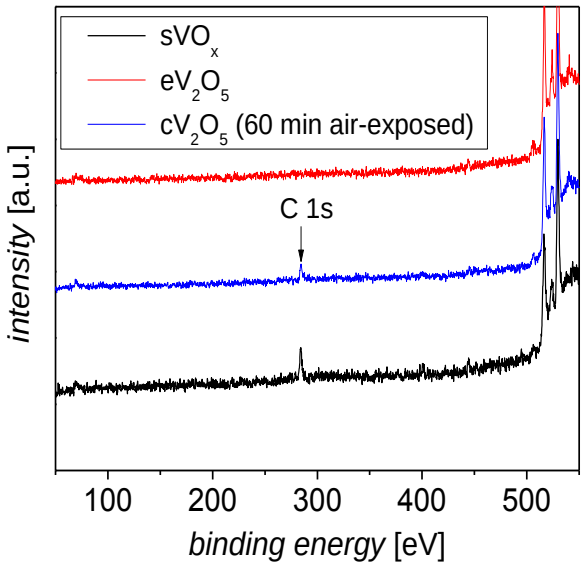

Figure 3.2.3. The characteristic carbon (C 1s) peak in XPS spectrum of vanadium oxide layers: sol-gel processed sVO_x, thermally evaporated in high vacuum eV_2O_5 and through air-exposure contaminated evaporated cV_2O_5. Collaboration with Princeton Univ.

The appearance of V $2p_{3/2}$-peaks (**Figure 3.2.4**) for solution-processed and air-contaminated evaporated films is broadened to lower binding energies, as compared to clean V_2O_5. Applying the Lorentzian-Gaussian fit to the broadened spectral region reveals an additional peak at 515.5 eV, which is in the very proximity to reported crystalline VO_2 [169].

Therefore, the formation of reduced sub-stoichiometric species with V^{4+} states at V $2p_{3/2}$ during air exposure due to adsorbates is stated. The ratio of V^{5+} to V^{4+} for cV_2O_5 and sVO_x is calculated to 5.6 and 3.3 respectively. The V-atoms in the metal-organic precursor complex exhibit 5+ oxidation states. Thus, the lower V^{5+}-to-V^{4+} ratio for sol-gel VO_x cannot be associated with unreacted precursor species present in the film, but may result due to excessive air exposure during the film formation resulting from the gel densification.

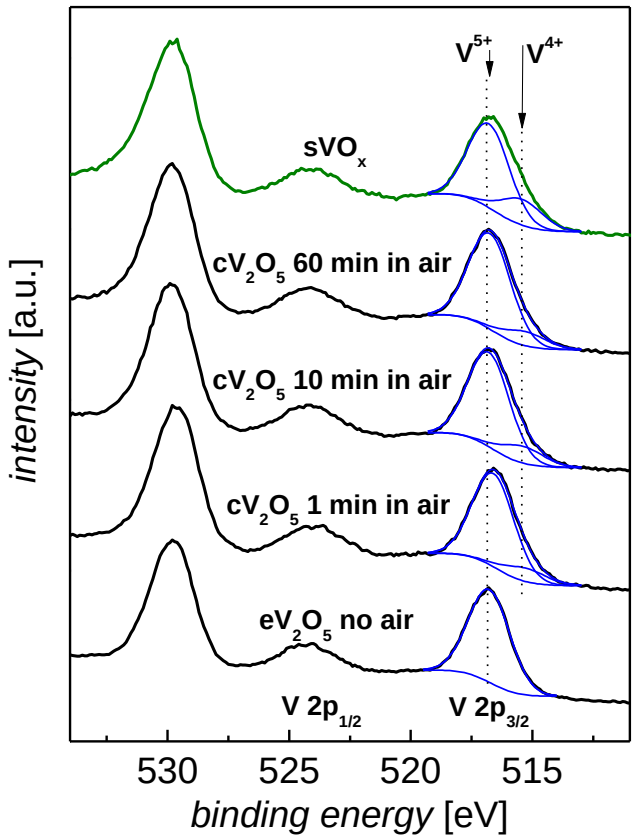

Figure 3.2.4. The characteristic vanadium 2p-peaks in XPS spectrum of vanadium oxide: sVO_x, eV_2O_5 and through air-exposure contaminated evaporated cV_2O_5. Collaboration with Princeton Univ. (group of Prof. A. Kahn).

The impact of adsorbates on the electronic structure of the surface of vanadium oxide is derived from UPS/IPES spectra and depicted in **Figure**

3.2.5. The sol-gel derived VO_x exhibits an essentially similar band diagram as the air-contaminated cV_2O_5. Both exhibit the states in the bandgap below the E_F provided by the adsorbates. An apparent widening of the band gap is observed during the air-exposure. A similar effect was observed in earlier works on vanadium oxide intercalated with Na or Li, where the split-off conduction band (present in the structure of V_2O_5 below the edge of CB) was filled via charge transfer from the alkali metal.[170-172] In case of solution-based VO_x, the reduction of the metal might correlate directly with filling of the split-off CB, formed predominantly by the metal orbitals, via donating adsorbates.

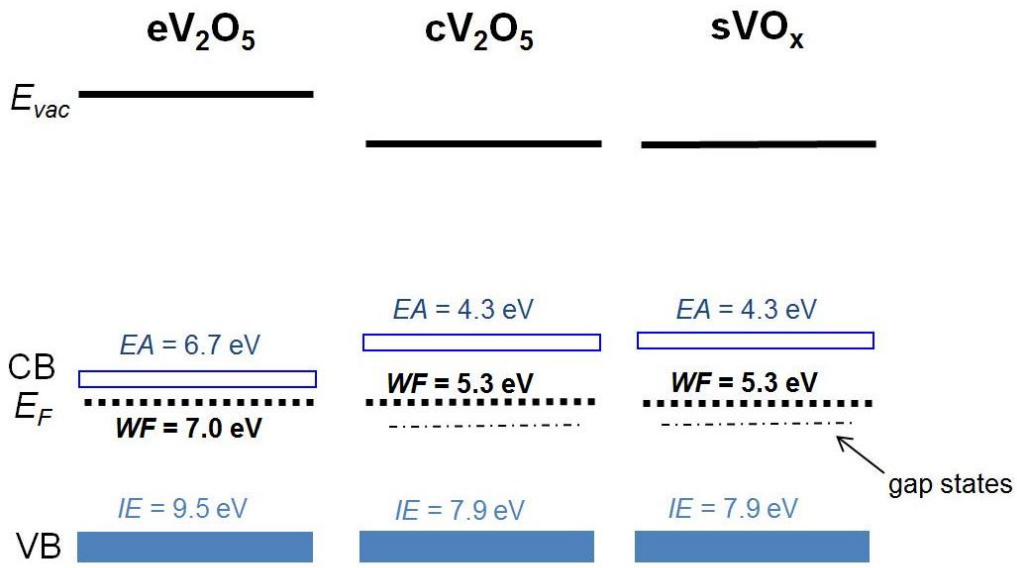

Figure 3.2.5. The electronic structure of vanadium oxide films derived from UPS/IPES measurements. Collaboration with Princeton University (group of Prof. A. Kahn).

The *WF* of eV_2O_5 is significantly lowered upon air exposure (from 7 eV to 5.3 eV), which is in agreement with observations for vacuum-processed films in other groups.[173, 174] More importantly, the *WF* of 5.3 eV (or 5.6 eV as estimated alternatively from KP analysis) is also valid for layers processed completely in air from solution and without any post-deposition

treatment. This *WF* is significantly higher than that of PEDOT:PSS (5.1 eV) and allows for efficient hole extraction in OSCs.

To demonstrate that, OPV devices in regular architecture (**Figure 3.2.6.-a**) with layer sequence glass/ITO/sVO_x or PEDOT:PSS/P3HT:$PC_{60}BM$/Al/Ag were fabricated. For ease of processing and for efficient electron extraction from the BHJ, low *WF* aluminum is evaporated on the cathode side. As can be seen in **Figure 3.2.6.-b** and in **Table 3.2.1**, devices with optimum thickness of sVO_x outperform the optimized PEDOT:PSS cells with *PCE* of 2.7% having *PCE* of 3%.

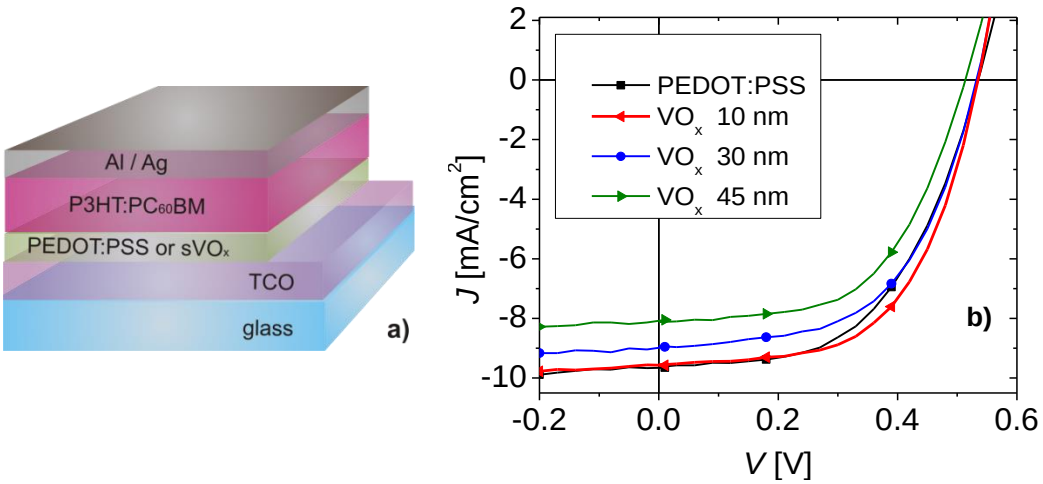

Figure 3.2.6. Stack of the studied regular OSCs (a); *JV*-curves of devices with sVO_x interlayers in comparison to PEDOT:PSS devices under AM1.5G, 100 mW/cm^2 (b).

Table 3.2.1. Characteristics of regular OSCs with sVO_x interlayer in comparison to PEDOT:PSS devices.

	PCE [%]	V_{oc} [V]	J_{sc} [mA/cm^2]	*FF* [%]
w/o interlayer	0.6	0.26	7.5	32
PEDOT:PSS	2.7	0.53	9.7	54
sVO_x 45 nm	2.4	0.52	8.4	59
sVO_x 30 nm	2.5	0.52	8.7	56
sVO_x 10 nm	3.0	0.53	9.6	59

Further, the impact of the sVO_x film thickness (10 to 45 nm) on the performance of OSCs is verified by adjusting the spin-velocities during the film deposition. For thicker sVO_x films the efficiency drops dramatically, as the photo-generated current becomes lower (**Table 3.2.1**).

The electrical conductivity of a TMO was shown to originate from oxygen deficiency states [120] and can vary by orders of magnitude, depending on their density [175]. The electrical conductivity of sVO_x is estimated to 10^{-5} S/cm, which is somewhat lower than for vanadium oxide processed via ALD [176]. However, as the *FF* for OSCs with thicker VO_x films remains unaffected, the series resistance in the bulk of the thicker VO_x film cannot play a crucial role in J_{sc} drop. As the thicker films appear more yellowish, the intrinsic photon absorption in the bulk of VO_x is assumed resulting in less photo-current, as the light has to pass through the VO_x covered TCO previous to useful absorption in the photo-active layer.

The absorption coefficients are calculated from the optical transmission measurements on sVO_x films and plotted in **Figure 3.2.7-a**. Applying the Tauc's law [177] to the absorption spectrum (**Figure 3.2.7.-b**), the bandgap of roughly 2.3 eV for sVO_x is determined, which is in good agreement with other works [144, 160, 178]. A clear absorption on-set is seen at 540 nm, which is close to the absorption maximum of the active blend (P3HT:$PC_{60}BM$) used in studied devices.

At this point, it is important to distinguish between the bandgap in the oxide bulk, accessed by the optical absorption measurement (**Figure 3.2.7.-b**), and the bandgap derived from the surface sensitive spectroscopic measurements for sVO_x (**Figure 3.2.5**), as the above discussed widening of the bandgap due to adsorbates is confined to the oxide surface.

Despite the significant overlap of absorption spectra for sVO_x and P3HT:$PC_{60}BM$, the absorption losses associated with this can be neglected for VO_x films thinner than 20 nm, as 99% of light at 500 nm close to absorption maximum of the polymer is still transmitted.

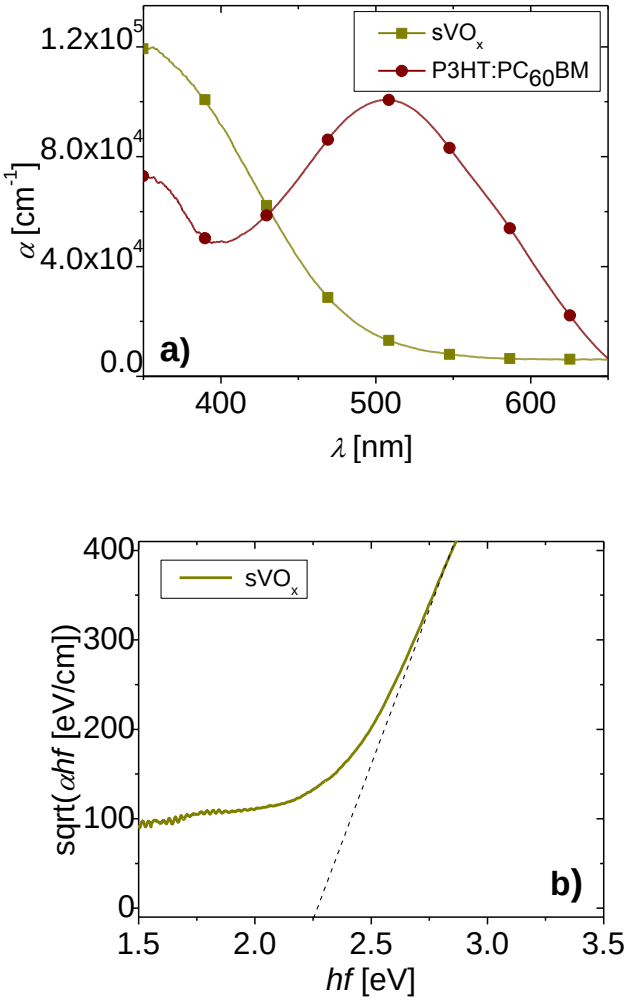

Figure 3.2.7. Plot of absorption coefficients of sVO_x confronting with absorption plot for P3HT:$PC_{60}BM$ (a); Tauc's plot derived from transmission spectra of sVO_x films (b).

For a current state of the technology it is difficult to foresee, if sol-gel metal oxides can be processed via R2R techniques (ink-jet printing, slot-die coating etc.) to achieve thin films <20 nm, as only little work has been done on development of ink formulation with adjusted viscosity, solvent evaporation rate and so on. If thicker layers of solution-based metal oxide will be required by the manufacturing process, other high *WF* TMOs, e.g. molybdenum oxide with its wide bandgap of 2.9 to 3.1 eV [179, 180] may become an attractive alternative to sVO_x.

3.3. Sol-gel processing and device application of molybdenum (VI) oxide

The sol-gel approach to prepare molybdenum oxide presented in this work is based on bis(2,4-pentanedionato)-molybdenum(VI)dioxide (see **Figure 3.3.1**) as a precursor and isopropanol as a solvent. In case of this somewhat less reactive (hydrolytic sensitivity class 7) precursor, isopropanol containing a small portion of water (< 0.1 %) is used in order to promote the cross-linking of the sol during the stirring. For the same reason, the minimal *rH* of 65% is also required during the subsequent precursor conversion via hydrolysis.

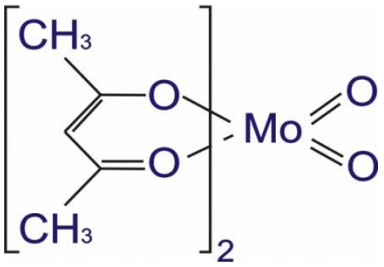

Figure 3.3.1. Molecular structure of Bis(2,4-pentanedionato)molybdenum(VI)dioxide.

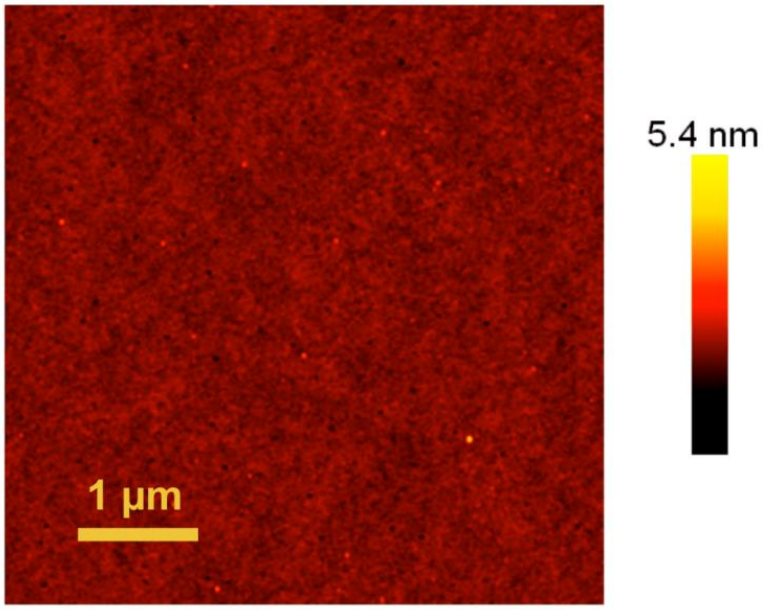

Figure 3.3.2. The AFM topography image of sol-gel processed MoO_x.

Also for $sMoO_x$ precursor solution a very small initial particle size < 1 nm previous to spincoating is found via DLS, which is beneficial for smooth and continuous films with complete surface coverage. This is confirmed via the AFM measurement of the $sMoO_x$ surface (**Figure 3.3.2**) revealing the surface roughness of less than 3 nm rms. Again some nano-scopic voids (similar to sVO_x films discussed above) characteristic for sol-gel deposition technique can be seen. The films are predominantly amorphous, as verified by XRD.

For *RT* as-deposited $sMoO_x$ films, the XPS spectrum of the C 1s peak is shown at **Figure 3.3.3**. The signatures of C-C, C-O and C=O bonds are resolved. These can either be assigned to the adsorbates or to residues of the metal-organic precursor (**Figure 3.3.1**). The separation of these two contributions is impossible, as the samples are prepared ex-situ and are subsequently transferred to the XPS system. The relative carbon content can be estimated to be 29%. This is in stark contrast to non-reacted bis(2,4-pentanedionato)molybdenum(VI)dioxide molecule, for which a 60% ratio (excluding hydrogen atoms) is expected. Therefore, some decomposition of the precursor and subsequent loss of organic groups during the hydrolysis even at *RT* is evidenced. Note, the vapor pressure of AcAc at *RT* is roughly 8 mbar (Sigma Aldrich), and therefore substantially less than that of isopropanol (roughly 60 mbar).

Further considering the XPS spectrum of *RT*-processed (pristine) $sMoO_x$ film at 232.2 and 235.4 eV (**Figure 3.3.4**) the strongly dominating Mo^{6+} oxidation state is found. However, at this stage it is impossible to distinguish, whether the signal originates from the stoichiometric MoO_3 or from the precursor compound comprising molybdenum in 6+ oxidation state.

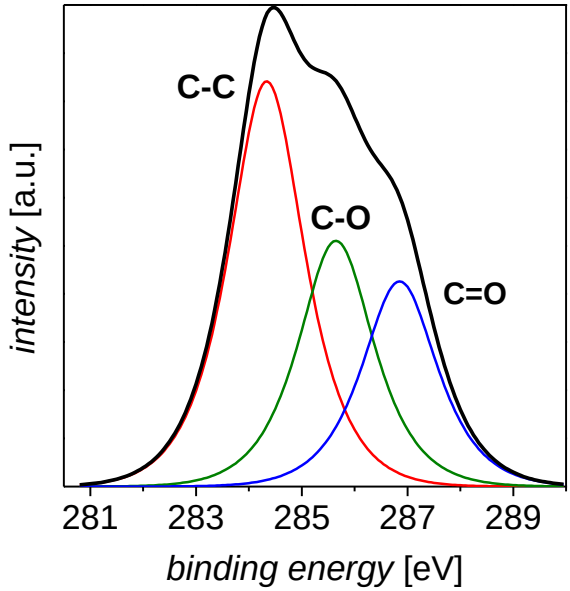

Figure 3.3.3. The XPS spectrum of $sMoO_x$ film at C 1s peak.

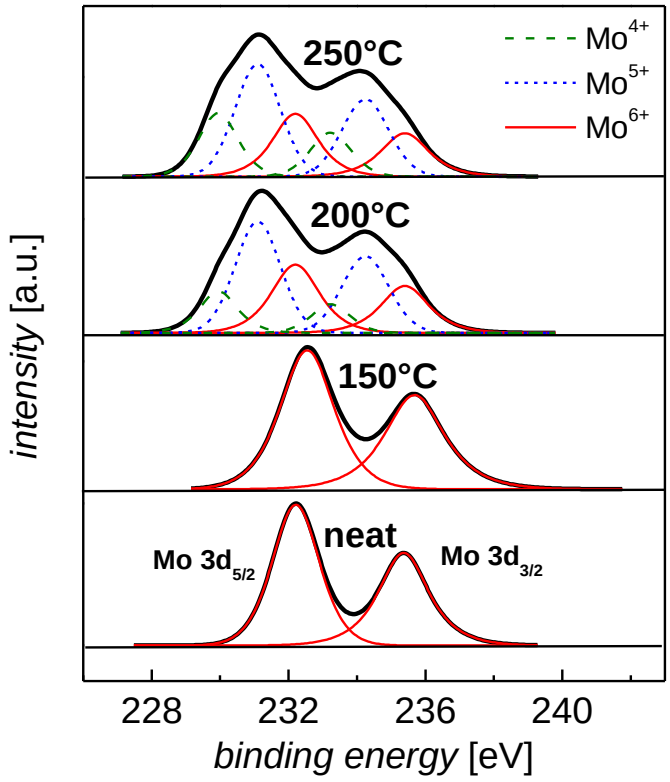

Figure 3.3.4. Normalized XPS spectra of $sMoO_x$ as-casted and thermally treated in N_2 for 20 min films at Mo 3d peaks.

With above discussed properties of sol-gel MoO_x in mind, the modification of the TCO *WF* via $sMoO_x$ for use in OSCs with regular stack structure glass/ITO/$sMoO_x$ or thermally evaporated MoO_3 ($eMoO_3$) or PEDOT:PSS/P3HT:$PC_{60}BM$/Al/Ag (**Figure 3.3.5-a**) is inspired.

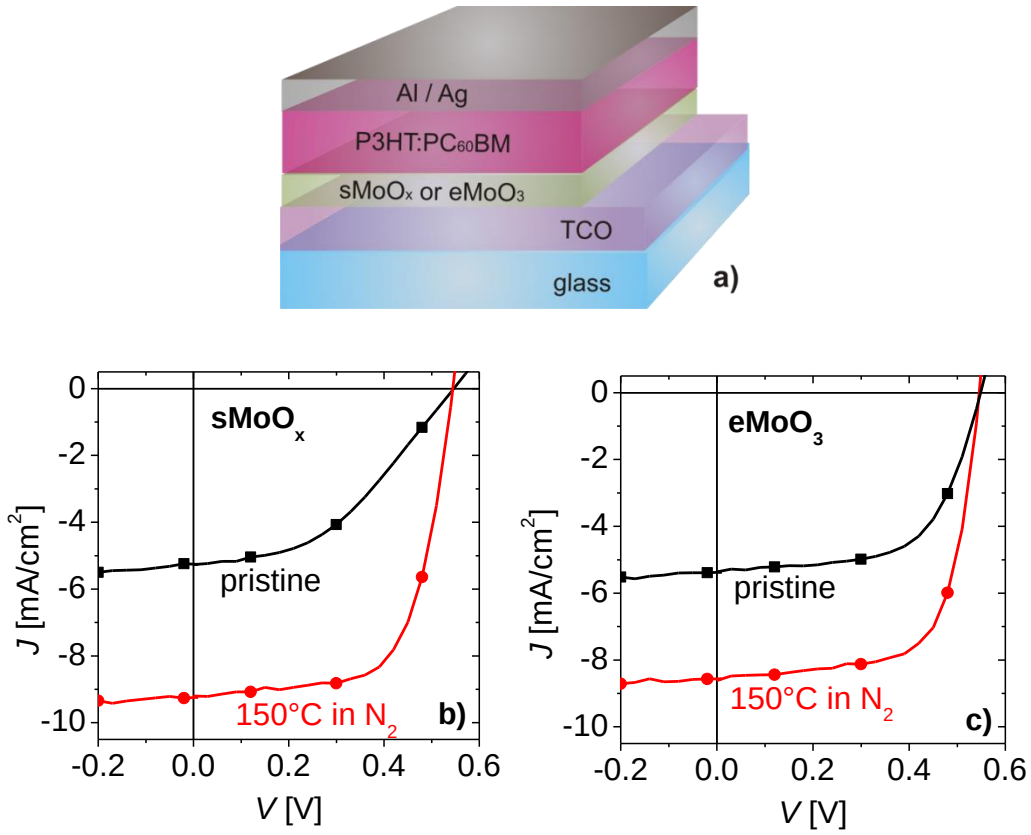

Figure 3.3.5. Regular OSCs studied (a); *JV*-curves of devices comprising $sMoO_x$ (22 nm) interlayers (b) in comparison to $eMoO_3$ (20 nm) devices under AM1.5G, 100 mW/cm^2 (c).

Using the pristine $sMoO_x$ films in the first run results in cell *PCE* of 1.3% (**Figure 3.3.5.-b** and **Table 3.3.1**) compared to 3.2% for optimized PEDOT:PSS device. Devices exhibiting a low J_{sc} of 5.3 mA/cm^2 and a poor *FF* of 44.5% clearly suffer from ohmic losses. The same low J_{sc} is found for devices with thermally evaporated $eMoO_3$, air-exposed previous to deposition of photo-active organics (**Figure 3.3.5.-c** and **Table 3.3.1**). Thus, the specific of the sol-gel oxide deposition is not necessarily responsible for deteriorated device performance.

Table 3.3.1. Characteristics of regular OSCs with $sMoO_x$ interlayer (optimized thickness of 22 nm) in comparison to $eMoO_3$ (optimized thickness of 20 nm) and PEDOT:PSS devices.

	PCE [%]	V_{oc} [V]	J_{sc} [mA/cm^2]	*FF* [%]
w/o interlayer	0.6	0.26	7.5	32
PEDOT:PSS	3.2	0.56	9.8	58
$sMoO_x$ pristine	1.3	0.54	5.3	45
$sMoO_x$ annealed 150°C@N_2	3.3	0.54	9.2	66
$eMoO_3$ air-exposed	1.8	0.55	5.4	61
$eMoO_3$ annealed 150°C@N_2	3.2	0.55	8.6	68

Keeping in mind the film thickness of molybdenum oxide in both devices with $sMoO_x$ and $eMoO_3$ of the order of 20-22 nm, such a low current cannot be associated with ohmic losses in the bulk of metal oxide, but is most probably coupled to surface energetics. Indeed, a surprisingly low *WF* of 4.9 eV for *RT*-processed $sMoO_x$ is found via KP analysis. The spectroscopic studies carried out on $eMoO_3$ by other group [181] indicate a drop of the oxide *WF* from 6.7 eV to 4.9 eV under air-exposure (**Figure 3.3.6**). For this, the formation of water dipoles or polar hydroxyl groups on the hydrophilic surface of molybdenum oxide is most probably responsible. The major role of moisture in reducing the *WF* of molybdenum oxide was also observed elsewhere.[182]

Similar to vanadium oxide, the bandgap of evaporated molybdenum oxide is widened from 3 to 3.8 eV and the gap states are formed via adsorbates. Again, the widening of the oxide bandgap derived from UPS/IPES spectra is confined to the oxide surface and not representative for the oxide bulk.

To demonstrate the presence of probable adsorbates on the oxide surface, the films were annealed in nitrogen-filled glovebox at 150°C for 20 min. Afterwards the KP analysis demonstrated the significant rise of *WF* by 0.4 eV resulting in the *WF* of $sMoO_x$ of 5.3 eV. It should be mentioned that annealing at such low temperatures did not affect the film morphology or surface roughness, as was verified via AFM (not shown

here). Also, no significant change of stoichiometry at 150°C in absence of oxygen was observed via XPS (**Figure 3.3.4**).

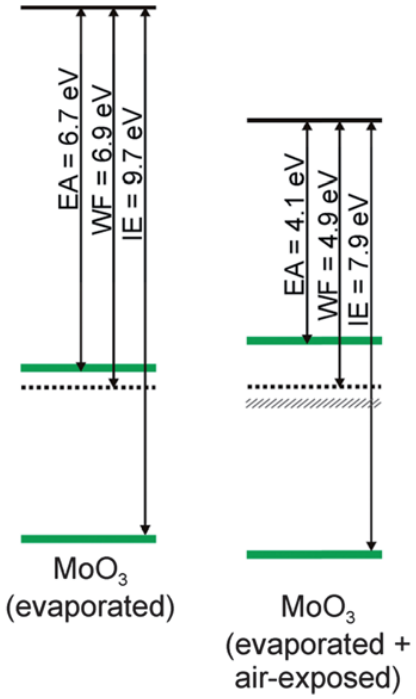

Figure 3.3.6. Energy diagrams of $eMoO_3$ [181] based on UPS/IPES results [92].

Interestingly, a neat precursor film spin-coated in absence of moisture exhibits the *WF* of 4.9 eV, which changes to 4.7 eV after the above mentioned heat treatment in N_2. This demonstrates that the hydrolytic precursor decomposition to an oxide in humid air takes place and is required to gain the high *WF* of 5.3 eV.

Following this annealing procedure for *WF* recovering, devices with enhanced 3.3% *PCE* for $sMoO_x$ and 3.2% *PCE* for $eMoO_3$ are fabricated (**Figure 3.3.5.-b,c** and **Table 3.3.1**) outperforming the PEDOT:PSS device in *FF*. Interestingly, $sMoO_x$ films that were annealed in N_2 and then again exposed to air (to allow for the sticking of adsorbatic species) for several minutes result in pronounced drop of device J_{sc} and *FF* by approx.1 mA/cm^2 and 10% respectively (not shown here). Thus, such behavior

again supports the assumption that the variations in the electronic structure of molybdenum oxide are due to adsorbates.

In order to gain more insight into the effects of annealing temperature and atmosphere and find the optimal device processing window, the $sMoO_x$ films were post-annealed in ambient air and in N_2 at temperatures from 100 to 300°C. The corresponding device characteristics are plotted in **Figure 3.3.7**. According to this, the optimal device efficiency is obtained for $sMoO_x$ heat-treated in N_2 at 130-150°C, which is favorable for R2R production on flexible foils. For both $sMoO_x$ and $eMoO_3$ the device characteristics improve during the first 20 min at 150°C in N_2 and then saturate (**Figure 3.3.8**).

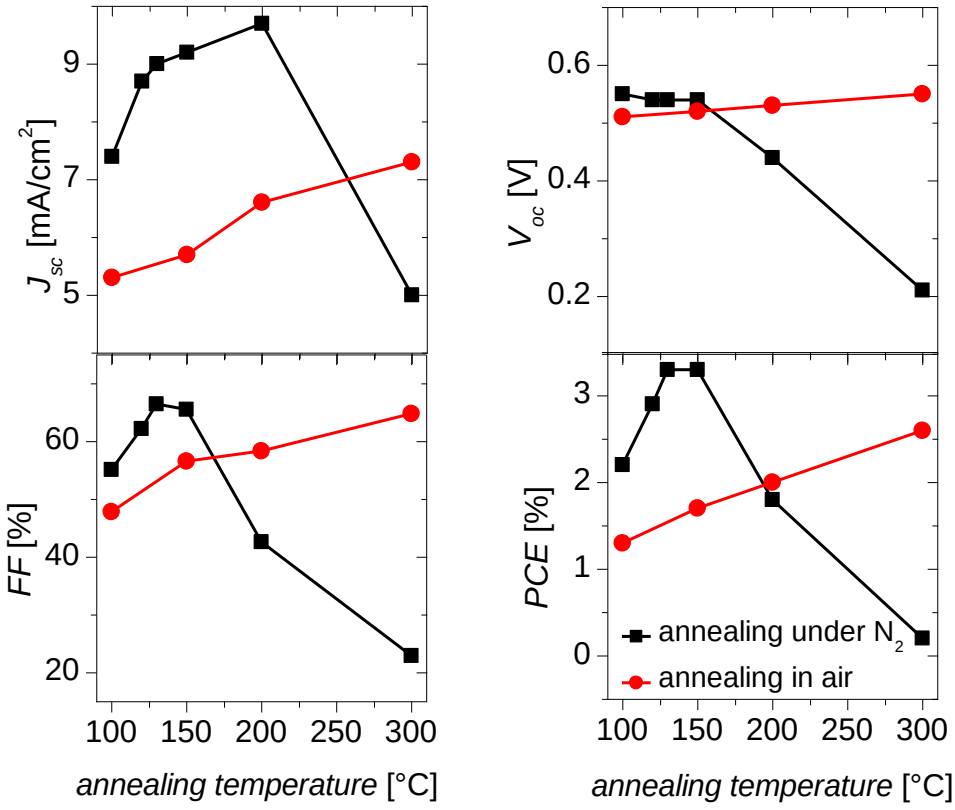

Figure 3.3.7. Characteristic of OSCs with $sMoO_x$ layer annealed (previous to deposition of the photo-active organics) in N_2 and in ambient air at various temperatures.

Temperatures below 130°C obviously cannot activate the desorption of the adsorbates from the surface, resulting in poor device *PCE* (**Figure 3.3.7**). On the other hand, going beyond 150°C results in rapid simultaneous decrease of J_{sc}, V_{oc} and *FF*. This is associated with semiconductor-to-metal transition of molybdenum oxide, whose thermo-chromic behavior is well-known.[160, 183] Indeed, the XPS spectrum (**Figure 3.3.4**) of $sMoO_x$ heat-treated at temperatures above 150°C contains growing signals of Mo^{5+} and even Mo^{4+}, as the oxygen leaves the oxide matrix. This is accompanied by a drop in *WF* to 5.1 eV (for 200°C) due to decrease of metal cation electronegativity [184] and an increase of electrical conductivity of $sMoO_x$ by more than an order of magnitude from $1.9 \cdot 10^{-6}$ to $4.0 \cdot 10^{-5}$ S/cm.

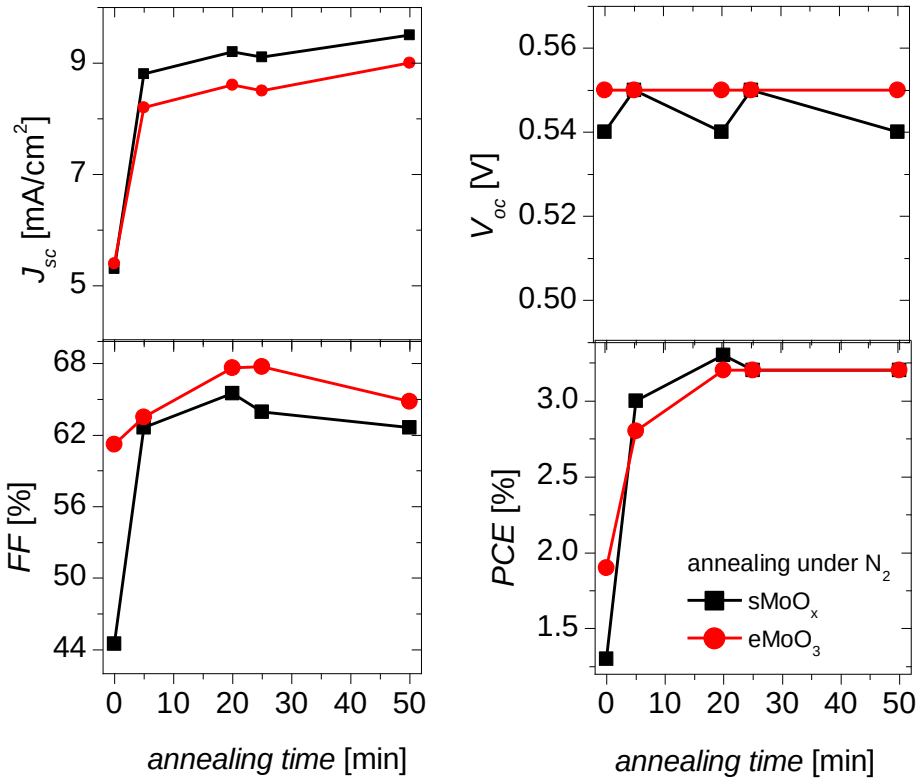

Figure 3.3.8. Evolution of OSC characteristics during the annealing (previous to deposition of the photo-active organics) of $sMoO_x$ and $eMoO_3$ layers in N_2 at 150°C.

As demonstrated in **Figure 3.3.9**, the thermally driven rise of the density of metal cations in the oxide bulk results in the pronounced reduction of the effective bandgap (from 2.76 eV for neat films to 2.4 eV for 200°C-treated films) and increased optical sub-bandgap absorption by electrons that partially fill the Mo d-orbitals within the oxide gap as the oxygen desorbs [85]. Essentially the same behavior is found for $eMoO_3$ films in this work (not shown here) and also for different TMOs in other groups [171, 185, 186]. Though the *WF* of $sMoO_x$ may stay reasonable for efficient hole extraction, an increased density of gap states may facilitate the parasitic recombination of charge carriers at the interface of the oxide and BHJ deteriorating the performance of devices on N_2-annealed $sMoO_x$ films observed in **Figure 3.3.7** for temperatures beyond 150°C.

Interestingly, devices on $sMoO_x$, annealed in ambient air (**Figure 3.3.7**), demonstrate a continuous rise of characteristics even for 300°C, as the thermally induced oxygen deficiency is balanced by re-adsorption of excessive atmospheric oxygen.

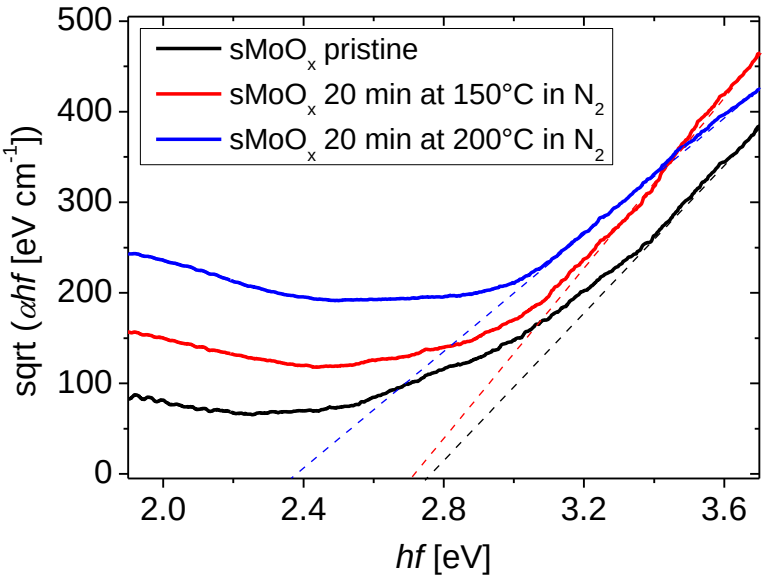

Figure 3.3.9. Tauc's plot for pristine and heat-treated in N_2 $sMoO_x$ films derived from optical transmission measurements. The crossing of dashed lines with the abscissa indicates the value of the $sMoO_x$ bandgap for individual annealing parameters.

Being aware of proper processing treatment, the optimization of $sMoO_x$ film thickness in range of 10 to 52 nm for the best device performance is carried out (**Figure 3.3.10, Table 3.3.2**). The optimum film thickness in a device in this series of experiments amounts to 22 nm.

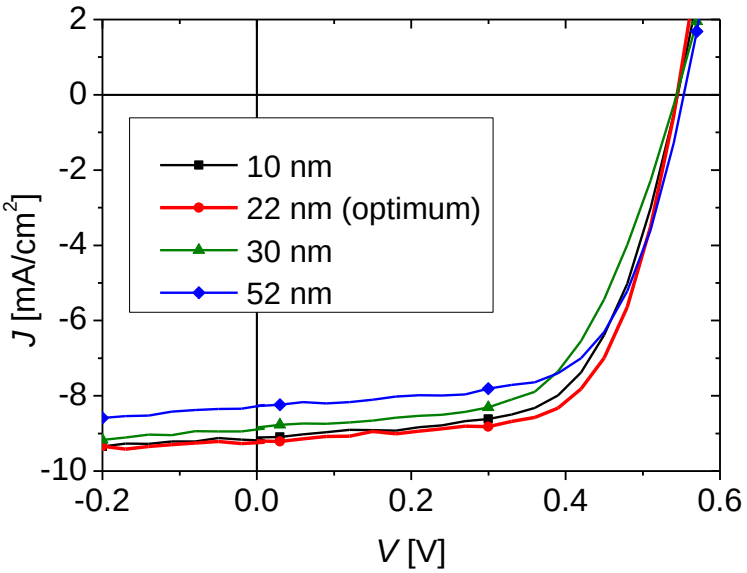

Figure 3.3.10. *JV*-characteristics of OSCs for varied $sMoO_x$ film thickness.

Table 3.3.2. Characteristics of OSCs comprising the $sMoO_x$ layer of various thickness.

$sMoO_x$ film thickness [nm]	*PCE* [%]	V_{oc} [V]	J_{sc} [mA/cm^2]	*FF* [%]
10	3.1	0.55	9.1	63
22	3.3	0.54	9.2	66
30	2.9	0.54	8.9	59
52	2.9	0.55	8.3	64

For layers thicker 22 nm, a slight drop in J_{sc} is evidenced. Similar as for sVO_x devices, this drop is not associated with ohmic losses in the bulk of the oxide (*FF* remains stable), but again is related to parasitic absorption in the metal oxide. Integrating the transmission spectrum in the relevant range from 350 to 650 nm (absorption band of P3HT:PC_{60}BM blend) counts for about 7% absorption in 52 nm bulk of MoO_x. For comparison,

having a substantially lower bandgap sVO_x film with 52 nm thickness would absorb twice as much light in the same spectral region.

3.4. Environmental device stability

As mentioned above, replacing the PEDOT:PSS in OSCs to provide environmental and (even if encapsulated) intrinsic stability of the hetero-junction and the interfaces in the device is one of the goals to achieve by utilizing the solution-processed metal oxides instead of PEDOT:PSS. The evolution of device efficiency using PEDOT:PSS and high *WF* metal oxides introduced in this work upon storage in darkness is depicted in **Figure 3.4.1**.

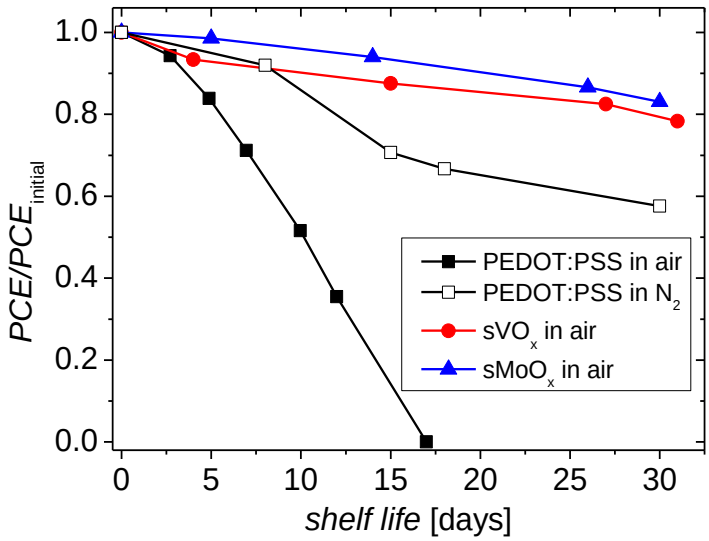

Figure 3.4.1. Plot of non-encapsulated PEDOT:PSS and sol-gel metal oxide device efficiency in dependency on storage time in the dark illustrating the device degradation.

During the first 17 days in ambient atmosphere (*rH* was varied between 44-62% in a natural way during the storage) the PEDOT:PSS device deteriorated fast and completely lost its functionality. Even in absence of moisture and oxygen in a controlled glove box environment filled with chemically inert N_2 the PEDOT:PSS devices exhibit pronounced degradation most probably caused by the acidic PSS component.[110]

Opposed to that, devices based on solution-processed TMOs after 30 days in air still maintain about 80% of the initial PCE.

3.5. Inverted device with sol-gel VO_x anodic interlayer

For reasons discussed above (**Chapter 2.5**), the inverted device sequence might be preferable. In the inverted stack the anode interlayer has to be deposited on top of the photo-active organic blend. Here, solvents orthogonal to those used for the organics have to be used and processing conditions have to be chosen in order to avoid eventual damage to the sensitive organics. As discussed in **Chapter 3.2** the unique high *WF* of the sVO_x is accessible without any post-depositional treatment. Opposed to that, using alternative sol-gel high *WF* metal oxides (e.g. MoO_x, **Chapter 3.3**) requires either an annealing step that could distort the morphology of the D/A blend (and with this exciton dissociation efficiency and charge transport), or oxygen plasma treatment of the surface, which is impossible as the metal oxide/organic interface is buried. Even if the interface could be accessed by plasma, the organic layer would be exposed to reactive oxygen species, most probably resulting of severe damage.

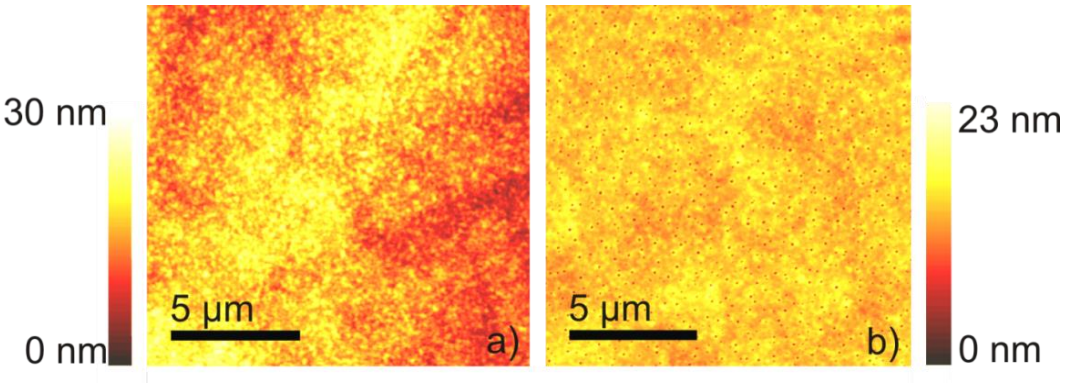

Figure 3.5.1. AFM non-contact topography images of P3HT:$PC_{60}BM$ film (a) and P3HT:$PC_{60}BM$ film coated with sVO_x (b).

For the sol-gel deposition of VO_x on top of the organic photo-active layer, vanadium(V) oxitriisopropoxide solution in isopropanol (see **Chapter 3.2**)

is used. The precursor concentration in IPA is further reduced to vol. 1:150 to avoid eventual unwanted chemical reaction with organics at the interface. **Figure 3.5.1** contains the AFM topography images of the annealed P3HT:$PC_{60}BM$ blend and the same blend coated with sVO_x, where the sVO_x coating is easily identified via nano-scopic voids (compare **Chapter 3.2**), which typically accompany the sol-gel films.

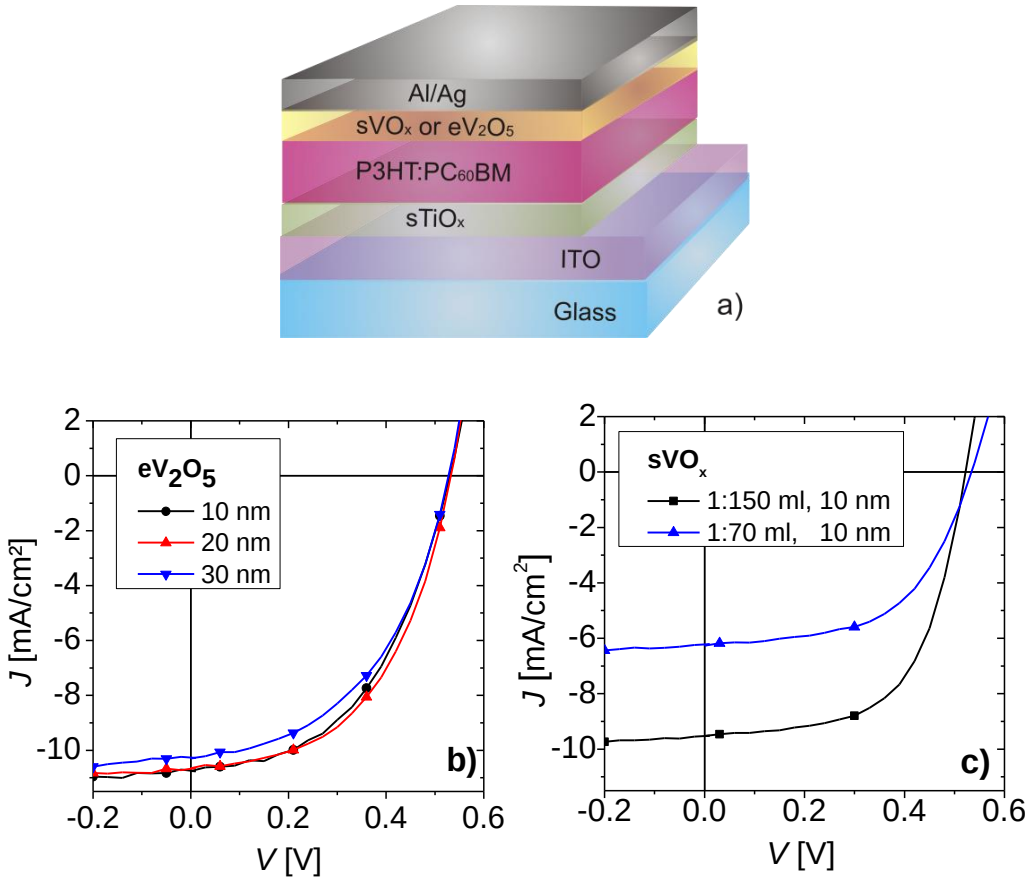

Figure 3.5.2. Layer sequence of the inverted devices studied in this work (a); *JV* characteristics of inverted devices comprising eV_2O_5 with varied film thickness (b); *JV* characteristics of inverted devices comprising sVO_x of optimized 10 nm thickness processed from two different concentrations of precursor solution: vol. 1:150 and 1:70 (c).

It is illustrated that the wettability of organics by the precursor solution is not an issue and despite the very low precursor concentration a complete organic surface coverage is afforded. The coating of sVO_x also smoothens

the annealed blend to 1.3 nm rms (vs. 4 nm rms previous to VO_x deposition).

The inverted OSCs studied in this work have the following layer sequence: glass/ITO/$sTiO_x$/P3HT:$PC_{60}BM$/(sVO_x or eV_2O_5)/Al/Ag. The stack is depicted in **Figure 3.5.2-a.** An additional aluminum thin film was deposited as adhesion promoter for the silver electrode.

As a reference, inverted devices with thermally evaporated eV_2O_5 in thickness range 10 to 30 nm are first analyzed (**Figure 3.5.2.-b** and **Table 3.5.1**). Typical (for P3HT:$PC_{60}BM$) V_{oc} values and moderate *FF*s are conserved. Remarkably, the dependency of J_{sc} on the oxide thickness is reduced dramatically in the inverted stack compared to the regular layout. For the inverted cell structure, the optical losses associated with the low bandgap of vanadium oxide are much less limiting the photo-current, as the light first passes through the photo-active organics and is absorbed there.

Table 3.5.1. Characteristics of inverted OSCs comprising thermally evaporated eV_2O_5.

	PCE [%]	V_{oc} [V]	J_{sc} [mA/cm²]	*FF* [%]
eV_2O_5 – 10 nm	2.8	0.53	10.8	49
eV_2O_5 – 20 nm	2.9	0.53	10.7	51
eV_2O_5 – 30 nm	2.6	0.53	10.3	48

Table 3.5.2. Characteristics of inverted OSCs comprising sol-gel sVO_x.

	PCE [%]	V_{oc} [V]	J_{sc} [mA/cm²]	*FF* [%]
sVO_x – 10 nm from vol. 1:150	3.0	0.52	9.5	60
sVO_x – 10 nm from vol. 1:70	1.8	0.53	6.2	55

Finally, devices comprising 10 nm of sVO_x were fabricated using the optimized precursor concentration (**Figure 3.5.2.-c** and **Table 3.5.2**). A comparable device performance is estimated for both sVO_x and eV_2O_5.

Surprisingly, a substantially deteriorated J_{sc} (**Figure 3.5.2.-c** and **Table 3.5.2**) is obtained for devices with sVO_x processed to the same film thickness of 10 nm from higher concentrated precursor solution (vol. 1:70). Note, it is rather unlikely that the device deterioration can be associated with morphological change in the BHJ or at its interface to the sVO_x layer spincoated from higher concentrated solution. The AFM measurement (not shown here) demonstrates no difference in surface topography and roughness for P3HT samples covered with sVO_x from vol. 1:150 and 1:70 solutions. Obviously, precursor species or the products of their hydrolysis somehow interact with the photo-active layer at the interface or even in the organic bulk.

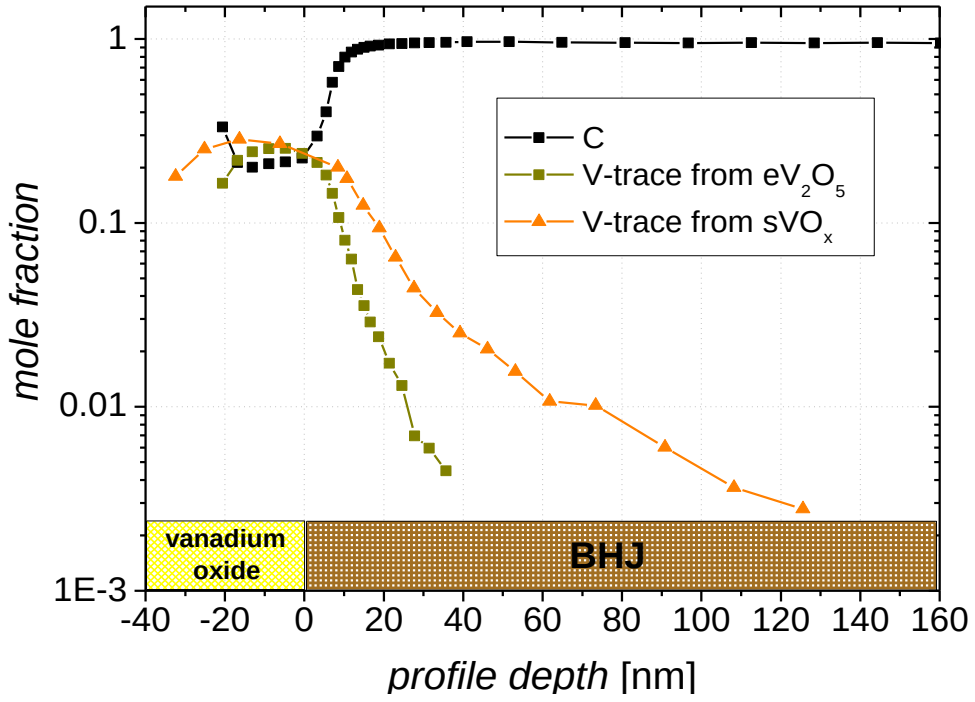

Figure 3.5.3. XPS depth profiles of V $2p_{3/2}$ signal for sVO_x film spin-casted on top and for eV_2O_5 film thermally evaporated on top of P3HT:PC_{60}BM layer. The carbon signal visualizes the interface between vanadium oxide and the organics.

To study the eventual penetration of vanadium(V)oxitriisopropoxide to the BHJ probable in case of liquid processing, depth profiling of

P3HT:P_{60}CBM blend samples coated with sVO_x is performed via low-energy Ar sputtering. For selected sputter depths the elemental (XPS) analysis of the resulting surface is carried out (**Figure 3.5.3**). For reference, organic samples covered with thermally evaporated vanadium oxide, for which an abrupt interface is expected, were analyzed.

The interface between the oxide and the BHJ is indicated by a dramatic rise of carbon signal. Counting from this interface, traces for V atoms stemming from the evaporated oxide are found to decay by an order of magnitude within the first 20 nm of the blend. Their very presence in the organic layer is explained by the mechanical interaction of oxide matrix with heavy Ar species that push the front of matter before them during the sputtering. Note, the surface roughness of the annealed blend counts for only 4 nm rms and, therefore, cannot affect the profiling results. In contrast, V atoms of the sol-gel processed oxide are found to penetrate the organics to a depth of more than 100 nm.

It should be mentioned beforehand that the vanadium-organic compound is not expected to oxidize the polymer or break the conjugation of the polymer backbone. Even though V^{5+} is a Lewis acid and can be used as a catalyst for oxidation reactions, it typically does not oxidize by itself. In addition, the activity of such catalysts is hampered in presence of alcohol (IPA is used in this work) or other polar solvents. [187]

A nuclear magnetic resonance (NMR) measurement carried out on P3HT dissolved in 1,2-dichlorobenzene (**Figure 3.5.4**) revealed no significant change in the molecular structure after addition of concentrated vanadium(V) oxitriisopropoxide to it. A shift in the response frequency and a somewhat lower signal intensity after the addition of the precursor is associated with an additional screening during the measurement introduced by the additional substance. Therefore, it is unlikely that the efficiency of OSCs drops due to chemical damage of the polymer introduced by the metal-organic compound.

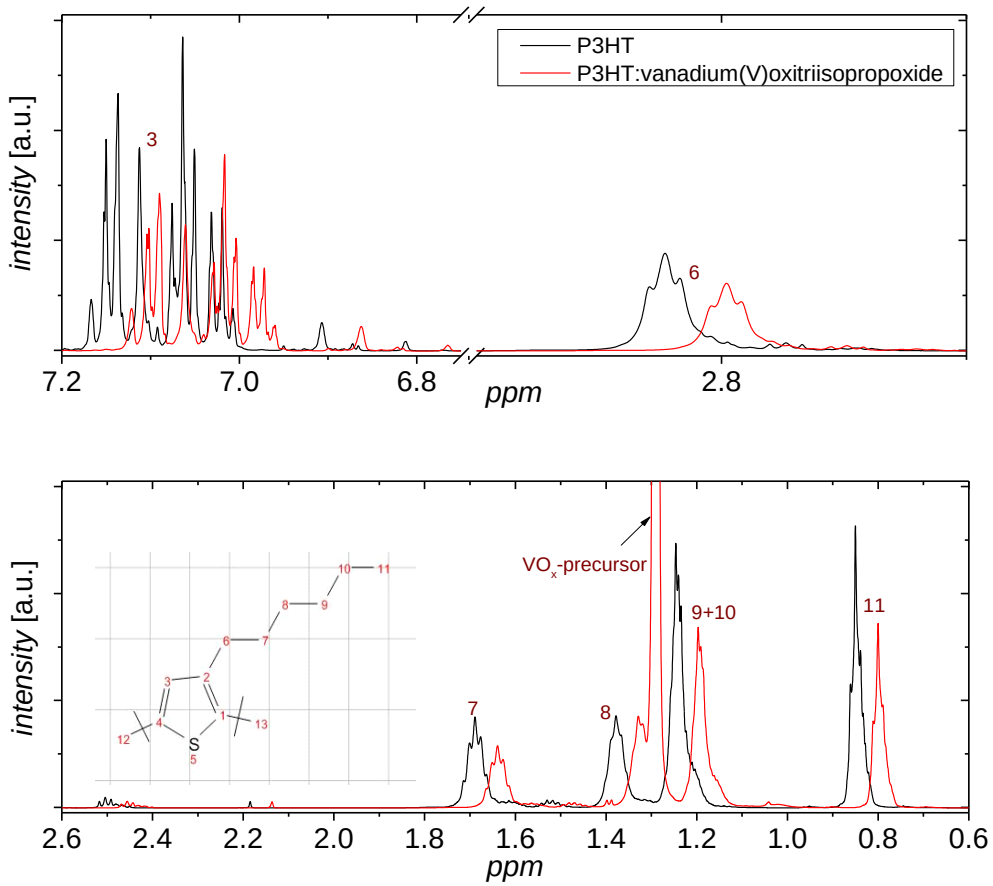

Figure 3.5.4. NMR-spectrum of P3HT and P3HT:vanadium(V) oxitriisopropoxide solved in 1,2-dichlorobenzene.

A result of the photoluminescence (PL) measurement carried out in chlorbenzene solution of pure P3HT and P3HT:precursor blend is depicted in **Figure 3.5.5**. It is seen that only a minor decrease of the PL signal is found upon mixing the P3HT with the precursor compared to pure P3HT sample.

Further, as a small portion of water is added to the P3HT:precursor blend, a considerable drop in PL signal intensity is observed (**Figure 3.5.5**). The agglomeration of the polymer on the formed metal oxide particles and precipitation leads to broadening of the peak. Note, the PL spectrum remains vastly unchanged, if water is added to the pure P3HT solution without the metal-organic compound. It is proposed that the vanadium

oxide, formed upon water addition, leads to quenching of the PL of P3HT e.g. by doping it (see also **Chapter 2.4**). It is known that in p-doped organic materials the PL quantum efficiency is strongly reduced.[188, 189]

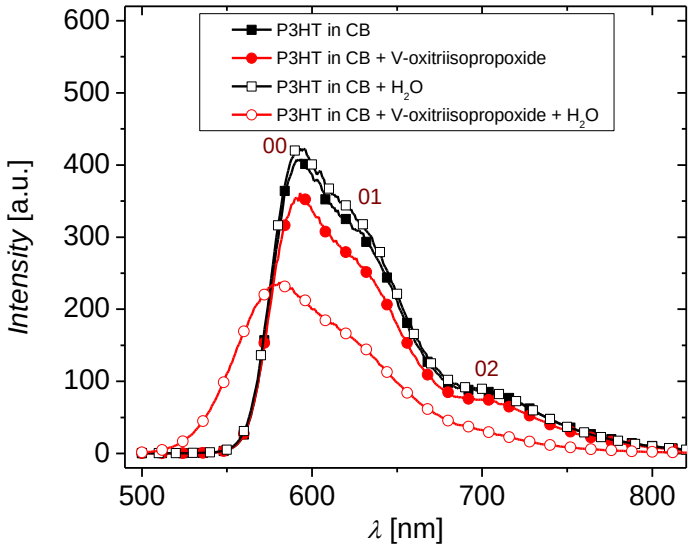

Figure 3.5.5. PL-spectra of neat P3HT solved in chlorbenzene, P3HT solved in chlorbenzene and blended with vanadium(V) oxitriisopropoxide with and without water. Excitation is provided by 470 nm laser to avoid the background PL from the solvent and vanadium(V) oxitriisopropoxide.

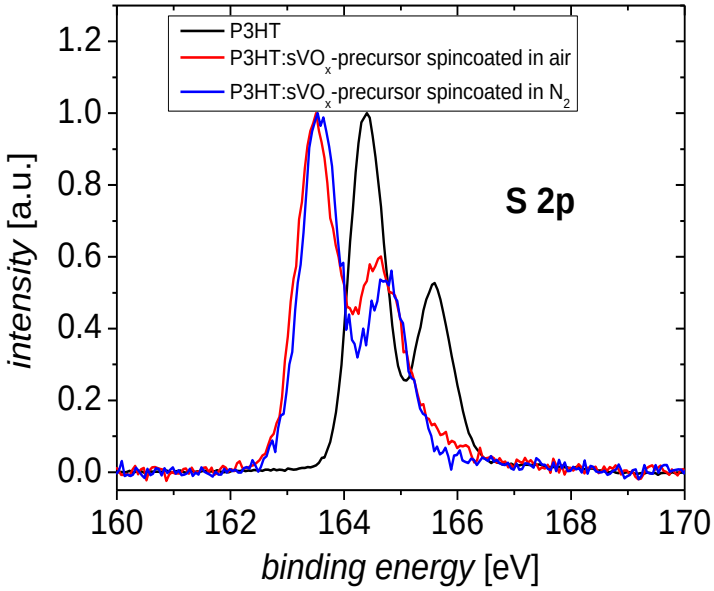

Figure 3.5.6. Normalized XPS spectra of films of P3HT, P3HT blended with vanadium(V) oxitriisopropoxide spincoated in ambient air and in N_2.

The assumption of p-doping is supported by the results of the XPS study on the solid thin films spincoated from the blended P3HT:precursor solutions (**Figure 3.5.6**). The XPS spectra (S 2p peak) of the films comprised of pure P3HT or P3HT:vanadium(V) oxitriisopropoxide (annealed after spincoating at 80°C for solvent evaporation) reveal a shift of the S 2p peak to smaller binding energies upon addition of the precursor. This is indicative of a movement of the HOMO level closer to E_F. Also, new shoulders arise in regions of 164.2 to 164.8 eV and between 165.5 and 166.8 eV that correlate with the formation of cationic polymer species. Simultaneously, the reduction of V^{5+} to V^{4+} (not shown here) occurs indicating an electron transfer to the V atoms within the film spincoated in air. This hints for the effective p-doping of P3HT. The shoulders mentioned above are more pronounced for the samples spincoated in air (than for films prepared in N_2), which are expected to contain more metal oxide, as a result of hydrolysis and condensation of the precursor. Thus, the dominant role in doping the polymer is attributed to the metal oxide rather than to the precursor. This is strongly supported by the fact that the film processed in N_2 exhibits only a weak XPS signal due to vanadium (not shown here). In absence of moisture, the vanadium(V) oxitriisopropoxide does not form a solid metal oxide and is not chemically bound to the polymer matrix. Thus, it may evaporate from the film after the deposition without any chemical interaction with the polymer. The small signs of p-doping also for inert-processed blended P3HT:vanadium(V) oxitriisopropoxide films may originate from a partial oxide formation due to residual moisture in the solvent used in this experiment.

The doping effect is also observed indirectly for the hole-only devices (**Figure 3.5.7**). For these, P3HT with and without sVO_x-precursor is directly spincoated in air and, for comparison, in N_2 on the glass/ITO substrates. A low *WF* aluminum electrode is deposited on top. Without using proper high *WF* interlayers, the effect of doping on the *JV*-

characteristics of such devices is expected to be more obvious. As a result, the blended films spincoated in air exhibit the injection current density (at 2.5 V) roughly 1 order of magnitude higher compared to blended films, spincoated in N_2, again indicating the major role of the metal oxide (and not of its precursor) in the polymer doping. Strikingly, the *J* for P3HT:precursor blends spincoated in air is enhanced roughly by 5 orders of magnitude compared to the neat P3HT at 2.5 V.

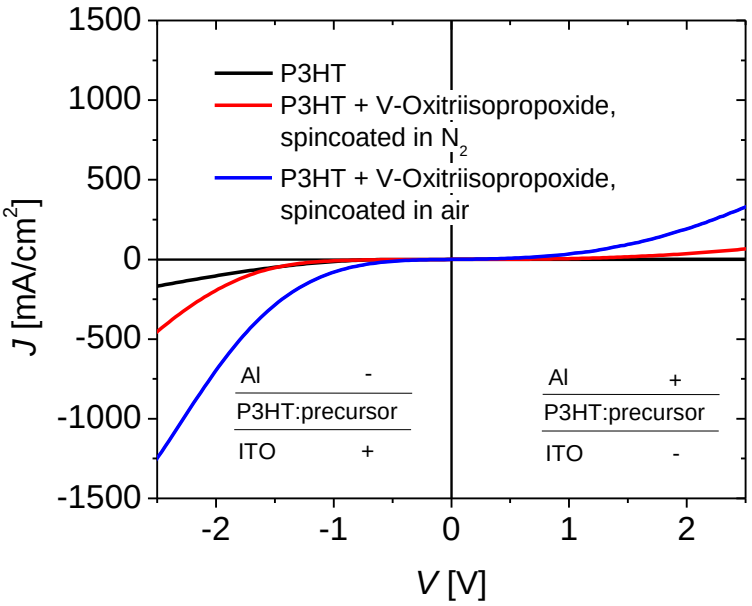

Figure 3.5.7. The *JV*-curves of the hole-only devices comprising P3HT, P3HT blended with vanadium(V) oxitriisopropoxide spincoated in ambient air and in N_2.

Even though doping of the organics at the anode interface of an OSC may have a positive effect on the device performance enhancing the hole extraction efficiency (**Chapter 2.4, 3.2** and **3.3**), the deep penetration of precursor into the bulk of the photo-active layer with subsequent formation of vanadium oxide and p-type doping of the polymer can explain the deterioration of the device performance found above (**Figure 3.5.2.-c** and **Table 3.5.2**). For instance, the theoretical modelling of P3HT-based OSCs clearly demonstrated that at the polymer doping concentration of 10^{16} cm^{-3} and above the built-in field within the BHJ becomes partially screened and

only a portion of the photo-generated charges within the areas, where the electric field is present, contributes to the photo-current.[190] The remaining photo-generated charges recombine. In this modelling study[190] it was assumed that the formation of cation radicals does not lead to exciton quenching. Interestingly, the drop in the device efficiency was mainly due to severe reduction of the J_{sc} and rather moderate reduction of the *FF*. Exactly this is observed empirically in this work (**Figure 3.5.2.-c** and **Table 3.5.2**) for inverted OSCs with sVO_x anode deposited from higher concentrated solution.

It is known that the metal-organic precursor molecules tend to form larger sized oligomers during the moisture-driven cross-linking.[191] This might be used to reduce the vanadium(V) oxitriisopropoxide penetration rate and depth into the BHJ during the deposition and reduce the deteriorating effect of the excessive polymer doping in the volume of the photo-active blend. To evaluate this, inverted OSCs comprising sVO_x from two solutions, stirred in air (aged for 48 h) and in N_2, are prepared. Note, in this experiment a more concentrated solution of vol. 1:70 (compared to best performing vol. 1:150) is deliberately chosen in order to intensify the precursor-related effects. The spincoating of the sVO_x-solution is done at 5 times slower velocity than that for an optimized device thickness (10 nm) in order to deliberately allow the precursor to penetrate into the photo-active layer. The resulting sVO_x film is estimated to be roughly 30 nm thick for pre-hydrolyzed solutions. The corresponding device characteristics are summarized in the **Table 3.5.3**.

The OSCs comprising the sVO_x interlayer from a solution stirred under inert conditions, which wetted the BHJ for 1 s previous to spincoating, exhibit the low J_{sc} of 7.6 mA/cm^2 and *FF* of 40%. The low *FF* results most probably from the not complete coverage of the BHJ by the sVO_x in case of not pre-hydrolyzed solution. The *FF* improves dramatically to 53%, if the wetting time is increased to 4 s. Within this time, an efficient cross-linking

of the thin liquid film obviously takes place resulting in complete substrate coverage. Still, the J_{sc} remains deteriorated at 7.4 mA/cm^2.

Table 3.5.3. Characteristics of inverted OSCs comprising the sVO_x anode interlayer deposited from precursor solution stirred in ambient air (65% *rH*) for 48 h and in N_2. In addition, the effect of a delay between wetting and spincoating for both solutions is demonstrated.

ITO/TiO_x/P3HT:$PC_{60}BM$/sVO_x/Al/Ag	*PCE* [%]	V_{oc} [V]	J_{sc} [mA/cm^2]	*FF* [%]
stirring in N_2, wetting 1 s	1.6	0.51	7.6	40
stirring in N_2, wetting 4 s	2.0	0.51	7.4	53
stirring in air 48 h, wetting 1 s	2.3	0.51	9.0	51
stirring in air 48 h, wetting 4 s	2.2	0.51	8.5	50

The J_{sc} is improved by roughly 20%, if the precursor solution aged in ambient air remaining on the BHJ for 1 s is used. A longer wetting (4 s previous to spincoating) again lowers the J_{sc} to some extent. Nevertheless, it remains dramatically higher in comparison to the J_{sc} observed for not pre-hydrolyzed solutions.

Importantly, this difference in the device performance cannot be explained by different interface energetics, as the *WF* estimated for sVO_x spincoated from aged and not aged solutions remains the same. Thus, a strong indication is found that the doping of the polymer is less spread into the volume of the BHJ and more confined to the anode interface, if pre-hydrolyzed metal-organic precursor solution combined with a shorter wetting time previous to spincoating is used for the oxide liquid-deposition.

3.6. Summary

This chapter deals with sol-gel processed high *WF* amorphous metal oxides (sVO_x and $sMoO_x$). Environmentally friendly alcoholic solvents are used for the sol-formulation. Both metal oxides are formed at *RT* and ambient air via hydrolysis of the precursor after deposition and exhibit extreme smoothness and homogeneous surface coverage. Only a small

portion of organic residue in the films non-affecting the electronics and device performance is proposed. The electronic structure of in air processed sol-gel oxides is identical to the structure of air-exposed thermally evaporated counterparts.

The high *WF*, required for efficient hole extraction, is obtained for VO_x films already at *RT* without any post-processing. This makes it especially attractive for inverted OSCs, where the anodic interlayer is processed on top of the temperature sensitive organics. At the vanadium(V) oxitriisopropoxide optimized concentration of vol. 1:150 in IPA, an efficient OSC is realized outperforming the devices with thermally evaporated oxide. If a higher concentrated solution (vol. 1:70) of the metal-organic precursor is used for metal oxide deposition on top of the organics, the massive penetration of the precursor species into the volume of the photo-active layer must be taken into account. Though the metal-organic compound is not expected to damage the polymer, the excessive doping through the product of its hydrolysis and condensation, the metal oxide, is observed via several direct and indirect analysis techniques and device measurements. If a long wetting time of the photo-active layer by the precursor solution must be tolerated due to the specifics of a solution-based deposition technique, a less concentrated precursor solution pre-hydrolyzed upon stirring in humid air must be used to limit the penetration due to growing cluster size in the sol-gel and minimize the effects leading to performance deterioration.

Though the optical losses in the bulk of VO_x due to its relatively low bandgap may not play a paramount role for inverted devices, for OSCs with regular architecture sVO_x films less than 20 nm thickness are preferable to avoid parasitic absorption and current drop.

From this point of view, the more transparent MoO_x serves as an attractive alternative. The sol-gel processing of MoO_x at *RT* results already in stoichiometric MoO_3. Unfortunately, due to the hydrophilic nature, the *WF* of as-deposited MoO_x is affected by the adsorbates and is rather low for

OSC applications. It is demonstrated that adsorbate removal can occur via heat treatment at 130-150°C in nitrogen. But it is not necessarily the only option. Alternative *RT* chemical routes or selective (without heat transfer to the substrate) microwave annealing for adsorbate removal can be considered. For instance, in this work the oxygen plasma treatment was shown to recover the *WF* of $sMoO_x$ to values above 5.3 eV.

Introducing these metal oxides allows for efficiency comparable and higher than that of devices on PEDOT:PSS. Maintaining the advantage of liquid-processing, the environmental stability of OSCs based on these metal oxides is dramatically improved.

4. Ultra-thin functional films of conjugated polyelectrolytes

In this chapter an enhancement of the electron extraction at the cathode interface of OSCs via solution-processed ultra-thin interlayer of conjugated polyelectrolyte (CPE) is addressed. Specifically for inverted OSCs, the ITO exhibiting a *WF* of typically 4.7-4.8 eV is not suitable for electron extraction. In addition, being highly doped, a metal-like ITO provides intense recombination sites for photo-generated electrons at the interface to organics. For these reasons, the surface of ITO is typically modified via low *WF* metal-oxides (TiO_x [192, 193], ZnO [194-197], Al:ZnO [198], SnO_x [199]). Applying the liquid-processing for metal oxides often requires high temperatures (200-260°C) for precursor decomposition and/or for dopant activation. Even using sol-gel *RT* derived oxides, like low *WF* titanium- or tin oxide, often requires a stricter parameter control and allows for a smaller degree of freedom associated with (moisture reactive) ink stability previous to and during the deposition.

A number of recent works in other groups demonstrated the alternative route to modify the cathode *WF* by using the organic interlayers, like polyethylene oxide [200], non-conjugated polyethyleneimine [201, 202] or polyvinylpyrrolidone [203]. In regular OPV device structure, the insertion of such layers between the organics and metal top electrode allowed for use of environmentally stable high *WF* metals (Au, Ag instead of Ca, Al, LiF) for electron extraction.[202] A substantial increase in OSCs performance was demonstrated using thin interlayers (<10 nm) of conjugated poly(3,3'-([(9'9'-dioctyl-9H,9'H-[2,2'biflourene]-9,9-dyil)bis(1,4-phenylene)]-bis(oxy)) bis(N,N-dimethylpropan-1-amine))[204] and poly[(9,9-bis(3'-(N,N-dimethyl-amino)propyl)-2,7-flourene)-alt-2,7-(9,9-dioctylfluorene)] [205, 206] also.

The CPEs are often used as an additional means to further enhance the charge extraction efficiency provided by low *WF* metal oxides (TiO_x [207], ZnO [208]) on the transparent electrode. Therefore, in this work, the direct modification of ITO *WF* via N-methylimidazoliniumalkyl-substituted Poly(3-[6-bromohexyl]thiophene) (P3ImHT) is studied on instance of inverted

OSCs. Choosing P3ImHT among the variety of CPEs is governed by its high chemical and thermal stability.[209]

4.1. Film processing and device application

The molecular structure of P3ImHT is depicted in **Figure 4.1.1**. The CPE materials are typically processed from polar solvents like water or alcohol, which makes the processing environmentally friendly and with less safety restrictions. In this work, methanol is primarily used to solve the polymer. To prevent the complete rapid solvent evaporation and obtain homogenous substrate coverage by ultra-thin CPE, ethanol with lower vapor pressure is added to the solution previous to spincoating. To dry the layer from solvent residue, a subsequent 5 min heat-treatment at 100°C is applied.

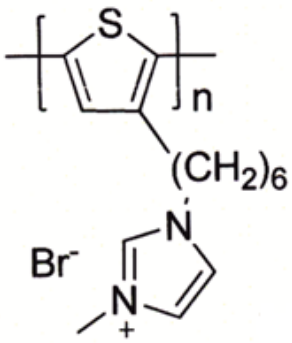

Figure 4.1.1. Molecular structure of conjugated P3ImHT.

Depositing CPE from extremely diluted solutions results in film thicknesses (far) below 10 nm. A low surface roughness of 0.3 nm rms and homogeneous coverage of the substrate is observed via AFM topography and phase image (**Figure 4.1.2**) respectively.

Modifying the surface of ITO by P3ImHT results in a large shift of the *WF* from 4.8 to 4.4 eV. The shift is not observed upon wetting the ITO with the solvent only. Further, the *WF* shift remains stable after rinsing the CPE-coated ITO with typical aromatic solvents, like dichlorobenzene, used for blending the moieties of the photo-active organics. This is crucial for

inverted OSCs, as the organics is deposited on top of the cathode interlayer.

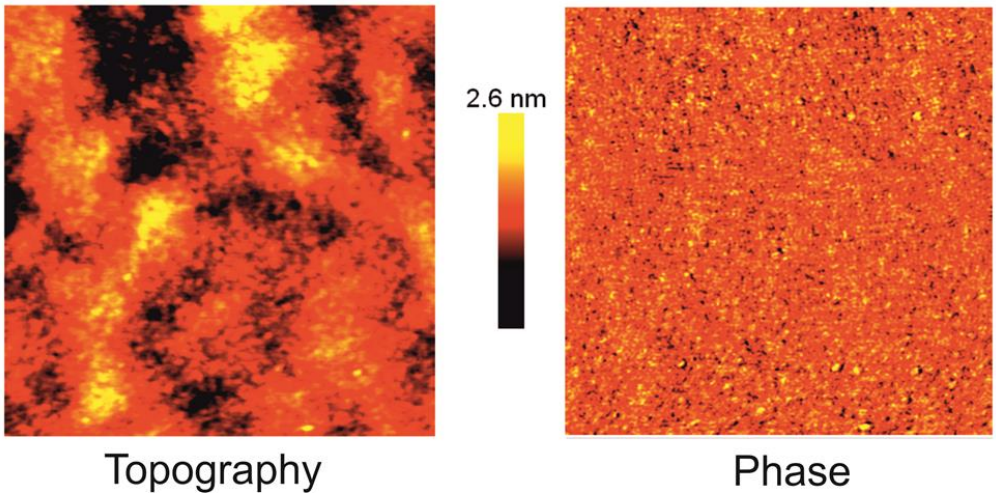

Figure 4.1.2. AFM topography (left) and phase (right) 1.5x1.5 μm^2 image of CPE film deposited on a smooth crystalline Si substrate.

The impact of the CPE interlayer is first demonstrated on inverted OSCs based on more efficient (compared to P3HT:$PC_{60}BM$) PCDTBT:$PC_{70}BM$ active blend with the stack structure according to **Figure 4.1.3.-a**. The corresponding curves are found in **Figure 4.1.3.-b**.

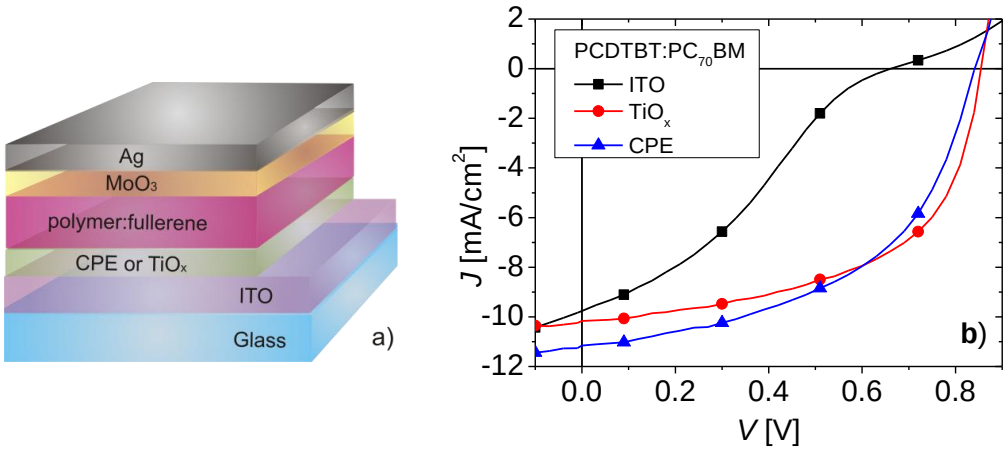

Figure 4.1.3. A stack of studied inverted OPV devices (a); *JV*-curves of inverted OSCs comprising different electron extraction layers and PCDTBT:$PC_{70}BM$ active blend (b).

As expected, the non-modified ITO results in a hampered device *FF* (**Table 4.1.1**) and an s-shaped *JV*-characteristics due to inefficient electron extraction and parasitic recombination at the interface. Meanwhile, devices with TiO_x or CPE demonstrate improvement of all characteristics simultaneously and exhibit comparably high *PCE*s of 4.9 and 4.8% respectively.

Table 4.1.1. Full-sun (AM1.5G) characteristics of inverted OSCs based on PCDTBT:$PC_{70}BM$ and P3HT:$PC_{60}BM$ active blends, using the ITO or $sTiO_x$ or P3ImHT for electron extraction.

PCDTBT:$PC_{70}BM$	*PCE* [%]	V_{oc} [V]	J_{sc} [mA/cm^2]	*FF* [%]
TiO_x	4.9	0.85	10.2	56
CPE	4.8	0.84	11.2	51
ITO only	2.0	0.66	9.8	31
P3HT:$PC_{60}BM$	*PCE* [%]	V_{oc} [V]	J_{sc} [mA/cm^2]	*FF* [%]
TiO_x	3.4	0.54	10.5	60
CPE	3.3	0.53	10.4	61
ITO only	0.9	0.35	8.5	29

However, in both cases (TiO_x and CPE) those high efficiencies are established only after a certain time required for so called light-soaking. Such behavior was observed previously for a number of low *WF* metal oxides, e.g. TiO_x [193, 210-212], ZnO [213, 214], SnO_x [199], independent on their deposition technique (sol-gel, ALD, NPs). Also for neat ITO the UV-light-soaking was found to take place, lowering its *WF* and thereby improving the device performance.[215, 216] However, even after significantly higher UV-illumination doses, the estimated device efficiency remains limited mainly due to a lower V_{oc}.

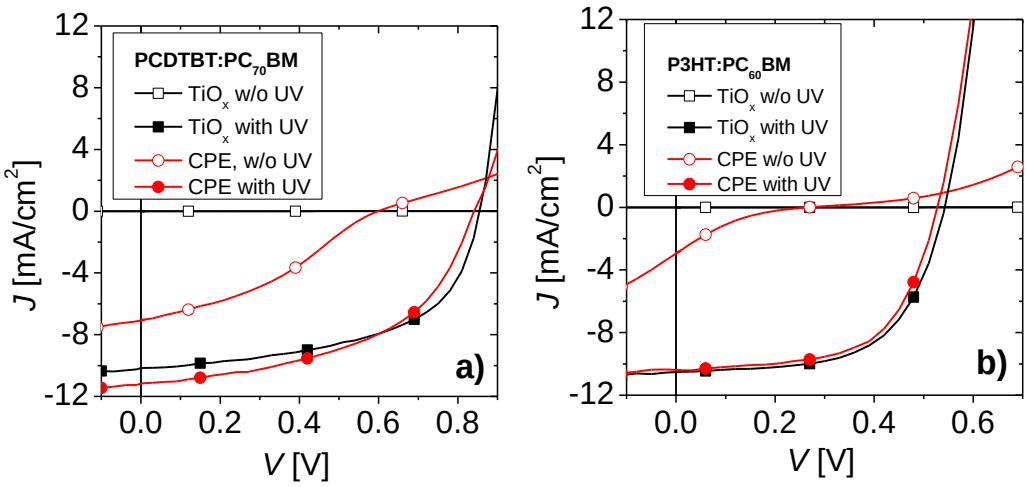

Figure 4.1.4. *JV*-curves of inverted OSCs based on TiO_x and CPE interlayers and different blends PCDTBT:PC_{70}BM (a) and P3HT:PC_{60}BM (b) at illumination under AM1.5G with and without UV part.

Regarding the ultra-thin polymer interlayer, the need of light-soaking can hardly be attributed to it. Nevertheless, inverted OSCs on ITO/CPE with different organic blends comprising PCDTBT:PC_{70}BM and P3HT:PC_{60}BM exhibit deteriorated *JV*-characteristics (s-shape), if the UV spectral part is cut-off by the GG435 (wavelength shorter than 435 nm are cut-off) optical filter (**Figure 4.1.4**). By removing the UV-filter, device characteristics improve continuously and saturate after several minutes of illumination at typical values (**Table 4.1.1**). A very similar behavior is witnessed for TiO_x-based devices.

4.2. Origin of light-soaking in ITO/CPE system

Considering the metal oxides, a number of (partially controversial) light-soaking mechanisms was proposed by several groups. Specifically, for high bandgap (3.1-3.3 eV) TiO_x trap-filling by UV-photo-generated charges and concomitant increase of electrical conductivity [212, 217], charge extraction barrier at ITO/TiO_x interface [210] and its removal via UV were suggested. For now, a plausible explanation of this phenomenon is

associated with the existence of the electron extraction barrier at the interface between the metal oxide and organics.[193]

According to this, the barrier is formed due to strongly electronegative oxygen species chemisorbed and negatively charged on the titania surface that causes the depletion at the interface. Under UV illumination, photo-generated holes interact with negatively charged oxygen and expel it from the surface recovering the low *WF* of the metal oxide, which is a prerequisite for efficient electron extraction. This effect was shown to be permanent for devices stored in oxygen deficient environment and reversible upon oxygen re-exposure.

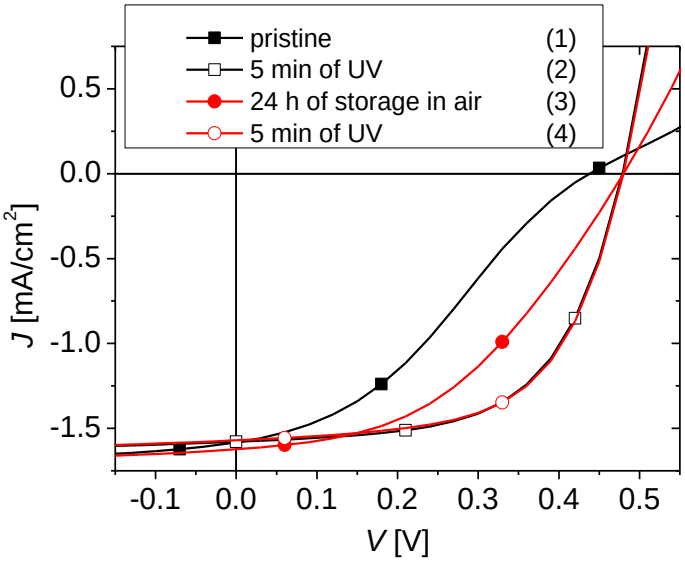

Figure 4.2.1. *JV*-curves of an inverted P3HT:PC_{60}BM OPV-device comprising a CPE interlayer upon illumination in nitrogen environment. For illumination, an UV-LED array (375 nm, 10 mW/cm^2) is used. The initial curve of the cell (1) with a low *FF* evolves to that of a proper functioning device upon UV-exposure (2), loses its performance during storage in air in dark (3) and recovers the performance upon repeated UV-exposure (4).

A very similar reversible behavior is found for the CPE devices (**Figure 4.2.1**) characterized in oxygen-poor nitrogen environment. The initially low *FF* of OSC comprising the CPE interlayer is improved to about 60% upon the continuous UV (375 nm) illumination. The subsequent 24 h air-exposure of the optimally functioning cell forces the *FF* to decrease to

44%. Whereas the repeated UV-illumination again recovers the high *FF* of 60%. Therefore, the improvement of the device *FF* upon UV-illumination cannot be explained by an irreversible change of the CPE due to e.g. photo-oxidation etc.

Remarkably, the improvement of the *FF* of OSCs on non-modified and CPE-modified ITO cathode upon AM1.5G (including UV part) essentially exhibits a similar temporal behavior (**Figure 4.2.2**). A rapid increase of the *FF* in first minutes for both ITO and ITO/CPE devices ends up in its saturation for longer light exposure. The deposition of CPE on ITO obviously grants an initial energetic off-set in form of an interfacial dipole, whereas light-induced change is apparently related to the ITO.

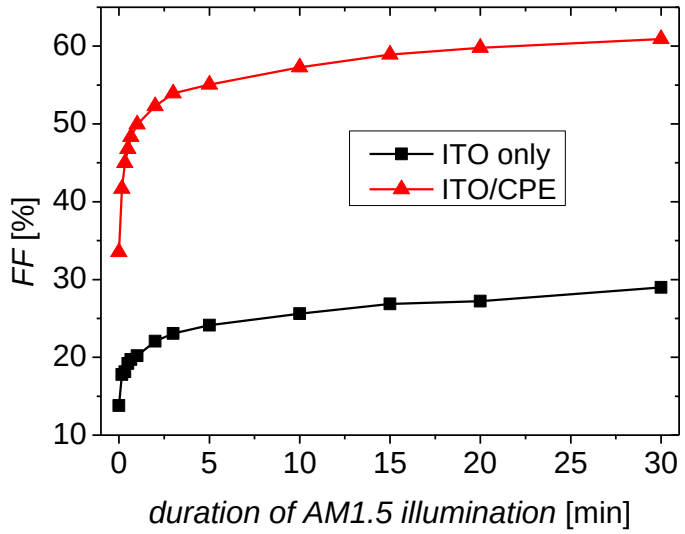

Figure 4.2.2. Time-resolved evolution of the *FF*s of inverted P3HT:$PC_{60}BM$ cells on ITO and ITO/CPE cathodes upon full-sun illumination.

To get the insight into the change of the energetics upon the UV illumination, KP analysis is performed (**Table 4.2.1**). As expected, the *WF* of TiO_x is lowered from 4.3 to 3.8 eV within minutes. Compared to that, the drop of the ITO *WF* takes typically much more time (several tens of minutes) and finally saturates at 4.3 eV. The *WF* of ITO/CPE saturates at 4.2 eV. Even though the difference to saturated ITO *WF* is only 0.1 eV, the

WF reduction down to at least 4.2 eV by CPE appears to be required for optimal electron extraction, as the s-shape of *JV*-characteristics vanishes (**Figure 4.1.4**).

Table 4.2.1. The *WF* of ITO modified by deposition of $sTiO_x$ and CPE estimated via KP before and after the UV illumination (375 nm, 10 mW/cm^2 for 60 min).

	WF [eV]	
	neat	after UV
ITO only	4.8	4.3
ITO/CPE	4.4	4.2
ITO/TiO_x	4.3	3.8

Interestingly, the relative drop of *WF* for ITO/CPE bilayer is significantly smaller than that for neat ITO (0.2 vs. 0.5 eV). In general, the interface dipole-induced shift in the *WF* caused by the deposition of ultra-thin CPE appears to be dependent on the initial *WF* of the substrate. The lower the initial *WF* of the substrate, the smaller the shift established by CPE (**Table 4.2.2**).

Though much work was devoted to reveal the mechanism of electronic change upon molecule adsorption, a universal explanation is still missing. Also for the phenomena discussed above, a systematic PES study would be required for deeper understanding of the nature of dipole formation specifically on metal oxide surfaces. This should be the subject of future analysis.

In general, the theoretical electrostatic modelling and spectroscopy data signal that the dipole moment for the substrate/organics system cannot be simply derived from the built-in molecular dipole moment of adsorbed molecules, but is formed in general as a superposition of that with an interface dipole created upon charge transfer (e.g. on bond formation) between substrate and molecular layer.[78, 79, 94, 202, 218-220]

Table 4.2.2. The *WF* modification of vastly amorphous metal oxides with different initial *WF* by CPE estimated via KP. For comparison the shift in the *WF* of crystalline Si-substrate with native oxide upon CPE deposition is shown.

	WF [eV]	Δ*WF* [eV]
VO_x	**5.4**	0.5
VO_x/CPE	4.9	
ITO	**4.8**	0.4
ITO/CPE	4.4	
ITO/UV-treated	**4.3**	0.1
ITO/CPE/UV-treated	4.2	
TiO_x	**4.3**	0.1
TiO_x/CPE	4.2	
TiO_x/UV-treated	**3.8**	0.1
TiO_x/CPE/UV-treated	3.7	
AZO	**4.2**	0.1
AZO/CPE	4.1	
AZO/UV-treated	**3.9**	0.0
AZO/CPE/UV-treated	3.9	

The contribution of **molecular dipole** of a single molecule to the modification of the substrate *WF* is restricted, if an assembly of neighboring adsorbed molecules is formed on the substrate surface. The effective dipole moment of all molecules depends on their geometry difference depending on the orientation of docking groups, coverage density, co-alignment of single molecular dipoles, twisting angle upon docking etc.[81, 218, 220, 221] For metal oxide substrates such geometric effects are even more crucial than for metallic layers.[218] In addition, for CPE films comprising not a single, but several (even well-ordered) monolayers, change of the effective dielectric constant and depolarization of the first on-substrate adsorbed molecular ensemble via next monolayers inevitably takes place.[222-227]

The **interface dipole** has even more complicated origin. In general, the electronic structure of the free-standing molecular layer differs dramatically from that of the adsorbed layer due to electrostatic renormalization on contact.[59, 78, 80, 81, 228, 229] Specifically, additional states

(strictly localized to the very bonding interface) appear in the gap of the molecular layer. Driven by the difference in chemical potentials between the substrate and the molecular assembly, the electron flow into/from these intra-gap states takes place to establish the energetic equilibrium.[80] The direction of the interface dipole is determined by the direction of the charge transfer.[230]

For this work, the electron transfer from the CPE into the metal oxide governed by the difference in the *WF* of both is assumed. This results in an interface dipole pointing away from the substrate surface (**Figure 4.2.3**) decreasing its *WF*, as observed experimentally.

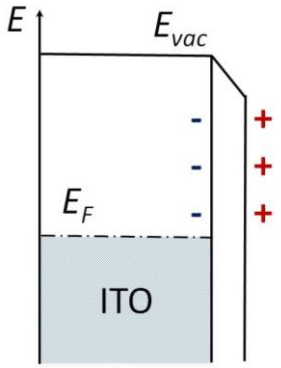

Figure 4.2.3. Schematic diagram of interface dipole formation on ITO upon adsorption of molecular layer.

According to density functional theory (DFT) calculations on SAM-modified metals done by other group [202], the higher the *WF* of the substrate, the more pronounced electron transfer from adsorbed molecules is expected. For instance, it was estimated experimentally that the interface dipole formed at the interface between high *WF* WO_3 and the organic layer was dependent on the initial *WF* of the oxide (varied by stoichiometry change) and was substantially more pronounced in case of higher *WF* oxide.[66] Moreover, the same study demonstrated a roughly 7 times smaller interface dipole on the low *WF* titania than on WO_3.

It is speculated here that the *WF* modification by the dipole moment of the molecule ensemble itself can be neglected due to stochastic CPE

molecular orientation on disordered surface of amorphous metal oxides. Thus, the shift of the *WF* in metal oxides modified via CPE originates from the interface dipole, which is of larger magnitude for high *WF* substrates and can be easily in-situ balanced via charge transfer for a bilayer of metal oxide/CPE, if the *WF* of the metal oxide is modified (e.g. by UV-exposure) as observed for ITO, TiO_x, ZnO and AZO. In other words, this assumption correlates with the CPE-induced *WF* shift of different magnitude dependent on initial substrate *WF* (**Table 4.2.2**) observed in this work.

4.3. Summary

In this chapter, a conjugated polyelectrolyte (P3ImHT) is successfully used to decrease the *WF* of an ITO electrode used as a cathode in efficient inverted OSCs. The CPE can be solution-processed from non-chlorinated solvents and forms an ultra-thin functional film on top of the ITO. The modification of the *WF* is achieved upon the formation of the dipole layer at the interface to the molecular film. Based on theoretical and spectroscopic studies carried out by various groups, an assumption is met that for metal oxides/CPE system the electron transfer from the contact-induced gap states of CPE into the oxide is a dominating factor of interface dipole formation and *WF* decrease. Thus, taking the difference in chemical potentials between the substrate and CPE as a driving force for charge transfer into account, the higher negative shift of the *WF* for metal oxides with initially high *WF* compared to low *WF* oxides is expected and observed.

Considering the device application of CPE, the reduction of the cathode *WF* obtained via CPE deposition results in efficient charge extraction from P3HT:PC_{60}BM blend and also for somewhat more efficient PCDTBT:PC_{70}BM system and device characteristics comparable with that of devices based on titania-modified ITO. The transient reversible characteristics of the OPV devices under full-sun illumination are shown to originate from the ITO underlying light-soaking process.

5. Composites of silver nano-wires and conductive metal oxides

Aside from photo-active and functional layers, R2R compatible low-temperature deposition of electrodes is desired for low-cost large-area OPV. Specifically for the see-through OPV, the electrodes must be in addition transparent.

As for now, ITO is almost exclusively used for device fabrication, for it exhibits typically low sheet resistance (R_{sh}) of 13-16 Ω/sq and high transparency in visible spectrum (95% compared to glass). But there are several issues associated with the use of indium. Aside from the limited abundance of indium, the deposition of ITO is a vacuum process. To gain the high transparency and low R_{sh} simultaneously, ITO-coatings require thermal post-treatment at 300-450°C.[11] If processed on flexible foils without excessive annealing, ITO still generates significant production costs [4, 231] and exhibits only moderate R_{sh} of 60 Ω/sq and average transmittance of 80%. Also, brittleness of ITO often does not fit the demand of R2R processing.

As the first alternative, *RT* processed evaporated thin metallic films sandwiched between two oxides were demonstrated to be highly transparent and conductive.[11, 232, 233] Still cost-intensive vacuum-processing remains a drawback. Further, solution-processed films of graphene [234] , graphene oxide [235] and carbon nanotubes [236-238] were studied. For these, a severe trade-off between transparency and conductivity was witnessed. Also, approaches based on metal nano-grids and stochastic meshes of metallic nano-wires were proposed for transparent conductive applications.[239]

5.1. Silver nano-wires: state of the art

Within such plethora, a lot of work was devoted to meshes of silver nano-wires (AgNWs) that exhibit outstanding stability, flexibility [240] and can be prepared with customized geometry [241]. The first reports of AgNW films already demonstrated reasonable average transparency (T_{av}) of 85% and

corresponding R_{sh} of 10 Ω/sq.[242] However, to avoid the agglomeration of NWs within the dispersion, polymeric dispersing agents had to be applied. In order to establish the conductive joints between the wires, samples were treated at 200°C in order to fuse the NWs on their crossings.

Typically, in a reasonable conductive transparent film NWs cover less than 20% of the substrate surface. The optical transmittance is then ensured via uncovered areas that each can be the size of several μm^2. In this areas charge transport is hampered due to absence of conductive material. This might be sufficient for transparent coatings used as e.g. resistive heaters for defrosting windows of outdoor vehicles. However, application of such films for instance in OSC or OLED, which require charge extraction / injection on the entire device active area, will result in issues. Taking a limited lateral conductivity of organic materials into account, this would result in severely deteriorated device performance. Aside from this, a very low adhesion of AgNW meshes on the substrate [240] must be improved for more robust device applications.

To overcome these obstacles, the μm^2-areas in between the wires must be filled with a conductive transparent medium. For this, solution processed PEDOT:PSS [5, 243-245], also in combination with low-temperature TiO_x [246], was introduced to the NW mesh. However, using PEDOT:PSS should be reduced for stability reasons, as discussed previously in **Chapter 3**. Alternatively, metal oxide (TiO_2 [244], ZnO [6, 247] and AZO [248]) NP dispersions were used, which typically required post-deposition sintering at 140 to 250°C to improve adhesion and adjust the conductivity of the hybrid layer. Recently, high efficiency OSCs with *RT* solution-processed transparent hybrid electrode using ITO-NPs were demonstrated.[249, 250] Nevertheless, concerning the indium costs, this approach appears less attractive.

In this work, very promising PEDOT:PSS- and In-free robust hybrid coatings of *RT* liquid-processed AgNWs and sol-gel tin oxide ($sSnO_x$) for transparent electrodes in OSCs are realized. In addition to solution-

processed metal oxides, Al:ZnO prepared by ALD has been considered in this study. Very recent studies on metal oxide deposition via atmospheric pressure ALD [251, 252] demonstrated perspectives of integration of this originally vacuum-based technique into a R2R production line. Simultaneously, goals of increasing the ALD deposition rates for high through-put film fabrication are being pursued.[253]

5.2. Processing and characterization of hybrid layers

AgNW coatings are spin-coated from environmentally friendly isopropanol dispersion of nano-wires of 90 nm in diameter and several tens of µm length. These wires are free of polymeric dispersion agents. **Figure 5.2.1.-a** depicts an SEM-micrograph of spin-coated AgNW-mesh on glass at 900 V acceleration potential of the primary electron beam. At this voltage, the charge accumulated by the sample during the electron bombardment is balanced by the amount of charge that leaves the substrate as secondary (SE) and backscattered electrons.[254, 255]

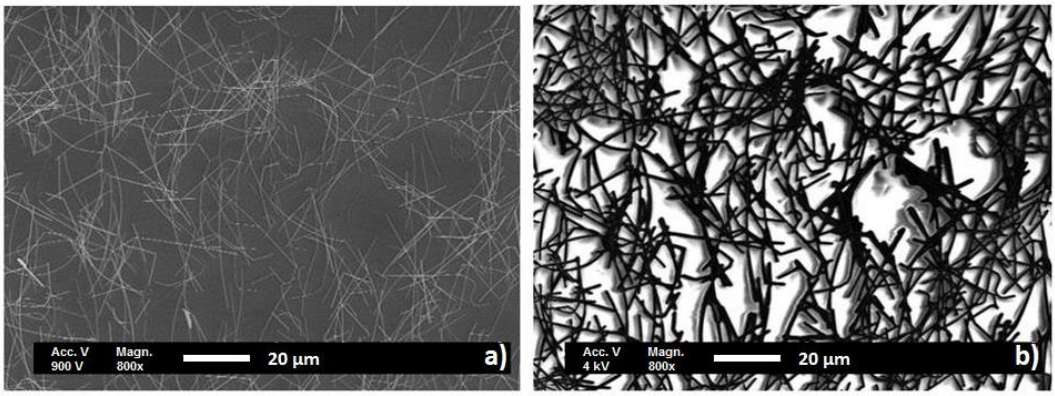

Figure 5.2.1. SEM-image of as-casted AgNW-mesh on glass taken at primary beam accelerating potentials of 900 V (a) and 4 kV (b).

The same image taken at 4 kV (**Figure 5.2.1.-b**) exhibits aside from material contrast a stark electron beam induced potential contrast (EBIP), as the balance between in- and outcoming charge is distorted due to different sample ionization cross-sections for higher primary *e*-beam

energy. It is clearly seen that sample areas close to the grounded NW mesh appear dark, as the induced charge can be efficiently transported to ground via the highly conductive NW-mesh. Opposed to that, insulating glass regions not covered with AgNWs accumulate and immobilize the negative charge, which induces the potential contrast overlapped with (always present) material contrast. This clearly illustrates the necessity of improvement of lateral charge transport for neat AgNW-meshes, if these films are to be used in whole-area devices, like OSCs.

To obtain the whole-area contact in the following, the AgNW mesh is coated with $sSnO_x$ or ALD-AZO. The metal oxide deposition parameters were chosen in the way that 80 nm thickness of the oxide would be achieved on a planar glass substrate without NW mesh. For sol-gel deposition of SnO_x at *RT*, a recipe based on acetylacetone-stabilized tetrakis(diethylamino)tin(IV) introduced earlier by our group is used.[199] For ALD-AZO, the nano-laminate recipe using diethylzinc and trimethylaluminum (TMA) interacting with H_2O was used.[256]

The AgNWs coated with $sSnO_x$ and ALD-AZO are depicted in **Figure 5.2.2.-a, b**. It is seen that the NWs are nicely imbedded into the oxide matrix in both cases and the metal oxide joins the wires at their interconnects. Interestingly, much thicker wire diameter is observed for ALD-AZO (80 nm oxide – 90 nm wire – 80 nm oxide) coating demonstrating the conformal three-dimensional coating, which is a unique feature of the ALD technique. Also, the formation of nano-crystallites is observed for AZO coatings, as zinc oxide tends to crystallize even at low (<100°C) temperatures.[257, 258]

The fusion of NWs at their crossing via metal oxides results in dramatic reduction of layer sheet resistance (**Table 5.2.1**). Using $sSnO_x$, R_{sh} of 5.2 Ω/sq is achieved for hybrid coating, as compared to neat AgNW-mesh having 90 Ω/sq. Using AZO, somewhat higher R_{sh} of 31 Ω/sq is achieved, despite the fact that AZO processed at 100°C exhibits the specific electrical conductivity 4 orders of magnitude higher (1 S/cm) than $sSnO_x$

(10^{-4} S/cm) processed at *RT*. This clearly demonstrates the importance of effective NW fusion at the wire-to-wire crossing junctions for samples, where the long-range charge transport is dominated by the NWs.

Despite the relatively large NW diameter (90 nm), it is not necessary to cover them completely to ensure the effective NW-fusion and low R_{sh}, as demonstrated in **Figure 5.2.2.-c**. The R_{sh} drops and saturates already for 10 nm $sSnO_x$ or 32 nm of AZO. This might be preferential for applications, where the lower film thickness can be tolerated and parasitic optical absorption of the metal oxide bulk (e.g. AZO) should be reduced.

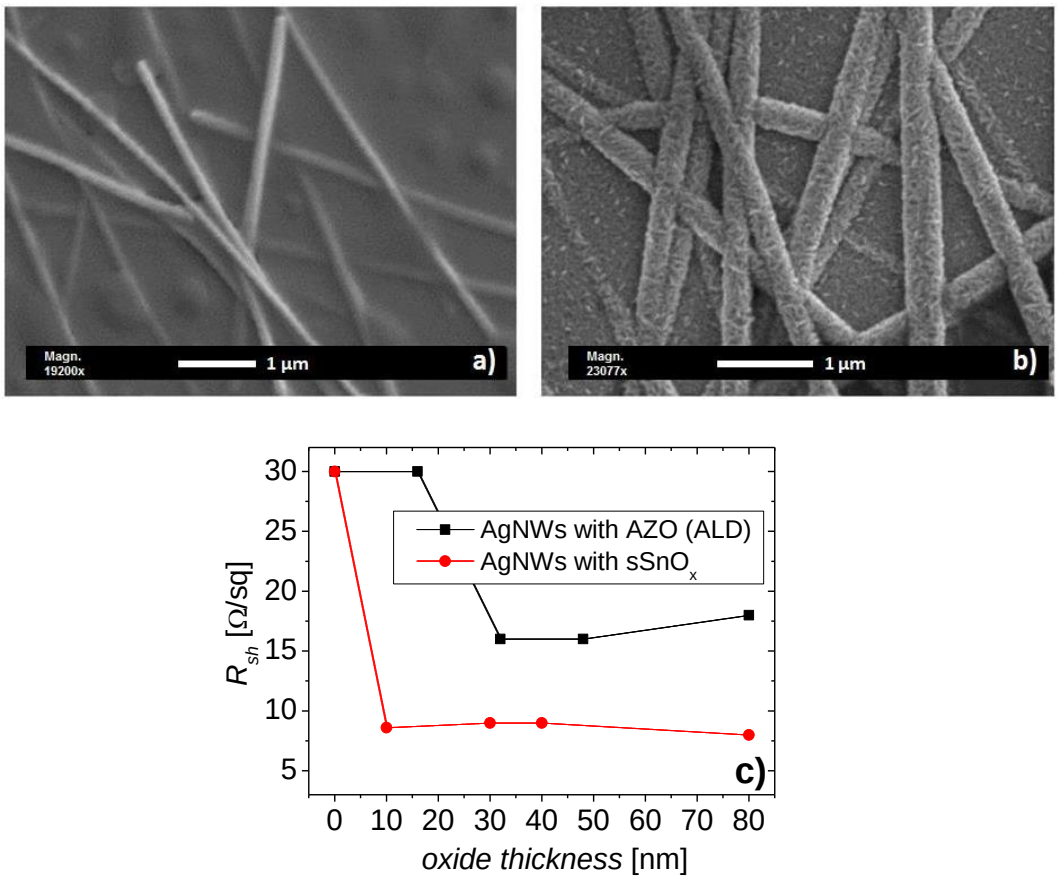

Figure 5.2.2. Magnified SEM-images of AgNWs coated with sol-gel SnOx (a), ALD-AZO (b); plot illustrating the dependency of sheet resistance of the hybrid layers on the thickness of metal oxide (c).

Figure 5.2.3. shows the SEM micrographs of hybrid layers comprising AgNWs/sSnO_x (a, c) and AgNWs/ALD-AZO (b, d) at 900 V and 4 kV acceleration potential respectively. As opposed to pristine AgNW-meshes (**Figure 5.2.1**), no potential contrast (only material contrast) in hybrid coatings is induced at higher energies, which qualitatively demonstrates an efficient lateral charge transport across the entire composite area.

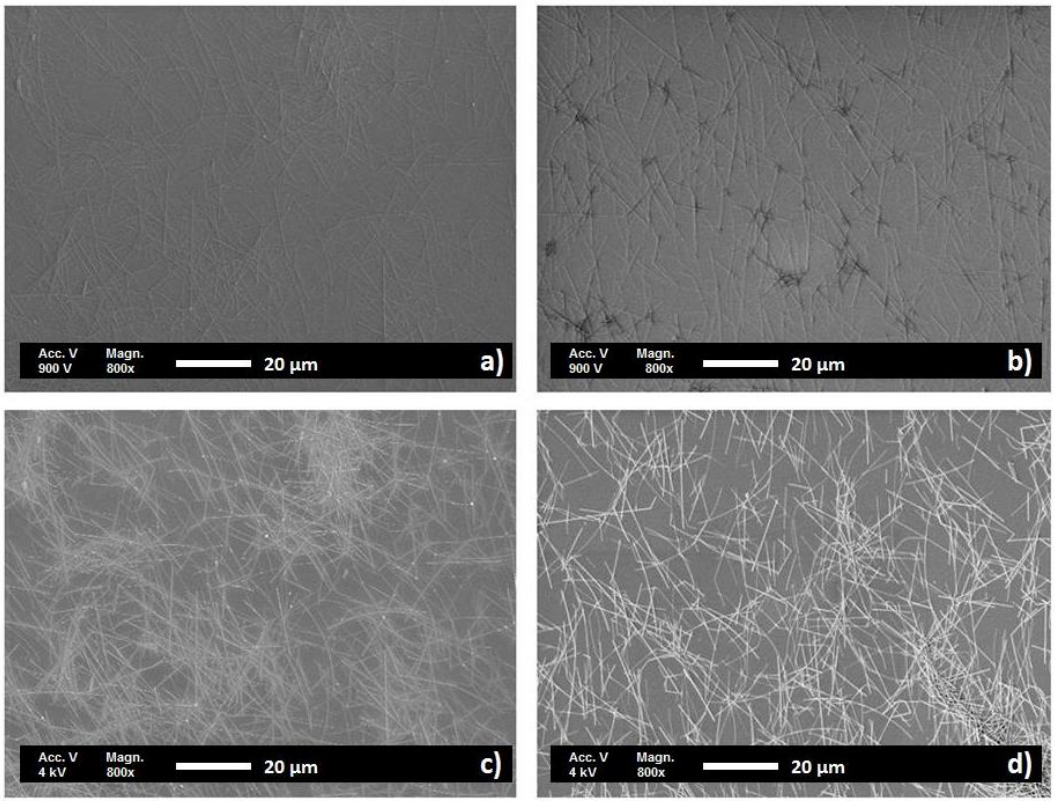

Figure 5.2.3. SEM-images of hybrid layers: AgNWs/sSnO_x (a, c) and AgNWs/ALD-AZO (b, d) for 900 V and 4 kV acceleration potential respectively.

The AFM surface morphology studies reveal high surface roughness of 65 nm rms for neat AgNW films on scan area of 50 x 50 µm (not shown here). Somewhat smoother surface (34 nm rms) is achieved for hybrid layers with sSnO_x. Due to the conformal ALD coating, the hybrid layers with AZO show increased roughness of 81 nm rms. The planarization of AgNWs previous to deposition of metal oxides is not considered in this work. However, well-established planarization concepts [240] could be combined

with this approach and make the use of these hybrid layers also as a bottom electrode for thin film devices possible.

Targeting the electro-optical applications, the optical properties of the hybrid transparent electrodes are studied in the following. Due to the random distribution of NWs on the substrate, a pronounced scattering of incident light has to be taken into account, distinguishing between the so called specular (non-scattered collimated light) and diffusive (total, incl. light scattered to angles other than 0°) transmission. This is done at different angles and distances to detector using the HeNe-laser at 632.8 nm (see **Appendix B.2** for experimental details). The corresponding specular transmission and its ratio to the diffusive transmission (integrated over the half-sphere after passing the sample) are listed in the **Table 5.2.1**. The neat AgNW-film transmits 79% of 632.8 nm light without scattering (specular transmission), whereas this value is slightly lower for both hybrid layers (72%). This is associated with the presence of metal oxide in the NW surrounding, as discussed in the following.

Table 5.2.1. T_{av} (integrated in range of 350 to 900 nm) and R_{sh} for hybrid layers; numbers for specular and diffusive transmission of hybrid layers at 632.8 nm laser wavelength. For reference, the data for room-temperature processed ITO [11] (ITO_{RT}) is shown.

	AgNWs on glass	AgNWs/ $sSnO_x$	AgNWs/ ALD-AZO	ITO_{RT} (60 nm)
R_{sh} [Ω/sq]	90	5.2	31	83
T_{av} [%]	84	81	80	-
T_{av} (in ref. to glass) [%]	90	87	86	85
$T_{specular}$ at 632.8 nm [%]	79	72	72	-
$T_{specular}/T_{diffusive}$ [%]	82	81	77	-

The scattering is almost independent on the scattering angle for such stochastic structures as composite electrodes discussed here (**Figure 5.2.6.-b**). Thus, the estimated ratio of specular-to-diffusive transmission is used to calibrate scattering spectra with respect to the specular transmittance.

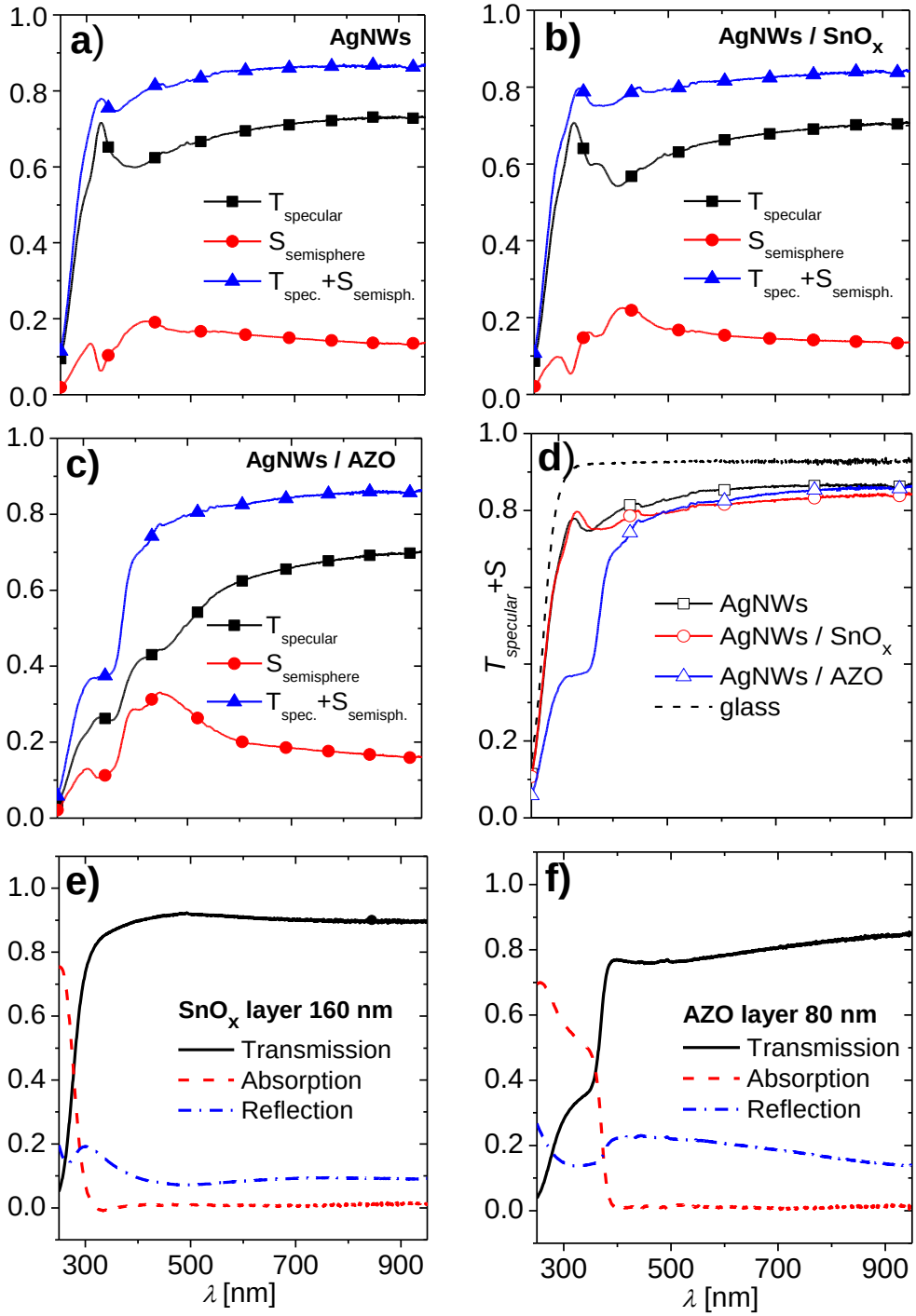

Figure 5.2.4. Plots of specular transmittance ($T_{specular}$), semisphere-scattered and detected in 45° angle transmittance ($S_{semisphere}$), resulting total diffusive transmittance ($T_{specular}$ + $S_{semisphere}$) of: as-casted AgNWs on glass (a); AgNWs/sSnO$_x$ composite (b) and AgNWs/ALD-AZO composite (c); comparison of total diffusive transmittance of as-casted and metal-oxide coated AgNW mesh on glass (d); transmission, absorption and reflection spectra of sSnO$_x$ film (e) and ALD-AZO film (f) deposited on glass.

Considering the spectral specular transmission of neat AgNWs (**Figure 5.2.4.-a**), a characteristic maximum is found at 325 nm, which correlates with plasma frequency of silver. For higher wavelength, a slight decrease of transmission and simultaneous increase of semi-sphere scattering is estimated. This is due to surface-plasmon-polariton (SPP) interaction on boundary of silver and surrounding environment.[259] The superposition of specular and scattered transmitted spectra gives 90% overall average transmission in range from 350 to 900 nm, as referred to uncoated glass substrate.

The similar high average transparency of 87% (as referred to glass) for composites of AgNWs/sSnO$_x$ (**Figure 5.2.4.-b** and **Table 5.2.1**) is estimated, as the SnO$_x$ exhibits an absorption edge at 300 nm (**Figure 5.2.4.-e**). That high transmission in combination with low R_{sh} of 5.2 Ω/sq counts for one of the best metal NW-based electrodes (even processed at >140°C), as for now (**Figure 5.2.5**).

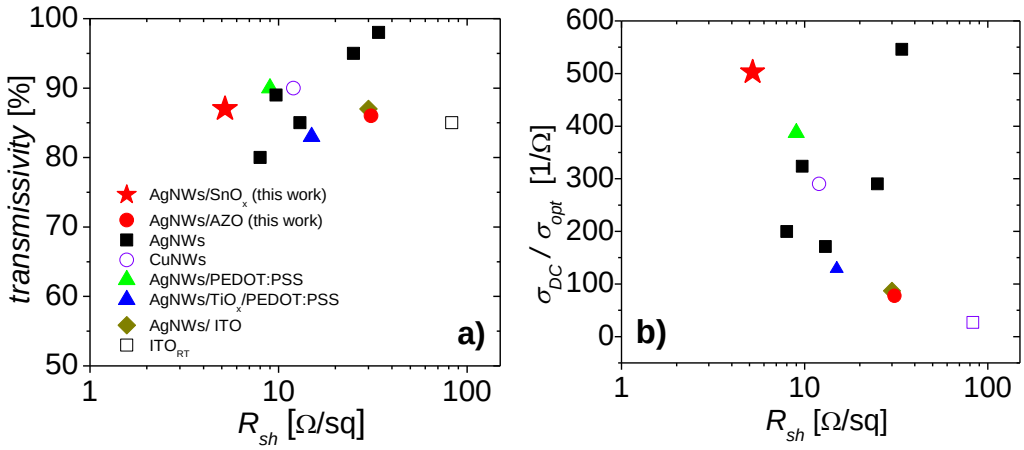

Figure 5.2.5. Characteristics (R_{sh} and transmittance) of various metal-NW based electrodes [11, 239, 240, 243, 244, 246, 249, 260] compared to the results of this work. The characteristics of ITO prepared at *RT* are stated for reference (a); corresponding figure of merit derived as the ratio of DC conductivity and optical conductivity (σ_{DC}/σ_{opt}) of the transparent conductive layers (b). (See [260] for details)

Interestingly, the minimum in the specular transmission is now found shifted to 420 nm (compare, 390 nm for pure AgNW film) and hints for

slightly increased scattering (**Figure 5.2.4.-b** and **5.2.6.-b**). The SPP resonance is known to shift towards longer wavelength with simultaneous rise of extinction (**Figure 5.2.6.-a**) by increasing the refractive index of the metal environment.[261, 262] After deposition of $sSnO_x$, the refractive index of the environment for the AgNWs changes from 1 (for air) to 1.62 @ 500 nm, as was estimated for $sSnO_x$. The SPPs can either be consumed by ohmic losses in silver and absorption by surrounding material, or re-emitted, causing an apparent diffusive transmission.

The more pronounced light scattering (**Figure 5.2.4.-c**) and extinction (**Figure 5.2.6.-a**) was estimated for AgNWs/ALD-AZO hybrid coatings, which correlates with the higher refractive index of AZO (2.04 @ 500 nm). Also, the intrinsic absorption of AZO sets on at 388 nm (**Figure 5.2.4.-f**) dominating the extinction spectrum. As a result, slightly lower total average transmittance of 86% (referred to glass) is estimated for AgNWs/ALD-AZO coatings (**Figure 5.2.4.-d** and **Table 5.2.1**). For comparison, ITO sputtered at *RT* exhibits T_{av} of 85% (referred to glass) and concomitant much higher R_{sh} of 83 Ω/sq.[11]

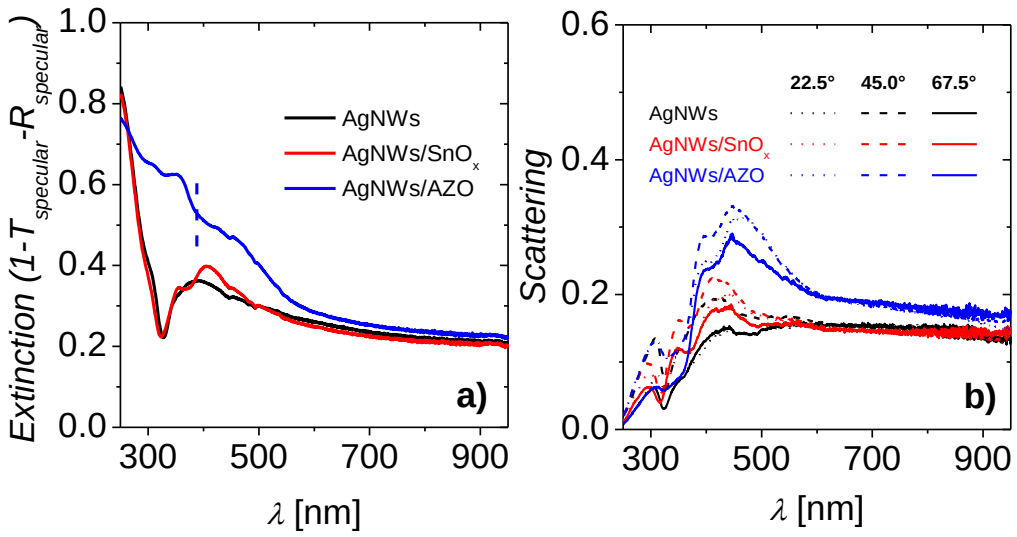

Figure 5.2.6. Incident light extinction spectra for AgNWs and composites of AgNWs/$sSnO_x$ and AgNWs/ALD-AZO (a) and light scattering spectra at various angles (b). Vertical dashed line indicates the absorption edge for AZO.

In general for OSCs, the semi-sphere light scattering due to SPP are not necessarily of negative effect. In contrary, such scattering can be used to optimize the light in-coupling into the photo-active layer, resulting in enhancement of device efficiency for the same BHJ thickness. In similar way, the same portion of light can then be converted by thinner layers of organic materials. Aside from lower material costs associated with this, this is also beneficial for active materials with limited charge carrier mobilities and issues in charge extraction from thicker layers.

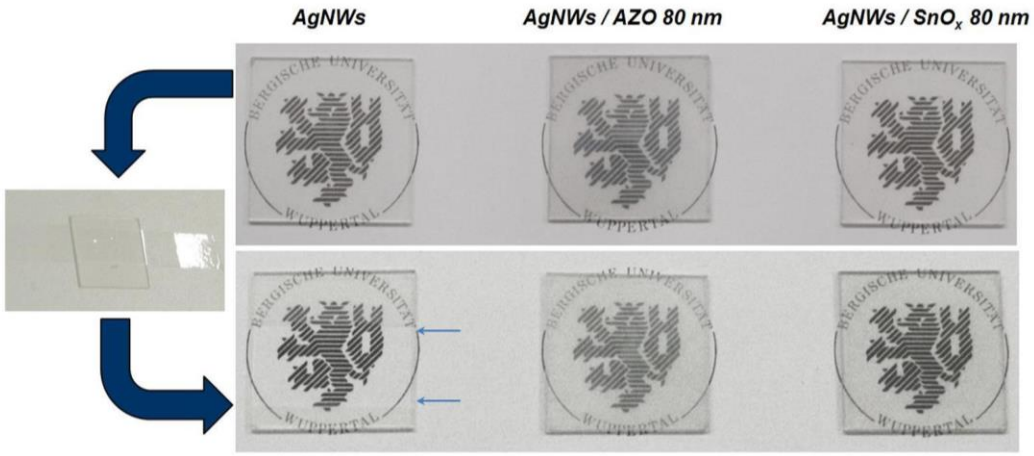

Figure 5.2.7. AgNWs mesh and composites of AgNWs/AZO and AgNWs/sSnO$_x$ on glass before (upper line) and after (lower line) scotch-tape peeling test. The blue arrows mark the peeled-off area.

The adhesion of the hybrid layers and concomitant conductive connection on the substrate is evaluated by applying the so called “scotch-tape peeling” test. As the **Figure 5.2.7** shows, the AgNWs non-coated with metal oxide “glue” are easily peeled off by the tape. This results in total loss of conductivity (**Table 5.2.2**). In contrast, AgNWs stabilized via metal oxide coating remain mechanically stable after peeling and maintain their low R_{sh}.

Finally, environmental stability of the composites is tested in climate cabinet for 7 days at 80°C and 80% *rH*. Neglecting the fluctuation due to finite experimental precision, the sheet resistance and the transparency remain unchanged for both composites.

Table 5.2.2. R_{sh} of AgNW mesh and composites of AgNWs/sSnO$_x$ and AgNWs/ALD-AZO before and after scotch-tape peeling test.

	R_{sh} [Ω/sq]		
	AgNWs	AgNWs/sSnO$_x$	AgNWs/ALD-AZO
before peeling	96	8	18
after peeling	-	8	18

With this broad knowledge on characteristics of composite AgNW/metal-oxide coatings the processing of the transparent electrodes is pursued in the following.

5.3. All-solution-processed inverted semitransparent OSCs

The functionality of the composite AgNW/metal-oxide transparent electrodes is demonstrated exemplarily for the AgNWs/sSnO$_x$ system. Without applying any planarization step for AgNW films the use of these in a thin film device is restricted to that as a top electrode. In this case, the high surface roughness exhibited by the composites does not cause short circuits in the device. The semitransparent inverted OSC stack, utilizing the composite electrode is depicted in **Figure 5.3.1.-a**. The device is realized on the standard glass/ITO and alternatively on Indium-free F:SnO$_2$ substrate. P3HT:PC$_{60}$BM is used as a photo-active layer for the first demonstration. In order to grant the proper hole extraction and protect the organics from eventual damage associated with sol-gel deposition of SnO$_x$, somewhat thicker films of sVO$_x$ (50 nm) and eMoO$_3$ (80 nm) are used on top of the organic layer. For a better controlled wettability and adhesion, the AgNW layers are coated with sSnO$_x$ precursor solution under nitrogen environment (to promote the “envelopment” of the wires with the sol-gel and prevent the immobilization of the sol-gel upon condensation already during the coating in the air) and then air-exposed for precursor hydrolysis and condensation. Finally, the devices with composite AgNW/sSnO$_x$ electrode are compared with the opaque reference, comprising a thermally evaporated metallic top electrode.

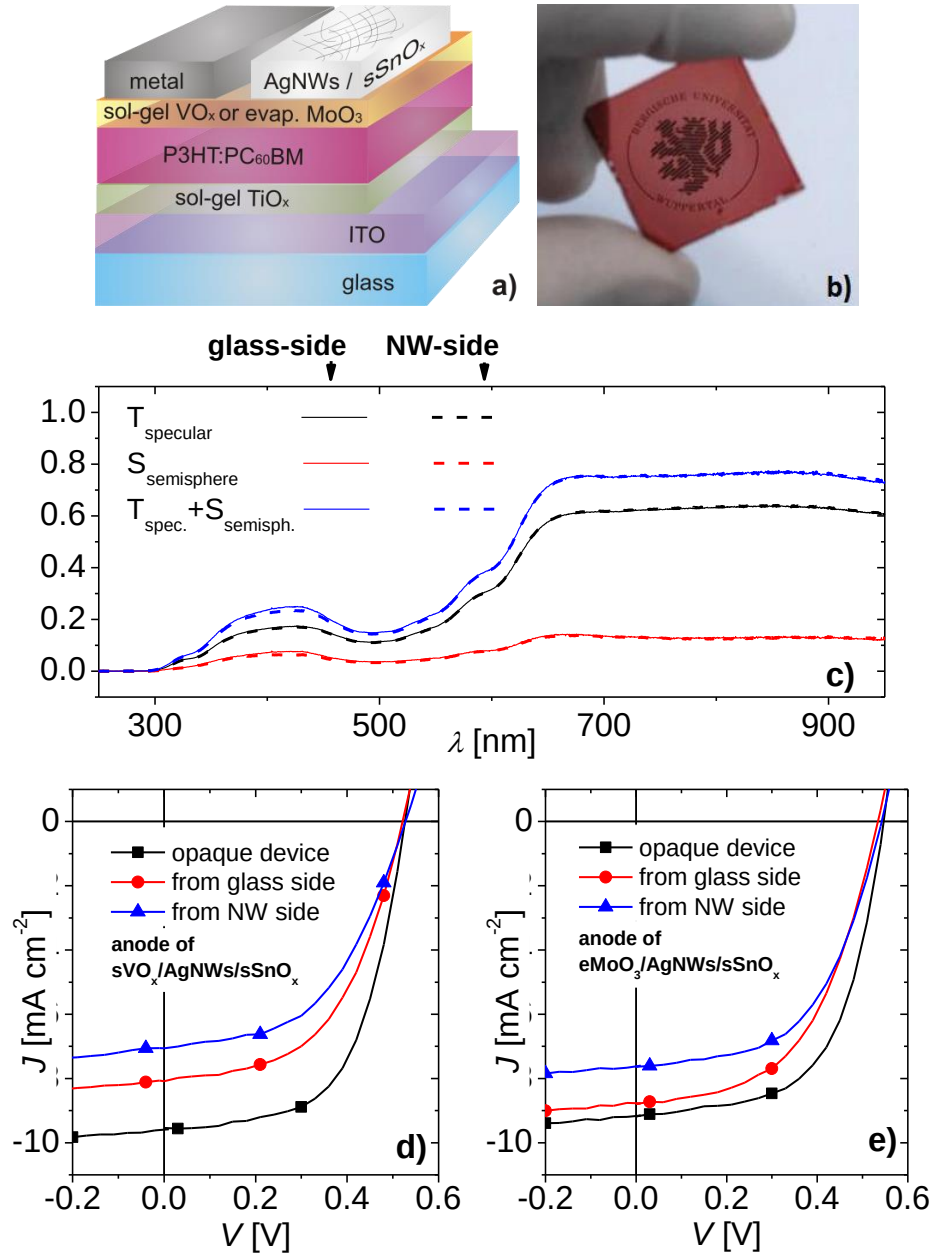

Figure 5.3.1. Layer sequence of the studied inverted OSCs (a); photo of large-area device stack comprising an anode of sVO_x/AgNWs/$sSnO_x$ (b); optical transmission spectrum ($T_{specular}$, $S_{semisphere}$ and their superposition) of the stack illuminated from glass side and from AgNWs/$sSnO_x$ top contact side (c); *JV* characteristics of all-solution-processed semitransparent inverted OSCs comprising sVO_x/AgNWs/$sSnO_x$ anode and opaque reference device with sVO_x/Al/Ag anode (d); *JV* characteristics of semitransparent inverted OSCs comprising $eMoO_3$/AgNWs/$sSnO_x$ anode and opaque reference device with $eMoO_3$/Al/Ag anode (e). Note, the bottom TCO for this run is ITO.

A photo of the complete device stack for the all-solution-processed semitransparent device is shown in **Figure 5.3.1.-b**. The optical transmittance of this stack in the red region starting at 650 nm accounts for >75% (**Figure 5.3.1.-c**) and is vastly independent on the illumination side (glass side or composite electrode side).

The resulting device characteristics including the opaque references are plotted in **Figure 5.3.1.-d, e** for sVO_x/AgNWs/$sSnO_x$ and $eMoO_3$/AgNWs/$sSnO_x$ electrodes respectively and summarized in **Table 5.3.1** (incl. data for F:SnO_2-based OSCs, not shown graphically).

Table 5.3.1. Characteristics of see-through inverted OSCs with liquid-processed AgNWs/$sSnO_x$ composite top contact and opaque reference device with thermally evaporated metallic top contact.

		PCE [%]	V_{oc} [V]	J_{sc} [mA/cm^2]	*FF* [%]
ITO/$sTiO_x$/BHJ/sVO_x/Al/Ag		3.0	0.53	9.6	59
ITO/$sTiO_x$/BHJ/ sVO_x/AgNWs/$sSnO_x$	glass side	2.2	0.52	8.1	53
	NW side	1.9	0.53	7.1	50
ITO/$sTiO_x$/BHJ/$eMoO_3$/Al/Ag		3.0	0.55	9.2	59
ITO/$sTiO_x$/BHJ/ $eMoO_3$/AgNWs/$sSnO_x$	glass side	2.5	0.53	8.8	52
	NW side	2.2	0.54	7.6	54
F:SnO_2/$sTiO_x$/BHJ/ $eMoO_3$/AgNWs/$sSnO_x$	glass side	2.4	0.53	8.8	51
	NW side	2.0	0.52	7.7	50

An efficiency of 3.0% (typical for P3HT:PC_{60}BM) is achieved for opaque reference devices with both sVO_x and $eMoO_3$ anode interlayers (see **Chapter 3**). The semitransparent cells with $eMoO_3$/AgNWs/$sSnO_x$ show *PCE* of up to 2.5%. As expected, the semitransparent devices exhibit lower *PCE*, for the light is only absorbed as it passes through the BHJ once without being fully reflected back by the metallic mirror of the top electrode as in reference devices. A lower J_{sc} is obtained for semitransparent devices, if illuminated from the AgNW-side rather than from the glass side, as the light is scattered back on the NW-mesh.

Further, for semitransparent devices comprising a thick VO_x, especially if illuminated from the top electrode side, lower *PCE* is achieved due to

parasitic absorption in the VO_x bulk (see **Chapter 3.2**), compared to $eMoO_3$. The semitransparent devices with sVO_x and $eMoO_3$, however, demonstrate similar high *FF*, which hints for efficient charge collection via the composite electrode. Still the *FF* of AgNW-based devices is somewhat lower than the *FF* of the reference. To improve this, the interface electronics between the anodic charge extraction layer and $sSnO_x$ as well as the lateral distribution of NWs on the substrate may require further optimization.

Despite the low R_{sh} of the composite electrodes, the series resistance through the device counts for 4 Ω cm^2. That is twice as high as the one for opaque reference with metallic contact. This is associated with a non-optimized energetics at the interface between the high *WF* metal oxide and $sSnO_x$. Note that in previous reports devoted to AgNWs/PEDOT:PSS electrode a five-fold increase of series resistance was evidenced in comparison to opaque reference, which was explained by limited contact of the electrode to the underlying stack.[244]

Finally, as a proof of concept, completely In-free semitransparent OSCs comprising the solution-processed AgNWs/$sSnO_x$ electrodes are fabricated on lithographically pre-patterned F:SnO_2 substrates. Essentially the same device characteristics (**Table 5.3.1**), as on ITO, are obtained.

5.4. Summary

In this chapter, the realization of hybrid transparent conductive coatings of AgNWs/sol-gel SnO_x processed at *RT* or AgNWs/ALD-AZO processed at moderate foil-friendly 100°C reactor temperature is addressed. Both metal oxide deposition approaches (sol-gel and ALD) have great potential for cost-effective device fabrication. The introduction of metal oxides to NW mesh results in effective fusing at wire-to-wire junction. The films demonstrate high average transparency (up to 87%, as referred to glass) and low sheet resistivity (down to 5.2 Ω/sq), outperforming commercial ITO in both categories. Further, due to filling of inter-wire space with these

moderately conductive oxides the lateral charge transport across the entire film area is granted. The coatings exhibit outstanding environmental and mechanical stability and adhesion on the substrate. Finally, the functionality of the hybrid coating as an electrode was successfully tested in all-solution-processed inverted semitransparent OSC.

6. Conclusions and outlook

Large-scale and high-throughput production of organic solar cells e.g. by solution based deposition techniques will become a key for its successful commercialization. For this purpose, processing of all the layers (transparent electrodes, photo-active layer and charge extraction interlayers) in the organic device stack from solution is required. The use of flexible plastic substrates for the R2R device fabrication sets additional constraints regarding temperature range (<150°C). In this thesis, the solution-based deposition of transparent charge extraction interlayers and transparent electrodes at low processing temperatures has been addressed.

At the anode side, sol-gel processing of high work-function metal oxides VO_x and MoO_x is introduced and discussed. Extremely smooth thin films of both metal oxides have been realized from environmentally benign alcoholic sol-gel solutions even at room temperature. The resulting metal-oxides have been evidenced to exhibit an electronic structure very similar to that of the thermally evaporated counterparts in organic solar cells, both metal oxides lead to outstanding device performance comparable or better than that of reference devices with metal oxides prepared in costly high-vacuum processes. Importantly, the use of these solution-based metal oxides allows for an efficient replacement of the commonly used PEDOT:PSS that causes severe reliability and lifetime issues. Using metal oxides, a dramatic improvement of the lifetime of the organic solar cells has been demonstrated.

In the inverted device architecture, the anode interlayer must be processed on top of the sensitive photo-active organic film. The choice of proper processing conditions (solution concentration, aging) is mandatory to avoid the penetration of the precursor into the photo-active layer and deterioration of the device performance. This optimization is based on a variety of analytical results that evidenced a p-type doping effect of the organic material by the metal oxide formed from the penetrated sol-gel

precursor. In optimized devices, the sol-gel derived vanadium oxide on top of the organic layer results in device efficiencies comparable and better than that of the devices based on the thermally evaporated V_2O_5.

At the cathode side of inverted solar cells, the lowering of the ITO work-function by ultra-thin films of conjugated polyelectrolyte P3ImHT processed from alcoholic solvent was investigated. This work has been done in close collaboration with the group of Prof. Dr. Scherf. This approach is a promising and potentially more facile alternative to the more conventional solution-based processing of low work-function metal oxides, like TiO_x, ZnO. The inverted organic solar cells based on the CPE-modified ITO exhibit comparable efficiency as the devices comprising the titania cathode interlayer. Even though the working mechanism of CPEs is still a topic of research and not fully clarified yet, it has been demonstrated that the ultra-thin CPE builds up an interface dipole causing the reduction of the ITO work-function. It has been found that the absolute reduction of the work-function of an electrode depends on the initial work-function of the substrate. Only a small change of the work-function is found for substrates with a work-function < 4.4 eV. It is, therefore, speculated that the formation of an interface dipole due to charge transfer driven by the difference in chemical potentials of the oxide substrate and the adsorbed molecular ensemble is predominantly responsible for the reduction of the substrate work-function.

Ultimately, entirely solution-processed semi-transparent organic solar cells have been prepared. To this end, liquid-processed transparent electrodes comprising highly conductive and transparent meshes of silver nano-wires glued together by moderately conductive and transparent sol-gel processed tin oxide have been developed. The metal oxide within the composite electrode provides an outstanding mechanical and environmental stability to the electrode and reduces the contact resistance on the NW interconnects. Moreover it allows making an electrical contact on the entire active device area.

As of yet, the combination of the high transparency and resulting low sheet resistance of AgNW/SnO_x composite films, achieved in this work, makes it one of the best transparent conductive coatings even when compared to others, which have been processed at substantially higher temperatures (>100°C). The use of the AgNW/SnO_x composite as a top electrode led to the realization of entirely solution-processed indium- and PEDOT:PSS-free inverted semitransparent efficient OSCs.

For now, this work has hopefully made a significant contribution to the solution-based processing of OPV. Still, as stated above, some additional study should be carried out to satisfy an academic interest and render the deposition processes industry-ready. Especially, going from-lab-to-fab, a number of properties of the sol-gel oxide ink formulation, e.g. viscosity, solvent vapor pressure, sol reactivity, stability and dynamics of oxide formation, post-treatment techniques alternative to the heat must be investigated and adjusted to fit in the production line. A deeper spectroscopic study is required to understand the underlying mechanism of the interface dipole formation on the oxide surface due to adsorption of polar organic molecules in order to even more efficiently modify the work-function at the cathodic or anodic interface, thus, creating the prerequisites for high efficiency devices. Considering the composite electrodes comprising the metal nano-wires, a planarization of the stochastically distributed wires is highly desired in order to realize the low-temperature liquid-processed (transparent) bottom electrodes. Combining these findings with high efficiency absorbing materials has a great potential for OPV commercialization.

7. References

[1] www.heliatek.de.

[2] www.polyera.com.

[3] J. B. You, L. T. Dou, K. Yoshimura, T. Kato, K. Ohya, T. Moriarty, K. Emery, C. C. Chen, J. Gao, G. Li, Y. Yang, "A polymer tandem solar cell with 10.6% power conversion efficiency", *Nat Commun* **2013**, 4, 1446.

[4] N. Espinosa, R. Garcia-Valverde, A. Urbina, F. Lenzmann, M. Manceau, D. Angmo, F. C. Krebs, "Life cycle assessment of ITO-free flexible polymer solar cells prepared by roll-to-roll coating and printing", *Sol Energ Mat Sol C* **2012**, 97, 3.

[5] L. Q. Yang, T. Zhang, H. X. Zhou, S. C. Price, B. J. Wiley, W. You, "Solution-Processed Flexible Polymer Solar Cells with Silver Nanowire Electrodes", *ACS applied materials & interfaces* **2011**, 3, 4075.

[6] J. Ajuria, I. Ugarte, W. Cambarau, I. Etxebarria, R. Tena-Zaera, R. Pacios, "Insights on the working principles of flexible and efficient ITO-free organic solar cells based on solution processed Ag nanowire electrodes", *Sol Energ Mat Sol C* **2012**, 102, 148.

[7] D. Angmo, F. C. Krebs, "Flexible ITO-Free Polymer Solar Cells", *J Appl Polym Sci* **2013**, 129, 1.

[8] Z. F. Duan, S. Fujii, Z. Liu, T. Okukawa, A. Yoshida, Y. Yanagi, H. Kataura, G. Y. Zhao, Y. Nishioka, "Flexible Organic Solar Cells Based on Spin-Coated Blend Films of a Phenylene-Thiophene Oligomer Derivative and PCBM", *Mol Cryst Liq Cryst* **2013**, 578, 78.

[9] H. P. Jen, M. H. Lin, L. L. Li, H. P. Wu, W. K. Huang, P. J. Cheng, E. W. G. Diau, "High-Performance Large-Scale Flexible Dye-Sensitized Solar Cells Based on Anodic TiO2 Nanotube Arrays", *ACS applied materials & interfaces* **2013**, 5, 10098.

[10] J. Yun, W. Wang, T. S. Bae, Y. H. Park, Y. C. Kang, D. H. Kim, S. Lee, G. H. Lee, M. Song, J. W. Kang, "Preparation of Flexible Organic Solar Cells with Highly Conductive and Transparent Metal-Oxide Multilayer Electrodes Based on Silver Oxide", *ACS applied materials & interfaces* **2013**, 5, 9933.

[11] T. Winkler, H. Schmidt, H. Flugge, F. Nikolayzik, I. Baumann, S. Schmale, T. Weimann, P. Hinze, H. H. Johannes, T. Rabe, S. Hamwi, T. Riedl, W. Kowalsky, "Efficient large area semitransparent organic solar cells based on highly transparent and conductive ZTO/Ag/ZTO multilayer top electrodes", *Org Electron* **2011**, 12, 1612.

[12] J. Meiss, K. Leo, M. K. Riede, C. Uhrich, W. M. Gnehr, S. Sonntag, M. Pfeiffer, "Efficient semitransparent small-molecule organic solar cells", *Appl Phys Lett* **2009**, 95, 213306.

[13] J. Meiss, T. Menke, K. Leo, C. Uhrich, W. M. Gnehr, S. Sonntag, M. Pfeiffer, M. Riede, "Highly efficient semitransparent tandem organic solar cells with complementary absorber materials", *Appl Phys Lett* **2011**, 99, 043301.

[14] F. Guo, X. D. Zhu, K. Forberich, J. Krantz, T. Stubhan, M. Salinas, M. Halik, S. Spallek, B. Butz, E. Spiecker, T. Ameri, N. Li, P. Kubis, D. M. Guldi, G. J. Matt, C. J. Brabec, "ITO-Free and Fully Solution-Processed Semitransparent Organic Solar Cells with High Fill Factors", *Adv Energy Mater* **2013**, 3, 1062.

[15] F. C. Krebs, "Stability, degradation, and operational lifetimes of fully solution R2R processed flexible polymer solar cells", *Abstr Pap Am Chem S* **2009**, 238.

[16] M. Manceau, D. Angmo, M. Jorgensen, F. C. Krebs, "ITO-free flexible polymer solar cells: From small model devices to roll-to-roll processed large modules", *Org Electron* **2011**, 12, 566.

[17] H. Hoppe, N. S. Sariciftci, D. Meissner, "Optical constants of conjugated polymer/fullerene based bulk-heterojunction organic solar cells", *Mol Cryst Liq Cryst* **2002**, 385, 233.

[18] J. L. Bredas, G. B. Street, "Polarons, Bipolarons, and Solitons in Conducting Polymers", *Accounts Chem Res* **1985**, 18, 309.

[19] T. Izumi, S. Kobashi, K. Takimiya, Y. Aso, T. Otsubo, "Synthesis and spectroscopic properties of a series of beta-blocked long oligothiophenes up to the 96-mer: Revaluation of effective conjugation length", *J Am Chem Soc* **2003**, 125, 5286.

[20] J. L. Bredas, J. E. Norton, J. Cornil, V. Coropceanu, "Molecular Understanding of Organic Solar Cells: The Challenges", *Accounts Chem Res* **2009**, 42, 1691.

[21] H. Sirringhaus, "Device physics of Solution-processed organic field-effect transistors", *Adv Mater* **2005**, 17, 2411.

[22] C. D. Dimitrakopoulos, D. J. Mascaro, "Organic thin-film transistors: A review of recent advances", *Ibm J Res Dev* **2001**, 45, 11.

[23] N. Tessler, Y. Preezant, N. Rappaport, Y. Roichman, "Charge Transport in Disordered Organic Materials and Its Relevance to Thin-Film Devices: A Tutorial Review", *Adv Mater* **2009**, 21, 2741.

[24] R. N. Marks, J. J. M. Halls, D. D. C. Bradley, R. H. Friend, A. B. Holmes, "The Photovoltaic Response in Poly(P-Phenylene Vinylene) Thin-Film Devices", *J Phys-Condens Mat* **1994**, 6, 1379.

[25] S. Barth, H. Bassler, "Intrinsic photoconduction in PPV-type conjugated polymers", *Physical review letters* **1997**, 79, 4445.

[26] B. A. Gregg, "Excitonic solar cells", *J Phys Chem B* **2003**, 107, 4688.

[27] T. J. Savenije, J. M. Warman, A. Goossens, "Visible light sensitisation of titanium dioxide using a phenylene vinylene polymer", *Chem Phys Lett* **1998**, 287, 148.

[28] L. A. A. Pettersson, L. S. Roman, O. Inganas, "Modeling photocurrent action spectra of photovoltaic devices based on organic thin films", *J Appl Phys* **1999**, 86, 487.

[29] M. Stoessel, G. Wittmann, J. Staudigel, F. Steuber, J. Blassing, W. Roth, H. Klausmann, W. Rogler, J. Simmerer, A. Winnacker, M. Inbasekaran, E. P. Woo, "Cathode-induced luminescence quenching in polyfluorenes", *J Appl Phys* **2000**, 87, 4467.

[30] J. M. Nunzi, "Organic photovoltaic materials and devices", *Cr Phys* **2002**, 3, 523.

[31] B. Schweitzer, H. Bassler, "Excitons in conjugated polymers", *Synthetic Met* **2000**, 109, 1.

[32] A. Haugeneder, M. Neges, C. Kallinger, W. Spirkl, U. Lemmer, J. Feldmann, U. Scherf, E. Harth, A. Gugel, K. Mullen, "Exciton diffusion and dissociation in conjugated polymer fullerene blends and heterostructures", *Phys Rev B* **1999**, 59, 15346.

[33] G. Zerza, C. J. Brabec, G. Cerullo, S. De Silvestri, N. S. Sariciftci, "Ultrafast charge transfer in conjugated polymer-fullerene composites", *Synthetic Met* **2001**, 119, 637.

[34] N. S. Sariciftci, L. Smilowitz, A. J. Heeger, F. Wudl, "Photoinduced Electron-Transfer from a Conducting Polymer to Buckminsterfullerene", *Science* **1992**, 258, 1474.

[35] L. Smilowitz, N. S. Sariciftci, R. Wu, C. Gettinger, A. J. Heeger, F. Wudl, "Photoexcitation Spectroscopy of Conducting-Polymer-C(60) Composites - Photoinduced Electron-Transfer", *Phys Rev B* **1993**, 47, 13835.

[36] X. Wei, Z. V. Vardeny, N. S. Sariciftci, A. J. Heeger, "Absorption-detected magnetic-resonance studies of photoexcitations in conjugated-polymer/C-60 composites", *Phys Rev B* **1996**, 53, 2187.

[37] N. S. Sariciftci, L. Smilowitz, A. J. Heeger, F. Wudl, "Semiconducting Polymers (as Donors) and Buckminsterfullerene (as Acceptor) - Photoinduced Electron-Transfer and Heterojunction Devices", *Synthetic Met* **1993**, 59, 333.

[38] V. Dyakonov, G. Zoriniants, M. Scharber, C. J. Brabec, R. A. J. Janssen, J. C. Hummelen, N. S. Sariciftci, "Photoinduced charge carriers in conjugated polymer-fullerene composites studied with light-induced electron-spin resonance", *Phys Rev B* **1999**, 59, 8019.

[39] J. De Ceuster, E. Goovaerts, A. Bouwen, J. C. Hummelen, V. Dyakonov, "High-frequency (95 GHz) electron paramagnetic resonance study of the photoinduced charge transfer in conjugated polymer-fullerene composites", *Phys Rev B* **2001**, 64, 195206.

[40] G. Yu, J. Gao, J. C. Hummelen, F. Wudl, A. J. Heeger, "Polymer Photovoltaic Cells - Enhanced Efficiencies Via a Network of Internal Donor-Acceptor Heterojunctions", *Science* **1995**, 270, 1789.

[41] R. J. Kline, M. D. McGehee, E. N. Kadnikova, J. S. Liu, J. M. J. Frechet, "Controlling the field-effect mobility of regioregular polythiophene by changing the molecular weight", *Adv Mater* **2003**, 15, 1519.

[42] A. Zen, J. Pflaum, S. Hirschmann, W. Zhuang, F. Jaiser, U. Asawapirom, J. P. Rabe, U. Scherf, D. Neher, "Effect of molecular weight and annealing of poly (3-hexylthiophene)s on the performance of organic field-effect transistors", *Adv Funct Mater* **2004**, 14, 757.

[43] J. Peet, C. Soci, R. C. Coffin, T. Q. Nguyen, A. Mikhailovsky, D. Moses, G. C. Bazan, "Method for increasing the photoconductive response in conjugated polymer/fullerene composites", *Appl Phys Lett* **2006**, 89, 252105

[44] W. L. Wang, H. B. Wu, C. Y. Yang, C. Luo, Y. Zhang, J. W. Chen, Y. Cao, "High-efficiency polymer photovoltaic devices from regioregular-poly(3-hexylthiophene-2,5-diyl) and [6,6]-phenyl-C-61-butyric acid methyl ester processed with oleic acid surfactant", *Appl Phys Lett* **2007**, 90, 183512.

[45] F. Padinger, R. S. Rittberger, N. S. Sariciftci, "Effects of postproduction treatment on plastic solar cells", *Adv Funct Mater* **2003**, 13, 85.

[46] B. A. Gregg, M. C. Hanna, "Comparing organic to inorganic photovoltaic cells: Theory, experiment, and simulation", *J Appl Phys* **2003**, 93, 3605.

[47] B. Kippelen, J. L. Bredas, "Organic photovoltaics", *Energ Environ Sci* **2009**, 2, 251.

[48] I. Riedel, J. Parisi, V. Dyakonov, L. Lutsen, D. Vanderzande, J. C. Hummelen, "Effect of temperature and illumination on the electrical characteristics of polymer-fullerene bulk-heterojunction solar cells", *Adv Funct Mater* **2004**, 14, 38.

[49] G. G. Malliaras, J. R. Salem, P. J. Brock, J. C. Scott, "Photovoltaic measurement of the built-in potential in organic light emitting diodes and photodiodes", *J Appl Phys* **1998**, 84, 1583.

[50] J. Liu, Y. J. Shi, Y. Yang, "Solvation-induced morphology effects on the performance of polymer-based photovoltaic devices", *Adv Funct Mater* **2001**, 11, 420.

[51] P. W. M. Blom, M. J. M. deJong, M. G. vanMunster, "Electric-field and temperature dependence of the hole mobility in poly(p-phenylene vinylene)", *Phys Rev B* **1997**, 55, R656.

[52] B. B. Chen, X. F. Qiao, C. M. Liu, C. Zhao, H. C. Chen, K. H. Wei, B. Hu, "Effects of bulk and interfacial charge accumulation on fill factor in organic solar cells", *Appl Phys Lett* **2013**, 102, 193302.

[53] G. F. A. Dibb, F. C. Jamieson, A. Maurano, J. Nelson, J. R. Durrant, "Limits on the Fill Factor in Organic Photovoltaics: Distinguishing Nongeminate and Geminate Recombination Mechanisms", *J Phys Chem Lett* **2013**, 4, 803.

[54] B. Y. Qi, J. Z. Wang, "Fill factor in organic solar cells", *Phys Chem Chem Phys* **2013**, 15, 8972.

[55] W. Tress, A. Merten, M. Furno, M. Hein, K. Leo, M. Riede, "Correlation of Absorption Profile and Fill Factor in Organic Solar Cells: The Role of Mobility Imbalance", *Adv Energy Mater* **2013**, 3, 631.

[56] W. Tress, S. Corvers, K. Leo, M. Riede, "Investigation of Driving Forces for Charge Extraction in Organic Solar Cells: Transient Photocurrent Measurements on Solar Cells Showing S-Shaped Current-Voltage Characteristics", *Adv Energy Mater* **2013**, 3, 873.

[57] V. D. Mihailetchi, L. J. A. Koster, P. W. M. Blom, "Effect of metal electrodes on the performance of polymer : fullerene bulk heterojunction solar cells", *Appl Phys Lett* **2004**, 85, 970.

[58] I. D. Parker, "Carrier Tunneling and Device Characteristics in Polymer Light-Emitting-Diodes", *J Appl Phys* **1994**, 75, 1656.

[59] H. Ishii, K. Sugiyama, E. Ito, K. Seki, "Energy level alignment and interfacial electronic structures at organic metal and organic organic interfaces", *Adv Mater* **1999**, 11, 605.

[60] Y. Hirose, A. Kahn, V. Aristov, P. Soukiassian, V. Bulovic, S. R. Forrest, "Chemistry and electronic properties of metal-organic semiconductor interfaces: Al, Ti, In, Sn, Ag, and Au on PTCDA", *Phys Rev B* **1996**, 54, 13748.

[61] L. Yan, Y. L. Gao, "Interfaces in organic semiconductor devices", *Thin Solid Films* **2002**, 417, 101.

[62] N. Koch, A. Kahn, J. Ghijsen, J. J. Pireaux, J. Schwartz, R. L. Johnson, A. Elschner, "Conjugated organic molecules on metal versus polymer electrodes: Demonstration of a key energy level alignment mechanism", *Appl Phys Lett* **2003**, 82, 70.

[63] S. C. Veenstra, H. T. Jonkman, "Energy-level alignment at metal-organic and organic-organic interfaces", *J Polym Sci Pol Phys* **2003**, 41, 2549.

[64] J. Blochwitz, T. Fritz, M. Pfeiffer, K. Leo, D. M. Alloway, P. A. Lee, N. R. Armstrong, "Interface electronic structure of organic semiconductors with controlled doping levels", *Org Electron* **2001**, 2, 97.

[65] J. Maibach, E. Mankel, T. Mayer, W. Jaegermann, "Synchrotron induced photoelectron spectroscopy on drop casted donor/acceptor bulk heterojunction: Orbital energy line up in DH6T/PCBM blends", *Surf Sci* **2013**, 612, L9.

[66] R. Hock, T. Mayer, W. Jaegermann, "p-Type Doping of Spiro-MeOTAD with WO3 and the Spiro-MeOTAD/WO3 Interface Investigated by Synchrotron-Induced Photoelectron Spectroscopy", *J Phys Chem C* **2012**, 116, 18146.

[67] D. Y. Kim, J. Subbiah, G. Sarasqueta, F. So, H. J. Ding, Irfan, Y. L. Gao, "The effect of molybdenum oxide interlayer on organic photovoltaic cells", *Appl Phys Lett* **2009**, 95, 093304

[68] M. A. Baldo, S. R. Forrest, "Interface-limited injection in amorphous organic semiconductors", *Phys Rev B* **2001**, 64, 085201.

[69] B. N. Limketkai, M. A. Baldo, "Charge injection into cathode-doped amorphous organic semiconductors", *Phys Rev B* **2005**, 71, 085207.

[70] Y. Park, V. Choong, Y. Gao, B. R. Hsieh, C. W. Tang, "Work function of indium tin oxide transparent conductor measured by photoelectron spectroscopy", *Appl Phys Lett* **1996**, 68, 2699.

[71] K. Sugiyama, H. Ishii, Y. Ouchi, K. Seki, "Dependence of indium-tin-oxide work function on surface cleaning method as studied by ultraviolet and x-ray photoemission spectroscopies", *J Appl Phys* **2000**, 87, 295.

[72] H. Ishii, K. Sugiyama, D. Yoshimura, E. Ito, Y. Ouchi, K. Seki, "Energy-level alignment at model interfaces of organic electroluminescent devices studied by UV photoemission: Trend in the deviation from the traditional way of estimating the interfacial electronic structures", *Ieee J Sel Top Quant* **1998**, 4, 24.

[73] I. G. Hill, D. Milliron, J. Schwartz, A. Kahn, "Organic semiconductor interfaces: electronic structure and transport properties", *Appl Surf Sci* **2000**, 166, 354.

[74] J. Hwang, A. Wan, A. Kahn, "Energetics of metal-organic interfaces: New experiments and assessment of the field", *Mat Sci Eng R* **2009**, 64, 1.

[75] Y. Hirose, C. I. Wu, V. Aristov, P. Soukiassian, A. Kahn, "Chemistry and electronic properties of metal contacts on an organic molecular semiconductor", *Appl Surf Sci* **1997**, 113, 291.

[76] H. Ishii, K. Seki, "Energy level alignment at organic/metal interfaces studied by UV photoemission: Breakdown of traditional assumption of a common vacuum level at the interface", *Ieee T Electron Dev* **1997**, 44, 1295.

[77] A. Rajagopal, A. Kahn, "Photoemission spectroscopy investigation of magnesium-Alq(3) interfaces", *J Appl Phys* **1998**, 84, 355.

[78] O. L. A. Monti, M. P. Steele, "Influence of electrostatic fields on molecular electronic structure: insights for interfacial charge transfer", *Phys Chem Chem Phys* **2010**, 12, 12390.

[79] G. Heimel, L. Romaner, J. L. Bredas, E. Zojer, "Interface energetics and level alignment at covalent metal-molecule junctions: pi-conjugated thiols on gold", *Physical review letters* **2006**, 96, 196806.

[80] G. Heimel, L. Romaner, E. Zojer, J. L. Bredas, "Toward control of the metal-organic interfacial electronic structure in molecular electronics: A first-principles study on

self-assembled monolayers of pi-conjugated molecules on noble metals", *Nano Lett* **2007**, 7, 932.

[81] D. A. Egger, E. Zojer, "Anticorrelation between the Evolution of Molecular Dipole Moments and Induced Work Function Modifications", *J Phys Chem Lett* **2013**, 4, 3521.

[82] C. J. Brabec, A. Cravino, D. Meissner, N. S. Sariciftci, T. Fromherz, M. T. Rispens, L. Sanchez, J. C. Hummelen, "Origin of the open circuit voltage of plastic solar cells", *Adv Funct Mater* **2001**, 11, 374.

[83] C. J. Brabec, A. Cravino, D. Meissner, N. S. Sariciftci, M. T. Rispens, L. Sanchez, J. C. Hummelen, T. Fromherz, "The influence of materials work function on the open circuit voltage of plastic solar cells", *Thin Solid Films* **2002**, 403, 368.

[84] V. D. Mihailetchi, P. W. M. Blom, J. C. Hummelen, M. T. Rispens, "Cathode dependence of the open-circuit voltage of polymer : fullerene bulk heterojunction solar cells", *J Appl Phys* **2003**, 94, 6849.

[85] M. T. Greiner, Z. H. Lu, "Thin-film metal oxides in organic semiconductor devices: their electronic structures, work functions and interfaces", *Npg Asia Mater* **2013**, 5, e55.

[86] K. X. Steirer, P. F. Ndione, N. E. Widjonarko, M. T. Lloyd, J. Meyer, E. L. Ratcliff, A. Kahn, N. R. Armstrong, C. J. Curtis, D. S. Ginley, J. J. Berry, D. C. Olson, "Enhanced Efficiency in Plastic Solar Cells via Energy Matched Solution Processed NiOx Interlayers", *Adv Energy Mater* **2011**, 1, 813.

[87] M. Y. Lin, C. Y. Lee, S. C. Shiu, I. J. Wang, J. Y. Sun, W. H. Wu, Y. H. Lin, J. S. Huang, C. F. Lin, "Sol-gel processed CuOx thin film as an anode interlayer for inverted polymer solar cells", *Org Electron* **2010**, 11, 1828.

[88] M. C. Gwinner, R. Di Pietro, Y. Vaynzof, K. J. Greenberg, P. K. H. Ho, R. H. Friend, H. Sirringhaus, "Doping of Organic Semiconductors Using Molybdenum Trioxide: a Quantitative Time-Dependent Electrical and Spectroscopic Study", *Adv Funct Mater* **2011**, 21, 1432.

[89] C. Tao, S. P. Ruan, G. H. Xie, X. Z. Kong, L. Shen, F. X. Meng, C. X. Liu, X. D. Zhang, W. Dong, W. Y. Chen, "Role of tungsten oxide in inverted polymer solar cells", *Appl Phys Lett* **2009**, 94, 043311.

[90] J. Meyer, S. Hamwi, S. Schmale, T. Winkler, H. H. Johannes, T. Riedl, W. Kowalsky, "A strategy towards p-type doping of organic materials with HOMO levels beyond 6 eV using tungsten oxide", *J Mater Chem* **2009**, 19, 702.

[91] M. T. Greiner, M. G. Helander, W. M. Tang, Z. B. Wang, J. Qiu, Z. H. Lu, "Universal energy-level alignment of molecules on metal oxides", *Nat Mater* **2012**, 11, 76.

[92] M. Kroger, S. Hamwi, J. Meyer, T. Riedl, W. Kowalsky, A. Kahn, "P-type doping of organic wide band gap materials by transition metal oxides: A case-study on Molybdenum trioxide", *Org Electron* **2009**, 10, 932.

[93] J. Meyer, S. Hamwi, M. Kroger, W. Kowalsky, T. Riedl, A. Kahn, "Transition Metal Oxides for Organic Electronics: Energetics, Device Physics and Applications", *Adv Mater* **2012**, 24, 5408.

[94] I. G. Hill, A. Rajagopal, A. Kahn, Y. Hu, "Molecular level alignment at organic semiconductor-metal interfaces", *Appl Phys Lett* **1998**, 73, 662.

[95] F. C. Krebs, "Polymer solar cell modules prepared using roll-to-roll methods: Knife-over-edge coating, slot-die coating and screen printing", *Sol Energ Mat Sol C* **2009**, 93, 465.

[96] M. Campoy-Quiles, T. Ferenczi, T. Agostinelli, P. G. Etchegoin, Y. Kim, T. D. Anthopoulos, P. N. Stavrinou, D. D. C. Bradley, J. Nelson, "Morphology evolution via self-organization and lateral and vertical diffusion in polymer: fullerene solar cell blends", *Nat Mater* **2008**, 7, 158.

[97] Y. Yao, J. H. Hou, Z. Xu, G. Li, Y. Yang, "Effect of solvent mixture on the nanoscale phase separation in polymer solar cells", *Adv Funct Mater* **2008**, 18, 1783.

[98] L. M. Chen, Z. R. Hong, G. Li, Y. Yang, "Recent Progress in Polymer Solar Cells: Manipulation of Polymer: Fullerene Morphology and the Formation of Efficient Inverted Polymer Solar Cells", *Adv Mater* **2009**, 21, 1434.

[99] Z. Xu, L. M. Chen, G. W. Yang, C. H. Huang, J. H. Hou, Y. Wu, G. Li, C. S. Hsu, Y. Yang, "Vertical Phase Separation in Poly(3-hexylthiophene): Fullerene Derivative Blends and its Advantage for Inverted Structure Solar Cells", *Adv Funct Mater* **2009**, 19, 1227.

[100] J. H. Choi, H. J. Choi, J. H. Shin, H. P. Kim, J. Jang, H. Lee, "Enhancement of organic solar cell efficiency by patterning the PEDOT: PSS hole transport layer using nanoimprint lithography", *Org Electron* **2013**, 14, 3180.

[101] A. D. Del Mauro, R. Diana, I. A. Grimaldi, F. Loffredo, P. Morvillo, F. Villani, C. Minarini, "Polymer solar cells with inkjet-printed doped-PEDOT: PSS anode", *Polym Composite* **2013**, 34, 1493.

[102] D. Gupta, M. M. Wienk, R. A. J. Janssen, "Efficient Polymer Solar Cells on Opaque Substrates with a Laminated PEDOT:PSS Top Electrode", *Adv Energy Mater* **2013**, 3, 782.

[103] W. Kim, N. Kim, J. K. Kim, I. Park, Y. S. Choi, D. H. Wang, H. Chae, J. H. Park, "Polymer Bulk Heterojunction Solar Cells with PEDOT:PSS Bilayer Structure as Hole Extraction Layer", *Chemsuschem* **2013**, 6, 1070.

[104] E. Lim, "Enhanced Photovoltaic Performance of P3HT:PCBM Cells by Modification of PEDOT:PSS Layer", *Mol Cryst Liq Cryst* **2013**, 585, 53.

[105] K. Lim, S. Jung, J. K. Kim, J. W. Kang, J. H. Kim, S. H. Choa, D. G. Kim, "Flexible PEDOT: PSS/ITO hybrid transparent conducting electrode for organic photovoltaics", *Sol Energ Mat Sol C* **2013**, 115, 71.

[106] J. S. Yeo, J. M. Yun, D. Y. Kim, S. S. Kim, S. I. Na, "Successive solvent-treated PEDOT:PSS electrodes for flexible ITO-free organic photovoltaics", *Sol Energ Mat Sol C* **2013**, 114, 104.

[107] G. T. Yue, J. H. Wu, Y. M. Xiao, J. M. Lin, M. L. Huang, L. Q. Fan, Y. Yao, "A dye-sensitized solar cell based on PEDOT:PSS counter electrode", *Chinese Sci Bull* **2013**, 58, 559.

[108] L. S. C. Pingree, B. A. MacLeod, D. S. Ginger, "The changing face of PEDOT : PSS films: Substrate, bias, and processing effects on vertical charge transport", *J Phys Chem C* **2008**, 112, 7922.

[109] S. K. Hau, H. L. Yip, J. Y. Zou, A. K. Y. Jen, "Indium tin oxide-free semi-transparent inverted polymer solar cells using conducting polymer as both bottom and top electrodes", *Org Electron* **2009**, 10, 1401.

[110] M. P. de Jong, L. J. van IJzendoorn, M. J. A. de Voigt, "Stability of the interface between indium-tin-oxide and poly(3,4-ethylenedioxythiophene)/poly(styrenesulfonate) in polymer light-emitting diodes", *Appl Phys Lett* **2000**, 77, 2255.

[111] M. Jorgensen, K. Norrman, F. C. Krebs, "Stability/degradation of polymer solar cells", *Sol Energ Mat Sol C* **2008**, 92, 686.

[112] F. So, D. Kondakov, "Degradation Mechanisms in Small-Molecule and Polymer Organic Light-Emitting Diodes", *Adv Mater* **2010**, 22, 3762.

[113] E. Voroshazi, B. Verreet, T. Aernouts, P. Heremans, "Long-term operational lifetime and degradation analysis of P3HT: PCBM photovoltaic cells", *Sol Energ Mat Sol C* **2011**, 95, 1303.

[114] M. Jorgensen, K. Norrman, S. A. Gevorgyan, T. Tromholt, B. Andreasen, F. C. Krebs, "Stability of Polymer Solar Cells", *Adv Mater* **2012**, 24, 580.

[115] G. Li, C. W. Chu, V. Shrotriya, J. Huang, Y. Yang, "Efficient inverted polymer solar cells", *Appl Phys Lett* **2006**, 88, 253503.

[116] J. Meyer, S. Hamwi, T. Bulow, H. H. Johannes, T. Riedl, W. Kowalsky, "Highly efficient simplified organic light emitting diodes", *Appl Phys Lett* **2007**, 91, 113506

[117] M. Kroger, S. Hamwi, J. Meyer, T. Riedl, W. Kowalsky, A. Kahn, "Role of the deep-lying electronic states of MoO3 in the enhancement of hole-injection in organic thin films", *Appl Phys Lett* **2009**, 95, 123301.

[118] H. Schmidt, H. Flugge, T. Winkler, T. Bulow, T. Riedl, W. Kowalsky, "Efficient semitransparent inverted organic solar cells with indium tin oxide top electrode", *Appl Phys Lett* **2009**, 94, 243302

[119] J. Meyer, K. Zilberberg, T. Riedl, A. Kahn, "Electronic structure of Vanadium pentoxide: An efficient hole injector for organic electronic materials", *J Appl Phys* **2011**, 110, 033710.

[120] K. Kanai, K. Koizumi, S. Ouchi, Y. Tsukamoto, K. Sakanoue, Y. Ouchi, K. Seki, "Electronic structure of anode interface with molybdenum oxide buffer layer", *Org Electron* **2010**, 11, 188.

[121] T. S. Sian, G. B. Reddy, "Optical, structural and photoelectron spectroscopic studies on amorphous and crystalline molybdenum oxide thin films", *Sol Energ Mat Sol C* **2004**, 82, 375.

[122] S. Hamwi, J. Meyer, M. Kroger, T. Winkler, M. Witte, T. Riedl, A. Kahn, W. Kowalsky, "The Role of Transition Metal Oxides in Charge-Generation Layers for Stacked Organic Light-Emitting Diodes", *Adv Funct Mater* **2010**, 20, 1762.

[123] H. Lee, S. W. Cho, K. Han, P. E. Jeon, C. N. Whang, K. Jeong, K. Cho, Y. Yi, "The origin of the hole injection improvements at indium tin oxide/molybdenum trioxide/N,N '-bis(1-naphthyl)-N,N '-diphenyl-1,1 '-biphenyl-4,4 '-diamine interfaces", *Appl Phys Lett* **2008**, 93, 043308.

[124] M. Sessolo, H. J. Bolink, "Hybrid Organic-Inorganic Light-Emitting Diodes", *Adv Mater* **2011**, 23, 1829.

[125] K. H. Wong, K. Ananthanarayanan, J. Luther, P. Balaya, "Origin of Hole Selectivity and the Role of Defects in Low-Temperature Solution-Processed Molybdenum Oxide Interfacial Layer for Organic Solar Cells", *J Phys Chem C* **2012**, 116, 16346.

[126] F. Xie, W. C. Choy, C. Wang, X. Li, S. Zhang, J. Hou, "Low-temperature solution-processed hydrogen molybdenum and vanadium bronzes for an efficient hole-transport layer in organic electronics", *Adv Mater* **2013**, 25, 2051.

[127] Irfan, M. L. Zhang, H. J. Ding, C. W. Tang, Y. L. Gao, "Strong interface p-doping and band bending in C-60 on MoOx", *Org Electron* **2011**, 12, 1588.

[128] T. Mayer, C. Hein, E. Mankel, W. Jaegermann, M. M. Muller, H. J. Kleebe, "Fermi level positioning in organic semiconductor phase mixed composites: The internal interface charge transfer doping model", *Org Electron* **2012**, 13, 1356.

[129] S. Hamwi, J. Meyer, T. Winkler, T. Riedl, W. Kowalsky, "p-type doping efficiency of MoO3 in organic hole transport materials", *Appl Phys Lett* **2009**, 94, 253307.

[130] C. P. Chen, Y. D. Chen, S. C. Chuang, "High-Performance and Highly Durable Inverted Organic Photovoltaics Embedding Solution-Processable Vanadium Oxides as an Interfacial Hole-Transporting Layer", *Adv Mater* **2011**, 23, 3859.

[131] J. Meyer, R. Khalandovsky, P. Gorrn, A. Kahn, "MoO3 Films Spin-Coated from a Nanoparticle Suspension for Efficient Hole-Injection in Organic Electronics", *Adv Mater* **2011**, 23, 70.

[132] J. H. Huang, T. Y. Huang, H. Y. Wei, K. C. Ho, C. W. Chu, "Wet-milled transition metal oxide nanoparticles as buffer layers for bulk heterojunction solar cells", *Rsc Adv* **2012**, 2, 7487.

[133] M. F. Xu, L. S. Cui, X. Z. Zhu, C. H. Gao, X. B. Shi, Z. M. Jin, Z. K. Wang, L. S. Liao, "Aqueous solution-processed MoO3 as an effective interfacial layer in polymer/fullerene based organic solar cells", *Org Electron* **2013**, 14, 657.

[134] J. S. Huang, C. Y. Chou, M. Y. Liu, K. H. Tsai, W. H. Lin, C. F. Lin, "Solution-processed vanadium oxide as an anode interlayer for inverted polymer solar cells hybridized with ZnO nanorods", *Org Electron* **2009**, 10, 1060.

[135] J. S. Huang, C. Y. Chou, C. F. Lin, "Efficient and Air-Stable Polymer Photovoltaic Devices With WO3-V2O5 Mixed Oxides as Anodic Modification", *Ieee Electr Device L* **2010**, 31, 332.

[136] N. Li, T. Stubhan, N. A. Luechinger, S. C. Halim, G. J. Matt, T. Ameri, C. J. Brabec, "Inverted structure organic photovoltaic devices employing a low temperature solution processed WO3 anode buffer layer", *Org Electron* **2012**, 13, 2479.

[137] T. Stubhan, N. Li, N. A. Luechinger, S. C. Halim, G. J. Matt, C. J. Brabec, "High Fill Factor Polymer Solar Cells Incorporating a Low Temperature Solution Processed WO3 Hole Extraction Layer", *Adv Energy Mater* **2012**, 2, 1433.

[138] D. C. Lim, Y. T. Kim, W. H. Shim, A. Y. Jang, J. H. Lim, Y. Do Kim, Y. Jeong, Y. D. Kim, K. H. Lee, "Wet-Chemically Prepared NiO Layers as Hole Transport Layer in the Inverted Organic Solar Cell", *B Korean Chem Soc* **2011**, 32, 1067.

[139] F. M. Liu, S. Y. Shao, X. Y. Guo, Y. Zhao, Z. Y. Xie, "Efficient polymer photovoltaic cells using solution-processed MoO3 as anode buffer layer", *Sol Energ Mat Sol C* **2010**, 94, 842.

[140] S. Y. Shao, J. Liu, J. Bergqvist, S. W. Shi, C. Veit, U. Wurfel, Z. Y. Xie, F. L. Zhang, "In Situ Formation of MoO3 in PEDOT:PSS Matrix: A Facile Way to Produce a Smooth and Less Hygroscopic Hole Transport Layer for Highly Stable Polymer Bulk Heterojunction Solar Cells", *Adv Energy Mater* **2013**, 3, 349.

[141] S. Murase, Y. Yang, "Solution Processed MoO3 Interfacial Layer for Organic Photovoltaics Prepared by a Facile Synthesis Method", *Adv Mater* **2012**, 24, 2459.

[142] C. Girotto, E. Voroshazi, D. Cheyns, P. Heremans, B. P. Rand, "Solution-Processed MoO3 Thin Films As a Hole-Injection Layer for Organic Solar Cells", *ACS applied materials & interfaces* **2011**, 3, 3244.

[143] T. B. Yang, M. Wang, Y. Cao, F. Huang, L. Huang, J. B. Peng, X. Gong, S. Z. D. Cheng, Y. Cao, "Polymer Solar Cells with a Low-Temperature-Annealed Sol-Gel-Derived MoOx Film as a Hole Extraction Layer", *Adv Energy Mater* **2012**, 2, 523.

[144] M. Benmouss, A. Outzourhit, R. Jourdani, A. Bennouna, E. L. Ameziane, "Structural, Optical and Electrochromic Properties of Sol–Gel V2O5 Thin Films", *Active and Passive Electronic Components* **2003**, 26, 245.

[145] N. Ozer, "Optical and electrochemical characteristics of sol-gel deposited tungsten oxide films: a comparison", *Thin Solid Films* **1997**, 304, 310.

[146] N. Ozer, "Electrochemical properties of sol-gel deposited vanadium pentoxide films", *Thin Solid Films* **1997**, 305, 80.

[147] N. Ozer, C. M. Lampert, "Electrochromic characterization of sol-gel deposited coatings", *Sol Energ Mat Sol C* **1998**, 54, 147.

[148] N. Ozer, C. M. Lampert, "Electrochromic performance of sol-gel deposited WO3-V2O5 films", *Thin Solid Films* **1999**, 349, 205.

[149] J. P. Cronin, D. J. Tarico, J. C. L. Tonazzi, A. Agrawal, S. R. Kennedy, "Microstructure and Properties of Sol-Gel Deposited Wo3 Coatings for Large-Area Electrochromic Windows", *Sol Energ Mat Sol C* **1993**, 29, 371.

[150] H. Unuma, K. Tonooka, Y. Suzuki, T. Furusaki, K. Kodaira, T. Matsushita, "Preparation of Transparent Amorphous Tungsten Trioxide Thin-Films by a Dip-Coating Method", *J Mater Sci Lett* **1986**, 5, 1248.

[151] O. Pyper, R. Schollhorn, J. J. T. M. Donkers, L. H. M. Krings, "Nanocrystalline structure of WO3 thin films prepared by the sol-gel technique", *Mater Res Bull* **1998**, 33, 1095.

[152] K. Galatsis, Y. X. Li, W. Wlodarski, E. Comini, G. Faglia, G. Sberveglieri, "Semiconductor MoO3-TiO2 thin film gas sensors", *Sensor Actuat B-Chem* **2001**, 77, 472.

[153] K. Galatsis, Y. X. Li, W. Wlodarski, K. Kalantar-zadeh, "Sol-gel prepared MoO3-WO3 thin-films for O-2 gas sensing", *Sensor Actuat B-Chem* **2001**, 77, 478.

[154] K. Galatsis, Y. X. Li, W. Wlodarski, E. Comini, G. Sberveglieri, C. Cantalini, S. Santucci, M. Passacantando, "Comparison of single and binary oxide MoO3, TiO2 and WO3 sol-gel gas sensors", *Sensor Actuat B-Chem* **2002**, 83, 276.

[155] N. N. Mallikarjuna, A. Venkataraman, "Synthesis of molybdenum oxide by thermal decomposition of molybdenum acetylacetonate sol-gel", *J Therm Anal Calorim* **2002**, 68, 901.

[156] K. Galatsis, Y. Li, W. Wlodarski, C. Cantalini, M. Passacantando, S. Santucci, "MoO3, WO3 single and binary oxide prepared by sol-gel method for gas sensing applications", *J Sol-Gel Sci Techn* **2003**, 26, 1097.

[157] T. M. McEvoy, K. J. Stevenson, "Electrochemical quartz crystal microbalance study of the electrodeposition mechanism of molybdenum oxide thin films from peroxo-polymolybdate solution", *Anal Chim Acta* **2003**, 496, 39.

[158] T. M. McEvoy, K. J. Stevenson, J. T. Hupp, X. J. Dang, "Electrochemical preparation of molybdenum trioxide thin films: Effect of sintering on electrochromic and electroinsertion properties", *Langmuir : the ACS journal of surfaces and colloids* **2003**, 19, 4316.

[159] J. B. Sun, R. Xiong, S. M. Wang, W. F. Tang, H. Tong, J. Shi, "Preparation and characterization of molybdenum oxide thin films by sol-gel process", *J Sol-Gel Sci Techn* **2003**, 27, 315.

[160] L. Boudaoud, N. Benramdane, R. Desfeux, B. Khelifa, C. Mathieu, "Structural and optical properties Of MoO3 andV(2)O(5) thin films prepared by Spray Pyrolysis", *Catal Today* **2006**, 113, 230.

[161] C. S. Hsu, C. C. Chan, H. T. Huang, C. H. Peng, W. C. Hsu, "Electrochromic properties of nanocrystalline MoO3 thin films", *Thin Solid Films* **2008**, 516, 4839.

[162] M. B. Sahana, C. Sudakar, C. Thapa, G. Lawes, V. M. Naik, R. J. Baird, G. W. Auner, R. Naik, K. R. Padmanabhan, "Electrochemical propertiesOf V2O5 thin films deposited by spin coating", *Mat Sci Eng B-Solid* **2007**, 143, 42.

[163] J. J. Jasieniak, J. Seifter, J. Jo, T. Mates, A. J. Heeger, "A Solution-Processed MoOx Anode Interlayer for Use within Organic Photovoltaic Devices", *Adv Funct Mater* **2012**, 22, 2594.

[164] S. Höfle, H. Do, E. Mankel, M. Pfaff, Z. Zhang, D. Bahro, T. Mayer, W. Jaegermann, D. Gerthsen, C. Feldmann, U. Lemmer, A. Colsmann, "Molybdenum oxide anode buffer layers for solution processed, blue phosphorescent small molecule organic light emitting diodes", *Org Electron* **2013**, 14, 1820.

[165] Z. A. Tan, W. Q. Zhang, C. H. Cui, Y. Q. Ding, D. P. Qian, Q. Xu, L. J. Li, S. S. Li, Y. F. Li, "Solution-processed vanadium oxide as a hole collection layer on an ITO electrode for high-performance polymer solar cells", *Phys Chem Chem Phys* **2012**, 14, 14589.

[166] Z. A. Tan, L. J. Li, C. H. Cui, Y. Q. Ding, Q. Xu, S. S. Li, D. P. Qian, Y. F. Li, "Solution-Processed Tungsten Oxide as an Effective Anode Buffer Layer for High-Performance Polymer Solar Cells", *J Phys Chem C* **2012**, 116, 18626.

[167] X. Orignac, H. C. Vasconcelos, X. M. Du, R. M. Almeida, "Influence of solvent concentration on the microstructure of SiO2-TiO2 sol-gel films", *J Sol-Gel Sci Techn* **1997**, 8, 243.

[168] J. L. K. A. Cappellani, N. P. Barradas, S. M. Jackson, "Processing and characterization of sol-gel deposited Ta2O5 and TiO2-Ta2O5 dielectric films", *Solid-State Electron.* **1999**, 43, 1095.

[169] M. Demeter, M. Neumann, W. Reichelt, "Mixed-valence vanadium oxides studied by XPS", *Surf Sci* **2000**, 454, 41.

[170] A. Talledo, C. G. Granqvist, "Electrochromic Vanadium-Pentoxide-Based Films - Structural, Electrochemical, and Optical-Properties", *J Appl Phys* **1995**, 77, 4655.

[171] C. G. Granqvist, "Electrochromic Oxides - a Unified View", *Solid State Ionics* **1994**, 70, 678.

[172] Q. H. Wu, A. Thissen, W. Jaegermann, "Photoelectron spectroscopic study of Na intercalation into V2O5 thin films", *Solid State Ionics* **2004**, 167, 155.

[173] H. M. Zhang, W. C. H. Choy, "Indium tin oxide modified by Au and vanadium pentoxide as an efficient anode for organic light-emitting devices", *Ieee T Electron Dev* **2008**, 55, 2517.

[174] M. G. Helander, Z. B. Wang, M. T. Greiner, J. Qiu, Z. H. Lu, "Substrate dependent charge injection at the V2O5/organic interface", *Appl Phys Lett* **2009**, 95, 083301

[175] C. Sanchez, M. Henry, J. C. Grenet, J. Livage, "Free and Bound Polarons in Vanadium Pentoxide", *J Phys C Solid State* **1982**, 15, 7133.

[176] J. C. Badot, A. Mantoux, N. Baffier, O. Dubrunfaut, D. Lincot, "Electrical properties of V2O5 thin films obtained by atomic layer deposition (ALD)", *J Mater Chem* **2004**, 14, 3411.

[177] J. Tauc, "Optical properties of solids", *Amsterdam* **1972**.

[178] G. A. Khan, C. A. Hogarth, "Optical-Absorption Spectra of Evaporated V2o5 and Coevaporated V2o5/B2o3 Thin-Films", *J Mater Sci* **1991**, 26, 412.

[179] V. Shrotriya, G. Li, Y. Yao, C. W. Chu, Y. Yang, "Transition metal oxides as the buffer layer for polymer photovoltaic cells", *Appl Phys Lett* **2006**, 88, 073508.

[180] J. Meyer, A. Shu, M. Kroger, A. Kahn, "Effect of contamination on the electronic structure and hole-injection properties of MoO3/organic semiconductor interfaces", *Appl Phys Lett* **2010**, 96, 133308

[181] S. R. Hammond, J. Meyer, N. E. Widjonarko, P. F. Ndione, A. K. Sigdel, A. Garcia, A. Miedaner, M. T. Lloyd, A. Kahn, D. S. Ginley, J. J. Berry, D. C. Olson, "Low-temperature, solution-processed molybdenum oxide hole-collection layer for organic photovoltaics", *J Mater Chem* **2012**, 22, 3249.

[182] Irfan, H. J. Ding, Y. L. Gao, C. Small, D. Y. Kim, J. Subbiah, F. So, "Energy level evolution of air and oxygen exposed molybdenum trioxide films", *Appl Phys Lett* **2010**, 96, 243307.

[183] M. A. Quevedo-Lopez, R. F. Reidy, R. A. Orozco-Teran, O. Mendoza-Gonzalez, R. Ramirez-Bon, "Enhancement of the photochromic and thermochromic properties of molybdenum oxide thin films by a cadmium sulfide underlayer", *J Mater Sci-Mater El* **2000**, 11, 151.

[184] K. Y. Li, D. F. Xue, "Estimation of electronegativity values of elements in different valence states", *Journal of Physical Chemistry A* **2006**, 110, 11332.

[185] C. G. Granqvist, "Progress in electrochromics: tungsten oxide revisited", *Electrochim Acta* **1999**, 44, 3005.

[186] M. T. Greiner, M. G. Helander, Z. B. Wang, W. M. Tang, J. Qiu, Z. H. Lu, "A metallic molybdenum suboxide buffer layer for organic electronic devices", *Appl Phys Lett* **2010**, 96, 213302

[187] A. Corma, H. Garcia, "Lewis acids as catalysts in oxidation reactions: From homogeneous to heterogeneous systems", *Chem Rev* **2002**, 102, 3837.

[188] T. Rabe, P. Gorrn, M. Lehnhardt, M. Tilgner, T. Riedl, W. Kowalsky, "Highly Sensitive Determination of the Polaron-Induced Optical Absorption of Organic Charge-Transport Materials", *Physical review letters* **2009**, 102, 137401.

[189] M. Lehnhardt, S. Hamwi, M. Hoping, J. Reinker, T. Riedl, W. Kowalsky, "Charge carrier densities in chemically doped organic semiconductors verified by two independent techniques", *Appl Phys Lett* **2010**, 96, 193301.

[190] V. A. Trukhanov, V. V. Bruevich, D. Y. Paraschuk, "Effect of doping on performance of organic solar cells", *Phys Rev B* **2011**, 84, 205318.

[191] U. Schubert, "Organically modified transition metal alkoxides: Chemical problems and structural issues on the way to materials syntheses", *Accounts Chem Res* **2007**, 40, 730.

[192] C. Waldauf, M. Morana, P. Denk, P. Schilinsky, K. Coakley, S. A. Choulis, C. J. Brabec, "Highly efficient inverted organic photovoltaics using solution based titanium oxide as electron selective contact", *Appl Phys Lett* **2006**, 89, 233517.

[193] H. Schmidt, K. Zilberberg, S. Schmale, H. Flugge, T. Riedl, W. Kowalsky, "Transient characteristics of inverted polymer solar cells using titaniumoxide interlayers", *Appl Phys Lett* **2010**, 96, 243305.

[194] M. S. White, D. C. Olson, S. E. Shaheen, N. Kopidakis, D. S. Ginley, "Inverted bulk-heterojunction organic photovoltaic device using a solution-derived ZnO underlayer", *Appl Phys Lett* **2006**, 89, 143517.

[195] J. Huang, Z. G. Yin, Q. D. Zheng, "Applications of ZnO in organic and hybrid solar cells", *Energ Environ Sci* **2011**, 4, 3861.

[196] R. Sondergaard, M. Helgesen, M. Jorgensen, F. C. Krebs, "Fabrication of Polymer Solar Cells Using Aqueous Processing for All Layers Including the Metal Back Electrode", *Adv Energy Mater* **2011**, 1, 68.

[197] Y. M. Sun, J. H. Seo, C. J. Takacs, J. Seifter, A. J. Heeger, "Inverted Polymer Solar Cells Integrated with a Low-Temperature-Annealed Sol-Gel-Derived ZnO Film as an Electron Transport Layer", *Adv Mater* **2011**, 23, 1679.

[198] T. Stubhan, H. Oh, L. Pinna, J. Krantz, I. Litzov, C. J. Brabec, "Inverted organic solar cells using a solution processed aluminum-doped zinc oxide buffer layer", *Org Electron* **2011**, 12, 1539.

[199] S. Trost, K. Zilberberg, A. Behrendt, T. Riedl, "Room-temperature solution processed SnOx as an electron extraction layer for inverted organic solar cells with superior thermal stability", *J Mater Chem* **2012**, 22, 16224.

[200] Y. H. Zhou, F. H. Li, S. Barrau, W. J. Tian, O. Inganas, F. L. Zhang, "Inverted and transparent polymer solar cells prepared with vacuum-free processing", *Sol Energ Mat Sol C* **2009**, 93, 497.

[201] H. Kang, S. Hong, J. Lee, K. Lee, "Electrostatically Self-Assembled Nonconjugated Polyelectrolytes as an Ideal Interfacial Layer for Inverted Polymer Solar Cells", *Adv Mater* **2012**, 24, 3005.

[202] Y. H. Zhou, C. Fuentes-Hernandez, J. Shim, J. Meyer, A. J. Giordano, H. Li, P. Winget, T. Papadopoulos, H. Cheun, J. Kim, M. Fenoll, A. Dindar, W. Haske, E. Najafabadi, T. M. Khan, H. Sojoudi, S. Barlow, S. Graham, J. L. Bredas, S. R. Marder, A. Kahn, B. Kippelen, "A Universal Method to Produce Low-Work Function Electrodes for Organic Electronics", *Science* **2012**, 336, 327.

[203] J. W. Shim, H. Cheun, J. Meyer, C. Fuentes-Hernandez, A. Dindar, Y. H. Zhou, D. K. Hwang, A. Kahn, B. Kippelen, "Polyvinylpyrrolidone-modified indium tin oxide as an electron-collecting electrode for inverted polymer solar cells", *Appl Phys Lett* **2012**, 101, 073303.

[204] Z. Tang, L. M. Andersson, Z. George, K. Vandewal, K. Tvingstedt, P. Heriksson, R. Kroon, M. R. Andersson, O. Inganas, "Interlayer for Modified Cathode in Highly Efficient Inverted ITO-Free Organic Solar Cells", *Adv Mater* **2012**, 24, 554.

[205] Z. C. He, C. M. Zhong, X. Huang, W. Y. Wong, H. B. Wu, L. W. Chen, S. J. Su, Y. Cao, "Simultaneous Enhancement of Open-Circuit Voltage, Short-Circuit Current Density, and Fill Factor in Polymer Solar Cells", *Adv Mater* **2011**, 23, 4636.

[206] Z. C. He, C. M. Zhong, S. J. Su, M. Xu, H. B. Wu, Y. Cao, "Enhanced power-conversion efficiency in polymer solar cells using an inverted device structure", *Nat Photonics* **2012**, 6, 591.

[207] H. Choi, J. S. Park, E. Jeong, G. H. Kim, B. R. Lee, S. O. Kim, M. H. Song, H. Y. Woo, J. Y. Kim, "Combination of Titanium Oxide and a Conjugated Polyelectrolyte for High-Performance Inverted-Type Organic Optoelectronic Devices", *Adv Mater* **2011**, 23, 2759.

[208] T. B. Yang, M. Wang, C. H. Duan, X. W. Hu, L. Huang, J. B. Peng, F. Huang, X. Gong, "Inverted polymer solar cells with 8.4% efficiency by conjugated polyelectrolyte", *Energ Environ Sci* **2012**, 5, 8208.

[209] J. Dupont, P. A. Z. Suarez, "Physico-chemical processes in imidazolium ionic liquids", *Phys Chem Chem Phys* **2006**, 8, 2441.

[210] J. Kim, G. Kim, Y. Choi, J. Lee, S. H. Park, K. Lee, "Light-soaking issue in polymer solar cells: Photoinduced energy level alignment at the sol-gel processed metal oxide and indium tin oxide interface", *J Appl Phys* **2012**, 111, 114511.

[211] R. Steim, S. A. Choulis, P. Schilinsky, C. J. Brabec, "Interface modification for highly efficient organic photovoltaics", *Appl Phys Lett* **2008**, 92, 093303

[212] C. S. Kim, S. S. Lee, E. D. Gomez, J. B. Kim, Y. L. Loo, "Transient photovoltaic behavior of air-stable, inverted organic solar cells with solution-processed electron transport layer", *Appl Phys Lett* **2009**, 94, 113302.

[213] M. R. Lilliedal, A. J. Medford, M. V. Madsen, K. Norrman, F. C. Krebs, "The effect of post-processing treatments on inflection points in current-voltage curves of roll-to-roll processed polymer photovoltaics", *Sol Energ Mat Sol C* **2010**, 94, 2018.

[214] J. Gilot, M. M. Wienk, R. A. J. Janssen, "Double and triple junction polymer solar cells processed from solution", *Appl Phys Lett* **2007**, 90, 143512.

[215] J. C. Wang, C. Y. Lu, J. L. Hsu, M. K. Lee, Y. R. Hong, T. P. Perng, S. F. Horng, H. F. Meng, "Efficient inverted organic solar cells without an electron selective layer", *J Mater Chem* **2011**, 21, 5723.

[216] Y. H. Zhou, J. W. Shim, C. Fuentes-Hernandez, A. Sharma, K. A. Knauer, A. J. Giordano, S. R. Marder, B. Kippelen, "Direct correlation between work function of indium-tin-oxide electrodes and solar cell performance influenced by ultraviolet irradiation and air exposure", *Phys Chem Chem Phys* **2012**, 14, 12014.

[217] C. Y. Li, T. C. Wen, T. H. Lee, T. F. Guo, J. C. A. Huang, Y. C. Lin, Y. J. Hsu, "An inverted polymer photovoltaic cell with increased air stability obtained by employing novel hole/electron collecting layers", *J Mater Chem* **2009**, 19, 1643.

[218] H. Li, P. Paramonov, J. L. Bredas, "Theoretical study of the surface modification of indium tin oxide with trifluorophenyl phosphonic acid molecules: impact of coverage density and binding geometry", *J Mater Chem* **2010**, 20, 2630.

[219] W. Osikowicz, X. Crispin, C. Tengstedt, L. Lindell, T. Kugler, W. R. Salaneck, "Transparent low-work-function indium tin oxide electrode obtained by molecular scale interface engineering", *Appl Phys Lett* **2004**, 85, 1616.

[220] O. T. Hofmann, J. C. Deinert, Y. Xu, P. Rinke, J. Stahler, M. Wolf, M. Scheffler, "Large work function reduction by adsorption of a molecule with a negative electron affinity: Pyridine on ZnO(10(1)over-bar0)", *Journal of Chemical Physics* **2013**, 139, 174701.

[221] G. Ashkenasy, D. Cahen, R. Cohen, A. Shanzer, A. Vilan, "Molecular engineering of semiconductor surfaces and devices", *Accounts Chem Res* **2002**, 35, 121.

[222] V. S. L'vov, R. Naaman, V. Tiberkevich, Z. Vager, "Cooperative effect in electron transfer between metal substrate and organized organic layers", *Chem Phys Lett* **2003**, 381, 650.

[223] A. Natan, Y. Zidon, Y. Shapira, L. Kronik, "Cooperative effects and dipole formation at semiconductor and self-assembled-monolayer interfaces", *Phys Rev B* **2006**, 73, 193310.

[224] D. Cornil, Y. Olivier, V. Geskin, J. Cornil, "Depolarization effects in self-assembled monolayers: A quantum-chemical insight", *Adv Funct Mater* **2007**, 17, 1143.

[225] A. Natan, L. Kronik, H. Haick, R. T. Tung, "Electrostatic properties of ideal and non-ideal polar organic monolayers: Implications for electronic devices", *Adv Mater* **2007**, 19, 4103.

[226] L. Romaner, G. Heimel, C. Ambrosch-Draxl, E. Zojer, "The Dielectric Constant of Self-Assembled Monolayers", *Adv Funct Mater* **2008**, 18, 3999.

[227] T. Van Regemorter, M. Guillaume, A. Fuchs, C. Lennartz, V. Geskin, D. Beljonne, J. Cornil, "Methodological aspects of the quantum-chemical description of interface dipoles at tetrathiafulvalene/tetracyanoquinodimethane interfaces", *Journal of Chemical Physics* **2012**, 137, 174708.

[228] G. Heimel, L. Romaner, E. Zojer, J. L. Bredas, "The interface energetics of self-assembled monolayers on metals", *Accounts Chem Res* **2008**, 41, 721.

[229] A. Kahn, N. Koch, W. Y. Gao, "Electronic structure and electrical properties of interfaces between metals and pi-conjugated molecular films", *J Polym Sci Pol Phys* **2003**, 41, 2529.

[230] F. Nuesch, K. Kamaras, L. Zuppiroli, "Protonated metal-oxide electrodes for organic light emitting diodes", *Chem Phys Lett* **1998**, 283, 194.

[231] A. J. Medford, M. R. Lilliedal, M. Jorgensen, D. Aaro, H. Pakalski, J. Fyenbo, F. C. Krebs, "Grid-connected polymer solar panels: initial considerations of cost, lifetime, and practicality", *Opt Express* **2010**, 18, A272.

[232] H. Jin, C. Tao, M. Velusamy, M. Aljada, Y. L. Zhang, M. Hambsch, P. L. Burn, P. Meredith, "Efficient, Large Area ITO-and-PEDOT-free Organic Solar Cell Sub-modules", *Adv Mater* **2012**, 24, 2572.

[233] H. Schmidt, T. Winkler, I. Baumann, S. Schmale, H. Flugge, H. H. Johannes, S. Hamwi, T. Rabe, T. Riedl, W. Kowalsky, "Indium-free bottom electrodes for inverted organic solar cells with simplified cell architectures", *Appl Phys Lett* **2011**, 99, 033304.

[234] J. B. Wu, M. Agrawal, H. A. Becerril, Z. N. Bao, Z. F. Liu, Y. S. Chen, P. Peumans, "Organic Light-Emitting Diodes on Solution-Processed Graphene Transparent Electrodes", *Acs Nano* **2010**, 4, 43.

[235] Z. Y. Yin, S. Y. Sun, T. Salim, S. X. Wu, X. A. Huang, Q. Y. He, Y. M. Lam, H. Zhang, "Organic Photovoltaic Devices Using Highly Flexible Reduced Graphene Oxide Films as Transparent Electrodes", *Acs Nano* **2010**, 4, 5263.

[236] C. Y. Li, Z. Li, H. W. Zhu, K. L. Wang, J. Q. Wei, X. A. Li, P. Z. Sun, H. Zhang, D. H. Wu, "Graphene Nano-"patches" on a Carbon Nanotube Network for Highly Transparent/Conductive Thin Film Applications", *J Phys Chem C* **2010**, 114, 14008.

[237] Z. C. Wu, Z. H. Chen, X. Du, J. M. Logan, J. Sippel, M. Nikolou, K. Kamaras, J. R. Reynolds, D. B. Tanner, A. F. Hebard, A. G. Rinzler, "Transparent, conductive carbon nanotube films", *Science* **2004**, 305, 1273.

[238] D. H. Zhang, K. Ryu, X. L. Liu, E. Polikarpov, J. Ly, M. E. Tompson, C. W. Zhou, "Transparent, conductive, and flexible carbon nanotube films and their application in organic light-emitting diodes", *Nano Lett* **2006**, 6, 1880.

[239] L. B. Hu, H. Wu, Y. Cui, "Metal nanogrids, nanowires, and nanofibers for transparent electrodes", *Mrs Bull* **2011**, 36, 760.

[240] L. B. Hu, H. S. Kim, J. Y. Lee, P. Peumans, Y. Cui, "Scalable Coating and Properties of Transparent, Flexible, Silver Nanowire Electrodes", *Acs Nano* **2010**, 4, 2955.

[241] S. M. Bergin, Y. H. Chen, A. R. Rathmell, P. Charbonneau, Z. Y. Li, B. J. Wiley, "The effect of nanowire length and diameter on the properties of transparent, conducting nanowire films", *Nanoscale* **2012**, 4, 1996.

[242] J. Y. Lee, S. T. Connor, Y. Cui, P. Peumans, "Solution-processed metal nanowire mesh transparent electrodes", *Nano Lett* **2008**, 8, 689.

[243] J. Krantz, M. Richter, S. Spallek, E. Spiecker, C. J. Brabec, "Solution-Processed Metallic Nanowire Electrodes as Indium Tin Oxide Replacement for Thin-Film Solar Cells", *Adv Funct Mater* **2011**, 21, 4784.

[244] D. S. Leem, A. Edwards, M. Faist, J. Nelson, D. D. C. Bradley, J. C. de Mello, "Efficient Organic Solar Cells with Solution-Processed Silver Nanowire Electrodes", *Adv Mater* **2011**, 23, 4371.

[245] J. Krantz, T. Stubhan, M. Richter, S. Spallek, I. Litzov, G. J. Matt, E. Spiecker, C. J. Brabec, "Spray-Coated Silver Nanowires as Top Electrode Layer in Semitransparent P3HT:PCBM-Based Organic Solar Cell Devices", *Adv Funct Mater* **2013**, 23, 1711.

[246] R. Zhu, C. H. Chung, K. C. Cha, W. B. Yang, Y. B. Zheng, H. P. Zhou, T. B. Song, C. C. Chen, P. S. Weiss, G. Li, Y. Yang, "Fused Silver Nanowires with Metal Oxide Nanoparticles and Organic Polymers for Highly Transparent Conductors", *Acs Nano* **2011**, 5, 9877.

[247] F. S. F. Morgenstern, D. Kabra, S. Massip, T. J. K. Brenner, P. E. Lyons, J. N. Coleman, R. H. Friend, "Ag-nanowire films coated with ZnO nanoparticles as a transparent electrode for solar cells", *Appl Phys Lett* **2011**, 99, 183307.

[248] T. Stubhan, J. Krantz, N. Li, F. Guo, I. Litzov, M. Steidl, M. Richter, G. J. Matt, C. J. Brabec, "High fill factor polymer solar cells comprising a transparent, low temperature solution processed doped metal oxide/metal nanowire composite electrode", *Sol Energ Mat Sol C* **2012**, 107, 248.

[249] C. C. Chen, L. T. Dou, R. Zhu, C. H. Chung, T. B. Song, Y. B. Zheng, S. Hawks, G. Li, P. S. Weiss, Y. Yang, "Visibly Transparent Polymer Solar Cells Produced by Solution Processing", *Acs Nano* **2012**, 6, 7185.

[250] C. H. Chung, T. B. Song, B. Bob, R. Zhu, H. S. Duan, Y. Yang, "Silver Nanowire Composite Window Layers for Fully Solution-Deposited Thin-Film Photovoltaic Devices", *Adv Mater* **2012**, 24, 5499.

[251] D. Theirich, R. Muller, K. Zilberberg, S. Trost, A. Behrendt, T. Riedl, "Atmospheric Pressure Plasma ALD of Titanium Oxide", *Chem Vapor Depos* **2013**, 19, 167.

[252] S. F. Nelson, D. H. Levy, L. W. Tutt, M. Burberry, "Cycle time effects on growth and transistor characteristics of spatial atomic layer deposition of zinc oxide", *J Vac Sci Technol A* **2012**, 30, 01A154.

[253] E. Dickey, W. A. Barrow, "High rate roll to roll atomic layer deposition, and its application to moisture barriers on polymer films", *J Vac Sci Technol A* **2012**, 30, 021502

[254] L. Reimer, "Scanning microscopy, physics of image formation and microanalysis, Springer Berlin", *Springer Series in Optical Sciences* **1985**, 45.

[255] C. Thomas, I. Joachimsthaler, R. Heiderhoff, L. J. Balk, "Electron-beam-induced potentials in semiconductors: calculation and measurement with an SEM/SPM hybrid system", *J Phys D Appl Phys* **2004**, 37, 2785.

[256] J. Meyer, P. Gorrn, S. Hamwi, H. H. Johannes, T. Riedl, W. Kowalsky, "Indium-free transparent organic light emitting diodes with Al doped ZnO electrodes grown by atomic layer and pulsed laser deposition", *Appl Phys Lett* **2008**, 93, 073308.

[257] D. Zhang, C. Z. Wang, F. X. Zhang, "Effect of Substrate Temperature on the Crystallinity and Band Edge Luminescence of Zno Thin Films Deposited by Pulsed Laser Deposition", *Int J Mod Phys B* **2012**, 26, 1250161.

[258] J. Malm, E. Sahramo, J. Perala, T. Sajavaara, M. Karppinen, "Low-temperature atomic layer deposition of ZnO thin films: Control of crystallinity and orientation", *Thin Solid Films* **2011**, 519, 5319.

[259] K. Aslan, Z. Leonenko, J. R. Lakowicz, C. D. Geddes, "Annealed silver-island films for applications in metal-enhanced fluorescence: Interpretation in terms of radiating plasmons", *J Fluoresc* **2005**, 15, 643.

[260] S. De, T. M. Higgins, P. E. Lyons, E. M. Doherty, P. N. Nirmalraj, W. J. Blau, J. J. Boland, J. N. Coleman, "Silver Nanowire Networks as Flexible, Transparent, Conducting Films: Extremely High DC to Optical Conductivity Ratios", *Acs Nano* **2009**, 3, 1767.

[261] K. L. Kelly, E. Coronado, L. L. Zhao, G. C. Schatz, "The optical properties of metal nanoparticles: The influence of size, shape, and dielectric environment", *J Phys Chem B* **2003**, 107, 668.

[262] M. K. Kinnan, S. Kachan, C. K. Simmons, G. Chumanov, "Plasmon Coupling in Two-Dimensional Arrays of Silver Nanoparticles: I. Effect of the Dielectric Medium", *J Phys Chem C* **2009**, 113, 7079.

[263] M. Lenes, M. Morana, C. J. Brabec, P. W. M. Blom, "Recombination-Limited Photocurrents in Low Bandgap Polymer/Fullerene Solar Cells", *Adv Funct Mater* **2009**, 19, 1106.

[264] A. Maurano, R. Hamilton, C. G. Shuttle, A. M. Ballantyne, J. Nelson, B. O'Regan, W. M. Zhang, I. McCulloch, H. Azimi, M. Morana, C. J. Brabec, J. R. Durrant, "Recombination Dynamics as a Key Determinant of Open Circuit Voltage in Organic Bulk Heterojunction Solar Cells: A Comparison of Four Different Donor Polymers", *Adv Mater* **2010**, 22, 4987.

[265] J. K. Lee, W. L. Ma, C. J. Brabec, J. Yuen, J. S. Moon, J. Y. Kim, K. Lee, G. C. Bazan, A. J. Heeger, "Processing additives for improved efficiency from bulk heterojunction solar cells", *J Am Chem Soc* **2008**, 130, 3619.

[266] J. Peet, J. Y. Kim, N. E. Coates, W. L. Ma, D. Moses, A. J. Heeger, G. C. Bazan, "Efficiency enhancement in low-bandgap polymer solar cells by processing with alkane dithiols", *Nat Mater* **2007**, 6, 497.

[267] R. J. Kline, M. D. McGehee, E. N. Kadnikova, J. S. Liu, J. M. J. Frechet, M. F. Toney, "Dependence of regioregular poly(3-hexylthiophene) film morphology and field-effect mobility on molecular weight", *Macromolecules* **2005**, 38, 3312.

[268] T. Agostinelli, T. A. M. Ferenczi, E. Pires, S. Foster, A. Maurano, C. Muller, A. Ballantyne, M. Hampton, S. Lilliu, M. Campoy-Quiles, H. Azimi, M. Morana, D. D. C. Bradley, J. Durrant, J. E. Macdonald, N. Stingelin, J. Nelson, "The Role of Alkane Dithiols in Controlling Polymer Crystallization in Small Band Gap Polymer:Fullerene Solar Cells", *J Polym Sci Pol Phys* **2011**, 49, 717.

[269] J. Gilot, I. Barbu, M. M. Wienk, R. A. J. Janssen, "The use of ZnO as optical spacer in polymer solar cells: Theoretical and experimental study", *Appl Phys Lett* **2007**, 91, 113520.

[270] M. Y. Chan, S. L. Lai, K. M. Lau, C. S. Lee, S. T. Lee, "Application of metal-doped organic layer both as exciton blocker and optical spacer for organic photovoltaic devices", *Appl Phys Lett* **2006**, 89, 163515.

[271] A. K. K. Kyaw, D. H. Wang, D. Wynands, J. Zhang, T. Q. Nguyen, G. C. Bazan, A. J. Heeger, "Improved Light Harvesting and Improved Efficiency by Insertion of an Optical Spacer (ZnO) in Solution-Processed Small-Molecule Solar Cells", *Nano Lett* **2013**, 13, 3796.

[272] E. New, T. Howells, P. Sullivan, T. S. Jones, "Small molecule tandem organic photovoltaic cells incorporating an alpha-NPD optical spacer layer", *Org Electron* **2013**, 14, 2353.

[273] Y. L. Zhang, A. K. Pandey, C. Tao, Y. Fang, H. Jin, P. L. Burn, P. Meredith, "Spectral response tuning using an optical spacer in broad-band organic solar cells", *Appl Phys Lett* **2013**, 102, 013302.1.

[274] G. D. Sharma, M. L. Keshtov, A. R. Khokhlov, D. Tasis, C. Galiotis, "Improved power conversion efficiency by insertion of RGO-TiO2 composite layer as optical spacer in polymer bulk heterojunction solar cells", *Org Electron* **2014**, 15, 348.

[275] D. A. Shirley, "High-Resolution X-Ray Photoemission Spectrum of the Valence Bands of Gold", *Phys. Rev. B* **1972**, 5, 4709.

[276] M. Wojdyr, "Fityk: a general-purpose peak fitting program", *J Appl Crystallogr* **2010**, 43, 1126.

[277] J. H. Scofield, "Hartree-Slater Subshell Photoionization Cross-Sections at 1254 and 1487ev", *J Electron Spectrosc* **1976**, 8, 129.

[278] L. S. Roman, W. Mammo, L. A. A. Pettersson, M. R. Andersson, O. Inganas, "High quantum efficiency polythiophene/C-60 photodiodes", *Adv Mater* **1998**, 10, 774.

[279] H. Hoppe, N. Arnold, D. Meissner, N. S. Sariciftci, "Modeling of optical absorption in conjugated polymer/fullerene bulk-heterojunction plastic solar cells", *Thin Solid Films* **2004**, 451, 589.

8. Author's publications and conference contributions

- M. Kraft, S. Adamczyk, A. Polywka, K. Zilberberg, P. Görrn, T. Riedl, U. Scherf, Polyanionic, alkylthiosulfate-based thiol precursor for conjugated polymer self-assembly onto gold from polar solvents, *submitted*.
- K. Zilberberg, F. Gasse, R. Pagui, A. Polywka, P. Görrn, A. Behrendt, S. Trost, R. Heiderhoff, T. Riedl, Highly robust Indium-free transparent conductive electrodes based on composites of silver nanowires and conductive metal oxides, *Adv. Funct. Mater.* **2014**, 24, 1671-1678.
- K. Zilberberg, J. Meyer, T. Riedl, Solution processed metal-oxides for organic electronic devices, *J. Mater. Chem. C* **2013**, 1, 4796.
- S. Kowalski, S. Allard, K. Zilberberg, T. Riedl, U. Scherf, Direct arylation polycondensation as simplified alternative for the synthesis of conjugated (co)polymers, *Progress in polymer sci.* **2013**, 38, 1805-1814.
- S. Trost, K. Zilberberg, A. Behrendt, P. Reckers, T. Mayer, T. Riedl, Overcoming the „light-soaking" issue in inverted organic solar cells by the use of Al:ZnO electron extraction layers, *Adv. Energy Mater.* **2013**, 3, 11, 1437-1444.
- D. Theirich, R. Müller, K. Zilberberg, S. Trost, A. Behrendt, and T. Riedl, Atmospheric pressure plasma ALD of titanium oxide, *Chem. Vap. Deposition* **2013**, 19, 167-173.
- K. Zilberberg, A. Behrendt, U. Scherf, T. Riedl, Ultrathin interlayers of a conjugated polyelectrolyte for low work-function cathodes in efficient inverted organic solar cells, *Org. Electron.* **2013**, 14, 951-957.
- S. Trost, K. Zilberberg, A. Behrendt, T. Riedl, Room-temperature solution processed SnO_x as electron extraction layer for inverted organic solar cells with improved thermal stability, *J. Mater. Chem.* **2012**, 22, 16224-16229.
- K. Zilberberg, H. Gharbi, A. Behrendt, S. Trost, T. Riedl, Low-temperature solution-processed MoO_x for efficient and stable organic solar cells, *ACS Appl. Mater. Interfaces* **2012**, 4, 1164-1168.
- K. Zilberberg, S. Trost, J. Meyer, A. Kahn, A. Behrendt, D. Lützenkirchen-Hecht, R. Frahm, T. Riedl, Inverted organic solar cells with sol-gel processed high work-function vanadium oxide hole-extraction layers, *Adv. Funct. Mat.* **2011**, 21, 4776-4783.
- J. Meyer, K. Zilberberg , T. Riedl , A. Kahn, Electronic structure of Vanadium pentoxide: An efficient hole injector for organic electronic materials", *J. Appl. Phys.* **2011**, 110, 033710.
- K. Zilberberg, S. Trost, H. Schmidt and T. Riedl, Solution processed vanadium pentoxide as charge extraction layer for organic solar cells, *Adv. Energy Mat.* **2011**, 1, 377-381.

- H. Schmidt, K. Zilberberg, S. Schmale, H. Flügge, T. Riedl, W. Kowalsky, „Transient characteristics of inverted polymer solar cells using titanium oxide interlayers", *Appl. Phys. Lett.* **2010**, 96, 243305.

Conference contributions

- Behrendt, T. Gahlmann, M. Fakhri, S. Trost, K. Zilberberg, T. Riedl, Highly robust transparent conductive gas diffusion barriers based on tin oxide prepared by low-temperature atomic layer deposition, *MRS Fall* **2013**, M1.06, Boston.
- S. Kowalski, S. Allard, K. Zilberberg, T. Riedl, U. Scherf, Synthesis of Poly(4,4-dialkyl-cyclopenta[2,1-b:3,4-b']-dithiophene-alt-2,1,3-benzothiadiazole) (PCPDTBT) in a direct arylation scheme, *Molekulares Kolloquium* **2013**, (Poster) 15, Freiburg.
- K. Zilberberg, F. Gasse, R. Pagui, A. Behrendt, S. Trost, R. Heiderhoff, T. Riedl, A hybrid approach for highly conductive and transparent coatings based on composites of silver nanowires and conductive metal oxides, *MRS Fall* **2012**, F1.05, Boston.
- D. Theirich, R. Mueller, K. Zilberberg, S. Trost, A. Behrendt, T. Riedl, Atmospheric preasure plasma ALD of TiO_x for Organic solar cells, *MRS Fall* **2012**, WW1.06, Boston.
- S. Trost, K. Zilberberg, A. Behrendt, T. Riedl, Room temperature sol-gel processing of SnO_x as electron extraction layer in inverted OSCs with improved thermal stability, *E-MRS Spring* **2012**, 14.3, Strasbourg.
- K. Zilberberg, H. Gharbi, A. Behrendt, S. Trost, T. Riedl, Low temperature sol-gel processing of MoO_x as high work function charge extraction layer in stable and efficient organic solar cells, *SPIE Photonics Europe* **2012**, 8435-17, Brussels.
- K. Zilberberg, S. Trost, I. Dumsch, S. Allard, U. Scherf, A. Behrendt, D. Lützenkirchen-Hecht, R. Frahm, T. Riedl, Efficiency enhancement of inverted low-bandgap polymer solar cells, *MRS Fall* **2011**, (Poster) H13.39, Boston.
- K. Zilberberg, S. Trost, J. Meyer, A. Kahn, and T. Riedl, Inverted organic solar cells with sol-gel processed high work-function transition metal oxide hole-extraction layers, *E-MRS Spring* **2011**, 11.4, Nice.
- K. Zilberberg, S. Trost, H. Schmidt, T. Riedl, Solution processed V_2O_5 as high work function charge extraction layers in organic solar cells, *MRS Spring* **2011**, C5.7, SF.
- H. Schmidt, T. Riedl, K. Zilberberg, T. Winkler, J. Meyer, H. Flügge, W. Kowalsky, Thin film encapsulation of inverted and semi-transparent organic solar cells using atomic layer deposition, *MRS Spring* **2010**, Symposium HH.

9. Acknowledgements

With this I would like to thank my dear colleagues K. Kraus, S. Trost, M. Fakhri, A. Räupke, A. Polywka, A. Behrendt, T. Jakob, T. Becker, L. Hoffmann, A. Makris, N. Pourdavoud, K. Brennecke, Dr. D. Theirich, Dr. R. Heiderhoff and Prof. P. Görrn for outstanding climate at office as well as in-private and for very productive co-operation.

My warmest thanks is addressed to my bachelor and master graduate students S. Trost, F. Gasse, R. Pagui, H. Gharbi, T. Abdallah, A. Codo and K. Brinkmann, who have done a notable contribution to this research.

For providing the essential experimental data and fruitful discussions, S. Adamczyk, E. Preis, S. Kowalski, M. Kraft, Dr. I. Dumsch and Prof. U. Scherf (Macromolecular Chemistry, BUW); D. Krämer, J. Gasse, Dr. D. Lützenkirchen-Hecht (Physics of Condensed Matter, BUW); Dr.-Ing. H. Schmidt and Prof. W. Kowalsky (Institute of High-Frequency Technology, TU-Braunschweig); S. Wang and Prof. Scheer (Microstructural Technique, BUW); P. Reckers and Dr. T. Mayer (Institute of Surface Science, TU-Darmstadt); Dr.-Ing. J. Meyer and Prof. A. Kahn (Surface Science Lab, Princeton Univ.) are gratefully acknowledged.

Honeywell Specialty Chemicals Seelze GmbH is acknowledged for P3HT supply. The help of Microtrac Europe GmbH (Meerbusch, Germany) in gaining insights to DLS is appreciated. The gratitude is expressed to the Federal Ministry for Education and Research (Grant No. 13N11777) and the Deutsche Forschungsgemeinschaft (Grant No. RI1551/4-1) for financial support.

Special thanks to Dr.-Ing. D. Dudek, Dr. D. Theirich, Prof. L. J. Balk for encouraging me for this thesis, to Prof. U. Scherf for his effort as a co-referent and to my advising Prof. T. Riedl for giving the opportunity and providing the means for this research and my personal professional rise, for sharing the overwhelming experience and for his support beyond the research activities.

Thank you very much!

Appendix A. Excursus: low-bandgap PCPDTBT:$PC_{70}BM$ OSCs

Aside from the liquid-processing of functional and electrode layers for OE devices, some additional activities within this thesis were devoted to the optimization of polymer:fullerene OSCs comprising a low-bandgap PCPDTBT (Poly[2,6-(4,4-bis-(2-ethylhexyl)-4H-cyclopenta[2,1-b;3,4-b']dithiophene)-alt-4,7(2,1,3-benzothiadiazole)]) and $PC_{70}BM$. Exhibiting an extended absorption in red spectral region, thin photo-active films of PCPDTBT allow for reasonably efficient OSCs that remain vastly transparent in the visible spectral region (**Figure A.1**).

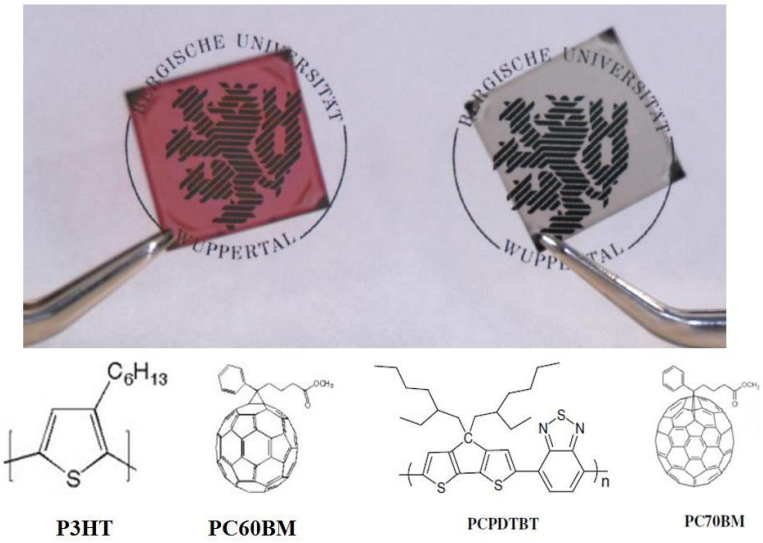

Figure A.1. Comparison of optical perception between P3HT:$PC_{60}BM$ and PCPDTBT:$PC_{70}BM$ blended films with thicknesses optimized for efficient OSCs. Molecular structures of corresponding BHJ moieties.

In the following, the impact of the polymer molecular weight, processing additives, resulting morphology and the OPV stack architecture on the device PCE and the origin of that are discussed.

A.1. Material specifics and effect of device architecture

The PCPDTBT films exhibit an enhanced hole mobility and balanced charge transport, when blended with $PC_{70}BM$.[263] However, the short exciton life-time and too small D/A phase domains upon thermal annealing

typically result in low OPV device *FF*.[263, 264] To improve that, additives, like 1,8-octanedithiol (ODT), that selectively solve the fullerene and have higher boiling point than the background solvent are used to prepare the BHJ.[265, 266] This provides additional mechanical mobility for a fullerene moiety and a chance to thermo-dynamically organize itself into larger cluster, while the polymer component has been immobilized upon formation of a solid phase.

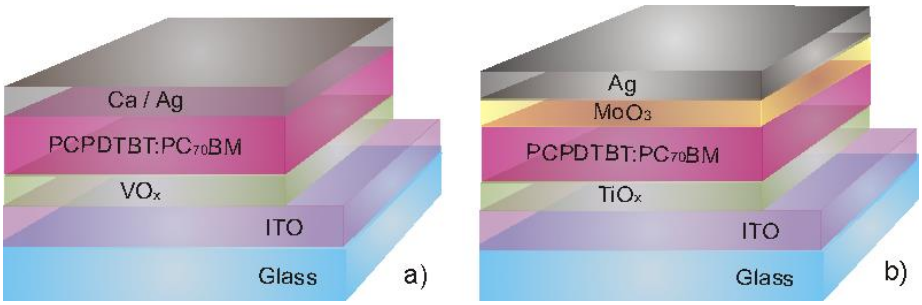

Figure A.1.1. Regular (a) and inverted (b) design of studied OSCs comprising PCPDTBT.

In this work, the nano-morphological changes introduced by ODT as a co-solvent are characterized indirectly, first, by analyzing the characteristics of regular OSC with the material stack, depicted in **Figure A.1.1.-a**. The use of sVO_x and Ca at the interfaces to organics ensures the high built-in field and, therefore, does not limit the device performance. The high *WF* of sVO_x allows for efficient hole extraction also from deep HOMO materials, such as PCPDTBT. For this study, an optimized blend proportion and BHJ thickness (see **Appendix B.1** for details) is chosen. The thickness remains unchanged also upon addition of ODT.

The cells comprising PCPDTBT of higher molecular weight (*MW*) of 19000-26000 g/mol compared to 17000-24000 g/mol without addition of ODT result in more efficient devices mainly due to higher J_{sc} (**Figure A.1.2.-a** and **Table A.1.1**). In general, the lower *MW* is associated with higher density of main-chain defects, limiting the hole mobility.[41, 42, 267]

For PCPDTBT with lower *MW* (17000-24000 g/mol), the addition of small portion of ODT (vol. 1.7%) to the blend solution improves the device J_{sc} and *FF* dramatically (*PCE* increase of 30%) and outperforms the blend comprising the higher *MW* polymer, as the charge carrier mobility improves in case of larger PCBM clusters in the BHJ.[263, 265, 268] Further increase of ODT fraction in the solution results in fullerene over-aggregation, increase in bimolecular recombination [268] and deteriorated device characteristics.

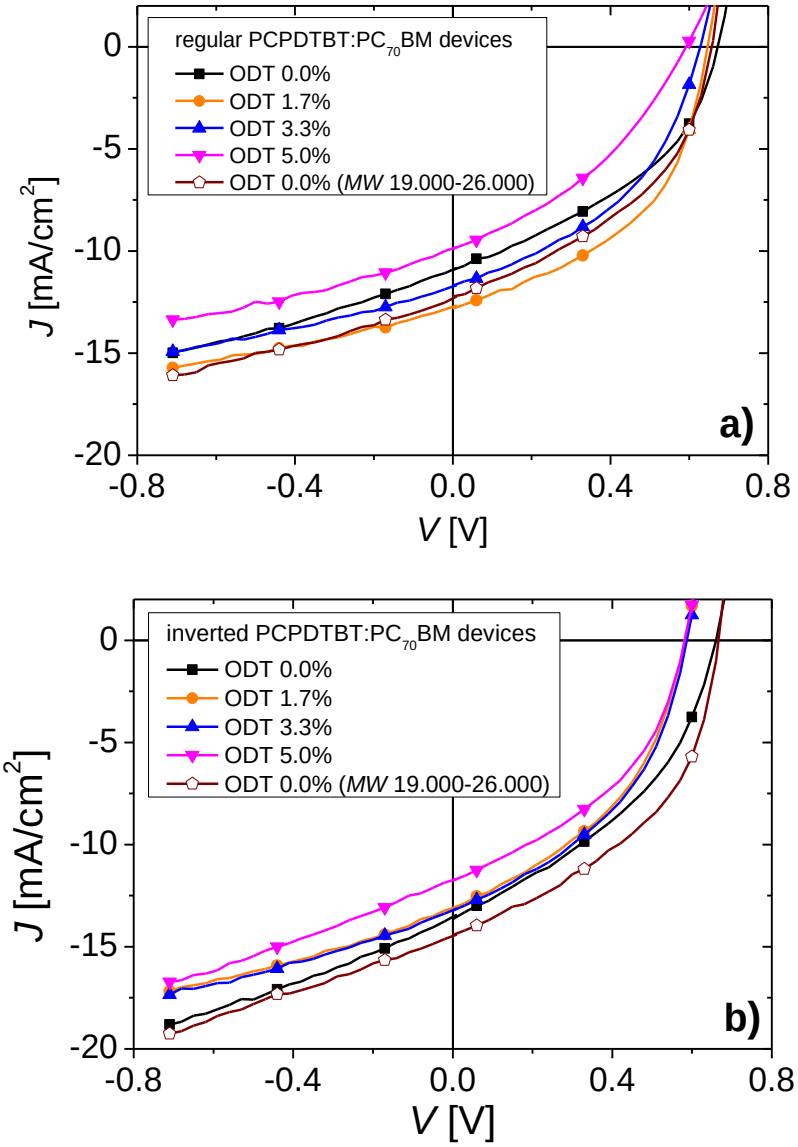

Figure A.1.2. *JV*-characteristics of regular (a) and inverted (b) OSCs with PCPDTBT:$PC_{70}BM$ photo-active layer. The molecular weight and the amount of ODT are varied.

Interestingly, inverted devices exhibit the same V_{oc}, as the regular ones, but much higher J_{sc} (**Figure A.1.2.-b**, **Table A.1.2**), which can be partially associated with more efficient optical intensity distribution through the thin film inverted device stack (to be discussed in the next **Appendix A.2**). The PCPDTBT fraction with higher *MW* results in the best performance.

Table A.1.1. Characteristics of regular OSCs comprising PCPDTBT:$PC_{70}BM$ prepared with varied amount of ODT and for different molecular weight.

	PCE [%]	V_{oc} [V]	J_{sc} [mA/cm^2]	*FF* [%]
ODT 0.0% 19.000-26.000 g/mol	3.5	0.66	12.2	43
ODT 0.0% 17.000-24.000 g/mol	3.0	0.67	10.9	41
ODT 1.7% 17.000-24.000 g/mol	3.9	0.65	12.8	47
ODT 3.3% 17.000-24.000 g/mol	3.2	0.63	11.7	43
ODT 5.0% 17.000-24.000 g/mol	2.2	0.59	9.9	37

Table A.1.2. Characteristics of inverted OSCs comprising PCPDTBT:$PC_{70}BM$ prepared with varied amount of ODT and for different molecular weight.

	PCE [%]	V_{oc} [V]	J_{sc} [mA/cm^2]	*FF* [%]
ODT 0.0% 19.000-26.000 g/mol	4.3	0.67	14.4	45
ODT 0.0% 17.000-24.000 g/mol	3.7	0.66	13.4	42
ODT 1.7% 17.000-24.000 g/mol	3.2	0.58	13.1	43
ODT 3.3% 17.000-24.000 g/mol	3.3	0.59	13.2	43
ODT 5.0% 17.000-24.000 g/mol	2.9	0.58	11.8	42

The addition of even small portion of ODT deteriorates the device V_{oc} and J_{sc} instead of improving them, as observed in case of regular device structure. For PCPDTBT of both higher and lower *MW* fractions, the inverted device operates better completely without ODT. The more severe

deterioration of the V_{oc} in inverted devices upon addition of ODT hints for strongly different morphological BHJ evolution and/or vertical phase segregation (see **Appendix A.2**) for different device architectures.

A.2. Origin of performance advantage in inverted stack layout

Due to a large number of interfaces of materials exhibiting different optical constants in multilayered opto-electronic thin film devices, an interference pattern of multiply reflected light results for every wavelength in local variation of the intensity across the device stack. An exemplary transfer-matrix-simulated light intensity distribution for 740 nm wavelength over the device stack (regular and inverted) is depicted in **Figure A.2.1**. The larger the area under the intensity (Ψ^2) profile confined within the BHJ (grey region), the more photons can contribute to the device photo-current.

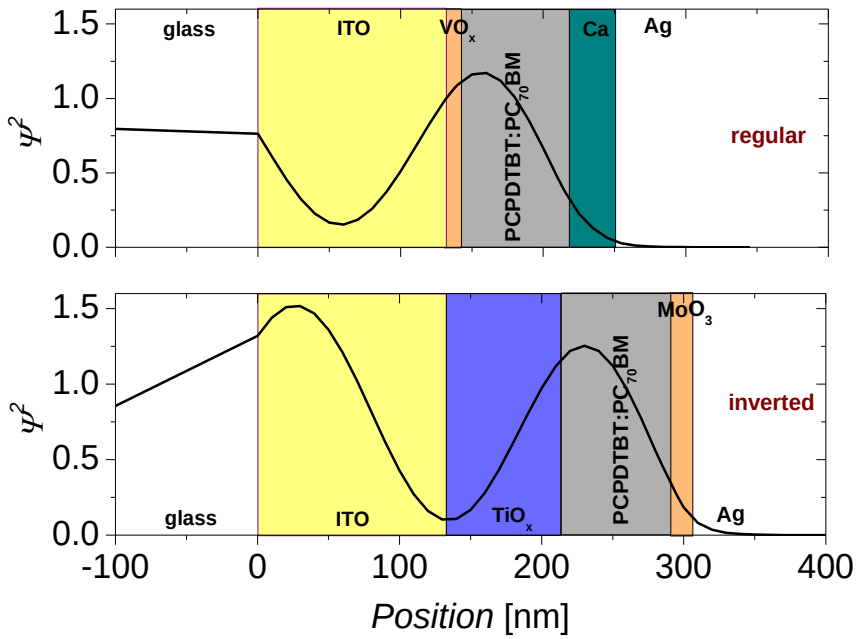

Figure A.2.1. Stack-depth resolved optical interference pattern for investigated regular and inverted OSCs at incident light wavelength of 740 nm.

Comprising the different charge extraction and electrode materials in different order and thickness, the inverted device structure might induce an enhanced spatial overlap between Ψ^2 maxima and photo-active layer

resulting in higher photo-current. To evaluate this, the intensity profile for both studied architectures for each relevant wavelength is integrated individually over the thickness of the photo-active layer and spectrally resolved in **Figure A.2.2**. In addition, the spectral absorption profile of the used BHJ (PCPDTBT:$PC_{70}BM$) is demonstrated as a green dashed line for clarity.

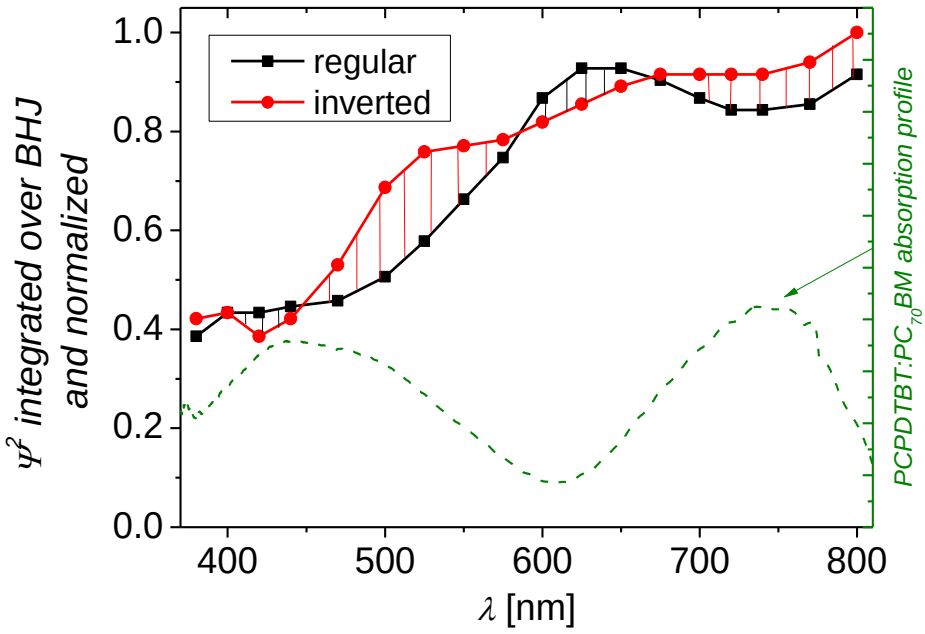

Figure A.2.2. Spectrally resolved normalized light intensity profile integrated for every wavelength over the thickness of the BHJ for both regular and inverted OSCs. The green dashed line visualizes the absorption profile of PCPDTBT:$PC_{70}BM$ blend.

From this plot the origin of the J_{sc} enhancement for inverted devices as compared to regular ones (fabricated using materials according to **Figure A.1.1**) becomes clear. The red-marked areas visualize the more intense photon flux for BHJ of inverted devices that additionally spectrally overlaps with rising absorption features of the BHJ. In contrast, the regular device stack outperforms the inverted one significantly only in the region from 580 to 660 nm (black-marked area); and in this region the absorption minimum

of the used BHJ is observed. Summarized, roughly 1 mA/cm^2 more J_{sc} is calculated for the inverted device compared to the regular one.

To optimize the light absorption in regular, but also in inverted OSCs, the well-known optical spacer [269-274] effect can be evaluated by using different interface and electrode materials in different thicknesses. For regular devices, the device J_{sc} with VO_x and MoO_x of varied thickness at the anode side along with Ca, Al and TiO_x on the cathode side is simulated (**Figure A.2.3**). For inverted devices, the influence of MoO_x and VO_x at the anode side and TiO_x (no metals for transparency reasons) at the cathode side is analyzed (**Figure A.2.4**). For this simulation, a pure photo-effect based on the ideal morphology of the BHJ is considered, i.e. recombination losses or R_s associated with a real device do not influence the simulated J_{sc}.

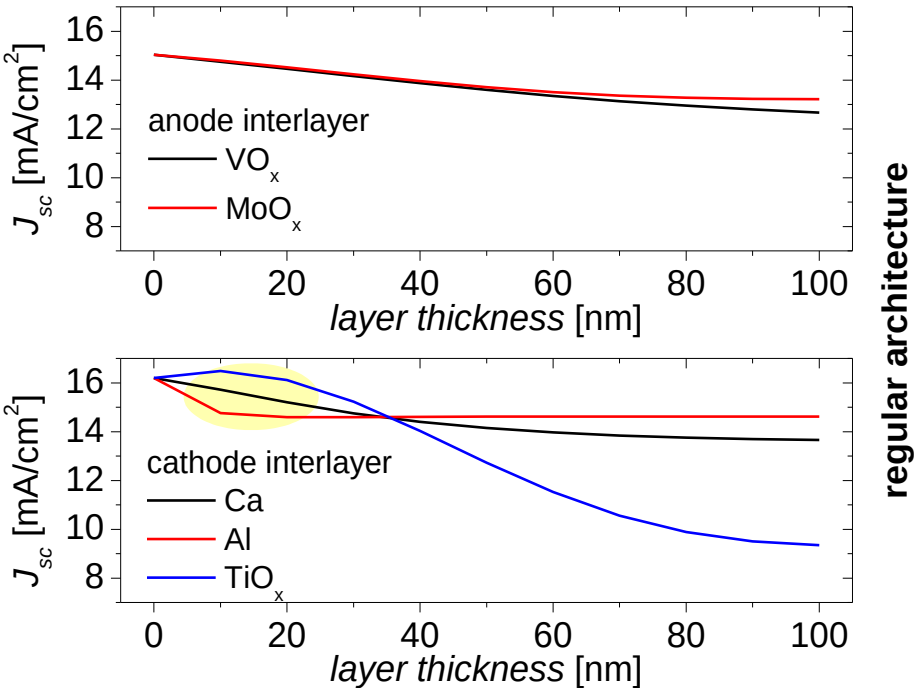

Figure A.2.3. Simulated J_{sc} of regular PCPDTBT:$PC_{70}BM$ OSCs comprising different anode and cathode interlayers in different thicknesses.

According to simulation results and from the optical point of view, the presence of anode interlayers of MoO_x and VO_x in regular devices (**Figure A.2.3**) in any thickness within the studied 100 nm range only reduces the internal quantum efficiency (*IQE*), i.e. number of absorbed photons that lead to excitation. On the cathode side, the *IQE* can clearly be enhanced by roughly 9% introducing 10 to 15 nm thick TiO_x optical spacer (instead of e.g. Ca) previous to metal electrode (Ag) deposition.

In a similar way, the glass/ITO adjacent cathode interlayer of TiO_x leads to reduced *IQE* for any oxide thickness in inverted structure (**Figure A.2.4**). On the anode side, the *IQE* is slightly increased by introduction of 10 nm of both VO_x and MoO_x and is vastly independent on the intrinsic absorption losses in these thin-film (~10 nm) metal oxides.

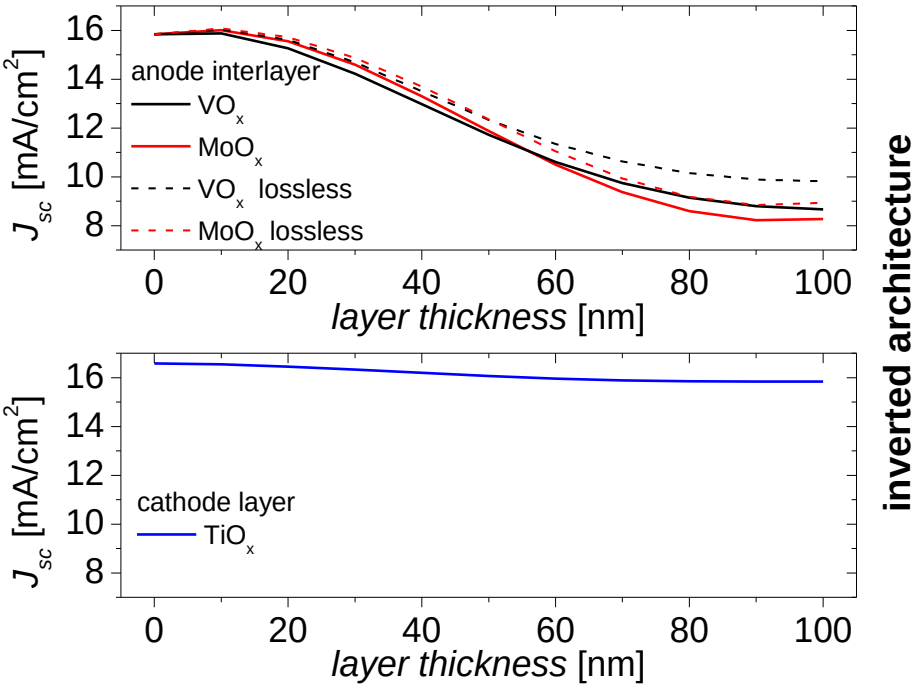

Figure A.2.4. Simulated J_{sc} of inverted PCPDTBT:$PC_{70}BM$ OSCs comprising different anode and cathode interlayers in different thicknesses. For absorbing high *WF* metal oxides at the anode side, the simulated J_{sc} plot upon exclusion of optical losses is additionally dash-line depicted.

The higher photo-current for inverted devices and the improvement of regular device characteristics by addition of vol. 1.7% ODT might have a nano-morphological origin.

The depth resolved elemental analysis via XPS (**Figure A.2.5**) reveals a non-uniform material distribution in the BHJ, which exhibits a capping layer of the polymer close to the BHJ/air interface for both blends: with and without ODT. Such morphology is certainly preferential for an inverted device, where the holes are extracted via top electrode, due to enhancement of hole selectivity at the anode interface. However, the enhancement of regular device performance upon addition of ODT cannot be explained by this. In contrary, the somewhat spatially more broadened PCPDTBT capping for ODT-modified blend is expected to deteriorate the electron extraction at the top electrode. Further, the origin of V_{oc} drop for inverted cells upon ODT addition is not revealed by this depth profile.

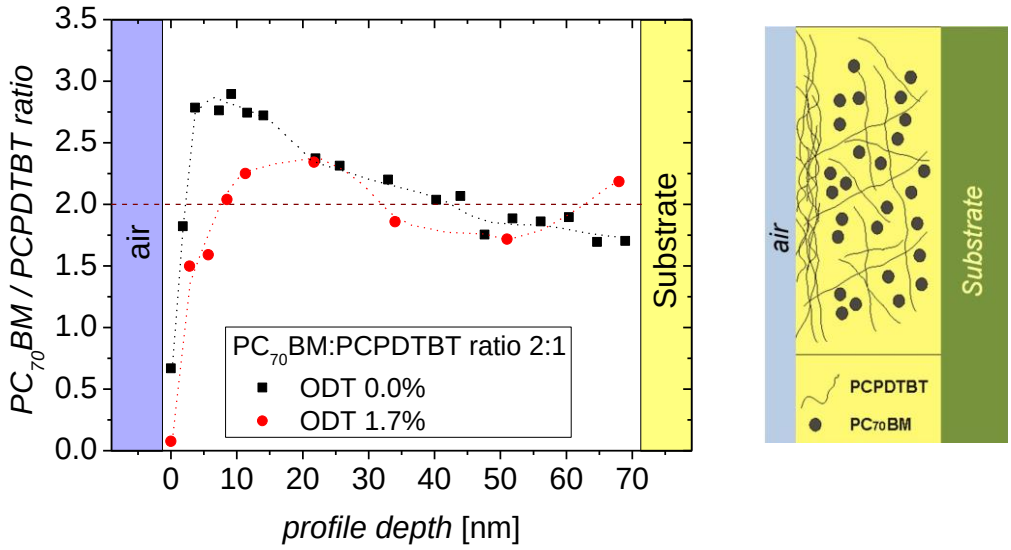

Figure A.2.5. XPS depth profile of neat and co-solvent (ODT) modified PCPDTBT:$PC_{70}BM$ blend with initial mass ratio 1:2 (visualized by the red dashed line). The schematic visualization of observed vertical phase segregation is depicted to the right.

Though the XPS depth profiling can access the buried morphology, the elemental signal remains integrated over the whole excited sample spot.

Thus, the information about the lateral (in general, substrate dependent) D/A nano-phase distribution that might shine light on the remaining questions is missing. For now, further 3D-tomographical analysis of nano-morphology (e.g. via grazing incidence XRD) is required.

A.3. Summary

Having an extended absorption in red and being an attractive material for see-through OSCs, the low-bandgap PCPDTBT exhibits somewhat poor nano-morphology in terms of charge transport, when blended with a fullerene. The use of properly concentrated co-solvents, like ODT, allows typically for simultaneous increase of all device characteristics. Surprisingly, the inverted devices studied in this work demonstrate the best performance without ODT exhibiting decisively higher photo-currents than regular devices, best performing, if ODT-modified. The optical simulation of the regular device stack shows a clear improvement potential for light absorption by introducing the optical spacer (e.g. TiO_x) previous to top metal deposition.

In addition to optimized light distribution, the higher photo-current in inverted devices is expected to be supported via enhanced hole extraction at the polymer rich anode interface, as revealed by XPS depth profiling for both BHJs: with and without ODT.

The influence of molecular weight is briefly addressed to underline its importance for device performance, as the polymer with lower *MW* results in less photo-current associated with main-chain defects.

The origin of the severe V_{oc} drop upon addition of even small portions of ODT for inverted devices (in contrast to regular ones) remains unclear, but is assumed to rely on lateral (probably substrate dependent) nano-morphological D/A phase deviations and is a subject for future work.

Appendix B. Experimental details

This chapter summarizes the experimental details of device processing and characterization, as well as the techniques of material analysis. Among them, somewhat less-known to a broad circle of readers, Kelvin-probe and dynamic light scattering analysis techniques and the basics of sol-gel-technique for metal oxides are discussed more detailed in corresponding separate sub-chapters.

B.1. Material processing

The polymer:fullerene OSCs studied in this work are based on the BHJ concept, where the polymer and the fullerene are blended previous to deposition of the active layer. The active area of the devices is defined (if not otherwise specified) lithographically to 0.03 cm^2 on commercially available glass/ITO substrates with sheet resistance (R_{sh}) of 13 Ω/sq.

The polymer:fullerene blend of P3HT (Honeywell Chemicals Seelze) and $PC_{60}BM$ (American Dye Source) with a weight ratio 1:1 were filtered with PTFE 0.2 µ and spin-coated at N_2 from chloroform and chlorbenzene (vol. ratio 1:1) solution (16 mg/ml). After subsequent annealing in N_2 at 110°C for 8 min, the layer thickness of 200-220 nm was achieved.

The polymer:fullerene blend of PCDTBT (Ossila) and $PC_{70}BM$ (Solenne BV) with a weight ratio of 1:4 were spin-coated in N_2 from a warm (90°C) solution (24 mg/ml) in 1,2-dichlorbenzene using PTFE 0.2 µ filter with subsequent annealing in N_2 at 70°C for 15 min resulting in film thickness of 90 nm.

The polymer:fullerene blend of PCPDTBT (synthesized at Macromolecular Chemistry Department, Univ. Wuppertal) in different molecular weights (17000-24000 vs.19000-26000 g/mol) and $PC_{70}BM$ (Solenne BV) with weight ratio 1:2 were spin-coated in N_2 from chlorbenzene solution (10 mg/ml) containing a small portion (specified individually) of co-solvent additive 1,8-octanedithiol (ODT) using PTFE 0,2 µ filter. Subsequent

thermal annealing at 50°C for 8 min and treatment by high vacuum (10^{-7} mbar) was applied for solvent evaporation.

The PEDOT:PSS films in 25 nm thickness were prepared via spin-coating of an aqueous dispersion (AI 8043, H. C. Starck) and subsequent annealing in ambient air at 110°C for 1 h to remove water residue.

The sol-gel vanadium oxide films (sVO_x) resulted in hydrolysis and condensation reaction of pre-hydrolyzed (90 min stirring in humid air) spin-coated isopropanol (anhydrous) solution of vanadium(V)oxitriisopropoxide (Alfa Aesar) at 1:70 vol. ratio in ambient air and at *RT*. For inverted organic solar cells, the more diluted solution (unless otherwise specified) of vol. 1:150 was used to prevent eventual deterioration of organic/oxide interface properties.

The sol-gel molybdenum oxide films ($sMoO_x$) were spin-casted from pre-hydrolyzed (30 min stirring in air with 65% *rH*) isopropanol (0.1% of H_2O) solution of Bis(2,4-pentanedionato)molybdenum(VI)dioxide (TCI Europe) at 1:150 w/v ratio. After hydrolysis and condensation at *RT* in ambient air (65% *rH*) for 1 h, the films were annealed in N_2 at 130-150°C for 20 min to remove adsorbates.

The thermally evaporated V_2O_5 and MoO_3 films (15 nm, unless otherwise stated) were processed from metal oxide powders (Alfa Aesar) via an effusion cell equipped with boron-nitrite crucible at base pressure 10^{-7} mbar and deposition rate of 0.04 nm/s.

Sol-gel processed titanium oxide ($sTiO_x$) films were spin-coated from pre-hydrolyzed (30 min stirring in humid air) isopropanol (anhydrous) solution of titanium(IV)isopropoxide (vol. ratio 1:35), then left in ambient air for 1 h for hydrolysis and condensation at *RT* resulting in 80 nm final film thickness.

Titanium dioxide films processed via Atomic Layer Deposition (ALD) on Beneq TFS 200 were deposited from titanium(IV)isopropoxide using H_2O as a reaction partner at 100°C reactor temperature. The films of 20 nm thickness were used for device fabrication.

The Al:ZnO (AZO) nano-laminate was ALD-processed on Beneq TFS 200 at 100°C reactor temperature by periodic pulsing of 50 cycles of diethylzinc and H_2O for ZnO and 2 cycles of trimethylaluminum and H_2O for Al_2O_3.

The sol-gel tin oxide films ($sSnO_x$) were deposited from acetylacetone stabilized cross-linked (stirring in humid air for 30 min) solution of Tetrakis-(diethylamino)tin(IV) in isopropanol [199]. The film formation occurred at *RT* during hydrolysis and condensation in ambient air (60% *rH*) within 1 h.

The films of conjugated polyelectrolytes based on N-methylimidazoliniumalkyl-substituted poly(3-[6-bromohexyl]thiophene) (P3ImHT) having molecular weight of 10000 g/mol were spin-coated in N_2 from methanol:ethanol (vol. ratio 2.5:1) solution (0.0143 mg/ml) and subsequently dried at 100°C for 5 min in N_2.

The metallic electrodes (100 nm final thickness) were thermally evaporated at base pressure 10^{-7} mbar using a shadow mask and deposition rates of 0.2 nm/s using tungsten boats for silver and alumina coated tungsten boats for aluminum.

The conductive films of silver nano-wires (AgNWs) were spin-coated (unless otherwise specified) in ambient air from a well-shaked commercially available AgNW-dispersion (BlueNano) in isopropanol with final concentration of 5 mg/ml and subsequently dried at 50°C for 1 min for solvent removal.

For stability evaluation of layers comprising AgNWs, samples were stored in climate chamber at specifically defined temperature and *rH*.

For In-free devices commercially available $F:SnO_2$ substrates (Sigma Aldrich) with sheet resistance of 13 Ω/sq were used. The active device area was defined lithographically (0.018 cm^2).

B.2. Measurements and simulation

The characterization of solar cells occurred in ambient air using a source-meter (Keithley 2400-C) and a solar simulator (Newport, 300 W, AM1.5G,

100 mW/cm^2). A reference crystalline Si shunted photo-diode was used for power density calibration.

The atomic force microscopy (AFM) measurements were carried out in tapping mode on Veeco Atomic Force Microscope at the Institute of Macromolecular Chemistry (Univ. Wuppertal).

The Scanning Electron Microscopy (SEM) measurements were carried out in high resolution mode in a Philips XL30S FEG with field emission cathode. For electron beam induced potential contrast (EBIP) imaging of surface-confined nano-structures, a Monte-Carlo electron-flight simulation was carried out to predict the correlation between the primary electron beam energy and the depth of electron-sample interaction.

The film surface potential was measured using a Kelvin Probe (KP) system from McAllister KP6500 under controlled atmosphere (vacuum, air, N_2 etc.). The work function was estimated from contact potential difference using the reference sample of highly ordered pyrolytic graphite (HOPG) with known and air-stable work-function of 4.5 eV. For measurement principals see **Appendix B.4**.

The film thickness was controlled via a Stylus profilometer (Bruker, Dektak).

The film morphology was studied via X-ray Diffraction (XRD) on X'Pert Pro MPD diffractometer with a molybdenum x-ray emitter using θ-2θ angle setup.

For optical absorption and transmission measurements on metal oxides (unless otherwise specified) the solar simulator as a light source and the Spectrometer (Ocean Optics HR4000CG-UV-NIR) with an optical fiber as detector were used. The optical absorption coefficients were derived from transmission measurements using the uncovered substrate (glass or glass/ITO) as reference. The reflection losses at the first interface with ambient air were taken into account by considering the refractive index of characterized material.

The optical measurements on samples comprising the silver nano-wires a white deuterium halogen lamp (DH-2000-BAL, Ocean Optics, 1 mW/cm^2) as a light source and a fiber spectrometer (USB 2000+XR1-ES, 186 – 1041 nm) as detector were used. An average of several measurements at different sample area points was derived. The specular transmission was measured in an angle of 0° (see **Figure B.2.1**). As a reference, the signal on the detector without the scattering sample has been used. The scattered transmission spectra were captured at angles of 22.5°, 45° and 67.5° (see **Figure B.2.1**). The referencing of the scattered spectra (unlike for the specular transmission spectra) is impossible by simply capturing the spectrum without the scattering sample. For this purpose, the ratio between the diffusive (specular and scattered, Si-detector close to the sample) transmitted intensity of HeNe-laser (4 mW, dia. 2 mm, 632.8 nm) and specular (detector at a distance of 75 cm to the sample along the laser beam to exclude the non-collimated scattered light) transmission was determined. Taking into account that the scattered spectra are almost independent on scattering angle, this ratio was used to calibrate the scattering spectra with respect to the specular transmittance. The specular reflectance spectra were determined using the beam splitter.

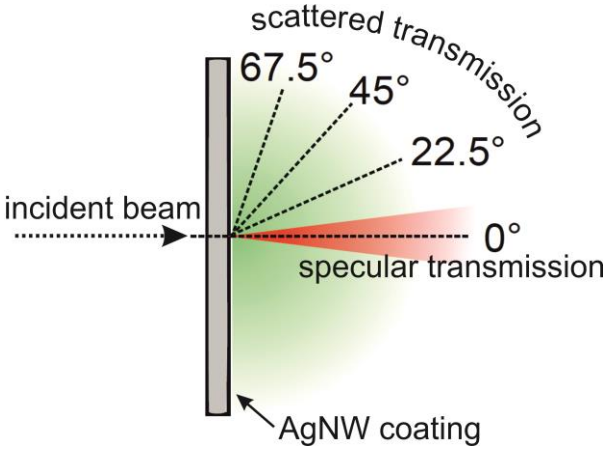

Figure B.2.1. Schematic optical transmission measurement setup for stark scattering samples (e.g. comprising nano-wires).

The electrical conductivities of metal oxides was measured using pre-patterned inter-digidated ITO/Au electrode structure with the channel geometry 10 mm x 2.5 µm (width, effective length). The specific electrical conductivity was estimated taking the geometry of the channel into account.

For conductivity measurements on macroscopically conductive AZO films and silver nanowire hybrid layers the four-point-probe method was used. For better contact, a small drop of silver conductive paste was deposited at the sample corners.

The size of pre-formed molecular clusters in metal-organic precursor solutions was determined via dynamic light scattering (DLS) heterodyne technique in 180° on Nanotrac Wave (Microtrac Europe GmbH) using a 780 nm excitation laser. For the model calculations, a spherical particle shape and viscosity and dielectric constant values of the solvent (isopropanol) for strongly diluted precursor solutions were assumed. For measurement principals see **Appendix B.5**.

The XPS measurements for metal oxides were performed on ESCALAB 5, VG Scientific with photoelectron take off normal to the sample surface and at constant analyzer energy mode with pass energy of 20 eV at base pressure of 10^{-8} mbar. Excitation occurred via non-monochromatized Mg K-Kα radiation (1253.6 eV) with an input power of 200 W. The Al Kα line (1486.6 eV) was also used. The evaluation of XPS spectra was carried out using background subtraction according to Shirley [275] and a peak deconvolution with least-squares fit [276]. The peak area was weighted with respective photoionization cross-sections by Scofield [277].

For XPS depth profiling, the sputter ion (Ar) source with power density of 75 mW/cm^2 at the base pressure of 10^{-5} mbar was used without vacuum break. The resulting sputter rate was estimated to 0.5 nm/min for organic layers and 1.4 nm/min for metal oxide. The large sputter crater of 20 mm ensured the homogeneous removal of metal oxide.

To study the electronic structure of metal oxides, Ultraviolet Photoelectron Spectroscopy (UPS) and Inverse Photoemission Spectroscopy (IPES) techniques were used in collaboration with Surface/Interface Science Lab (Univ. Princeton). For UPS with experimental resolution of 0.15 eV, the discharge radiation lines of He I (21.22 eV) and He II (40.8 eV) were used. IPES was performed in isochromatic mode with resolution of 0.45 eV.

The photoluminescence (PL) on P3HT was carried out for diluted solutions of organics in chlorbenzene on Cary Eclipse (Varian). The optical excitation was performed at 470 nm to avoid the parasitic excitation of the solvent.

To control the change in molecular structure of polymers, a Nuclear Magnetic Resonance (NMR) technique at Avance III 600 MHz (Bruker) setup was used. The measurements were performed at temperature of 300 K. The polymer was referenced to dichlorobenzene-d.

The viscosity of metal-organic precursor solution was measured with Anton Paar Physica MCR101 rheometer.

The optical constants (refracting index, extinction coefficient) of the materials were measured via ellipsometer (BASE-160). The films of investigated materials were deposited on Si substrates with native oxide. For the calculation of the constants from reflection signals a three-layer-model was applied.

To evaluate the influence of optical spacers (metal oxides) on the distribution of the interfered light within the stack of the OSCs for a given thin film material system the optical stack modelling based on transfer matrix formalism [28, 278, 279] was carried out with help of SETFOS 3.2 simulation software. The estimated n and k for each layer were used as boundary condition for modelling. For the prediction of short circuit current through the device for illumination at a given wavelength the ohmic losses at the stack interfaces and within the polymer:fullerene junction were neglected.

The oxygen plasma treatment of metal oxides was performed via RF magnetron discharge at 0.05 mbar background pressure and power density of 318 mW/cm^2.

The scotch-tape peeling test is applied to evaluate mechanical stability and adhesion on substrate of hybrid coatings of silver nano-wires and metal oxides. The tape is 15 mm wide and is peeled completely off during 2-3 s in 90° angle to sample surface.

B.3. Sol-gel technique

In this work, for the liquid-processing of metal oxides the sol-gel technique is used. Therefore, a general introduction into simplified process chain might be useful for the reader. The metal-organic precursor is first diluted with alcoholic solvent. With controlled addition of small portions of water (e.g. by stirring in humid air) a partial hydrolysis with detaching the alcoholic molecules occurs (**Equation B.3.1**).

$$M(OR)_n + H_2O \rightarrow M(OR)_{n-1}OH + ROH \qquad (\mathbf{B.3.1})$$

In the next step, the partially hydrolyzed molecules run condensation on contact to each other with detaching the water, according to **Equation B.3.2**. The reaction between partially hydrolyzed and non-hydrolyzed precursor molecules with detaching of alcohol is also possible.

$$M(RO)_mOH + M(RO)_mOH \rightarrow M(RO)_m\text{-}O\text{-}M(RO)_m + H_2O \qquad (\mathbf{B.3.2})$$

Following this principal, more complex oligomers (oxo-cluster or sol particles) are formed reaching the nm-scale in size. The so called cross-linking to a gel of (in general) higher viscosity within a solution is established. After film deposition, further condensation via remaining non-reacted alcoholic groups occurs, accompanied by detaching water, alcohol and solvent evaporation. A densified amorphous metal oxide matrix is formed.

B.4. Kelvin-probe analysis

Kelvin-probe (KP) technique allows for capacitive measurement of the contact potential difference (*CPD*), which is induced by charge transfer and Fermi-level alignment between the grounded sample and also grounded cylindrical metallic probe head. In this equilibrium, the sample and the probe are continuously oppositely charged.

To make the measurement of the *CPD* technically possible, the probe is now mechanically oscillating orthogonal to investigated sample surface with constant frequency and amplitude. In such a capacitive structure this oscillation induces a sin-formed current, which flows as long as the sample and the probe are charged.

Applying the external voltage bias to the capacitive structure distorts the equilibrium alignment of the Fermi-levels of the sample and the probe, resulting in less charging of the structure and associated lower induced current. By varying the external bias, the voltage value is found, for which the charging is compensated and no current flows. This value is the wanted *CPD* between the sample and the probe surface. Carrying out the *CPD* measurement on the reference sample with known *WF*, the *WF* of the unknown sample can be easily calculated.

B.5. Dynamic light scattering

Dynamic light scattering (DLS) is a technique for determination of particle size within a solution / dispersion. A laser-beam of known wavelength (frequency) is coupled into the cuvette with a sample formulation and reflected towards the detector by differently sized particles populating the sample. As the particles obey the continuous thermally driven Brown motion, the frequency of reflected light is modified by the velocity of particles according to Doppler effect. In its turn, the particle motion velocity within the sample of known temperature and viscosity is coupled to the size of the particle.

Applying Fourier-Transform to the detector signal gives the power spectrum. In this spectrum each frequency is associated with particle size (according to Stokes-Einstein relation) and the signal power at that frequency corresponds with number of the particles of this size in a sample.